

**TRANSIENT LIQUID PHASE BONDING IN
THE NICKEL BASE SUPERALLOY CM 247 LC**

By

JACKY MAN-LAM CHENG
B.A.Sc., The University of British Columbia, 2003

A THESIS SUBMITTED IN PARTIAL FULFILMENT OF
THE REQUIREMENTS FOR THE DEGREE OF

MASTER OF APPLIED SCIENCE

in

THE FACULTY OF GRADUATE STUDIES

(Materials Engineering)

THE UNIVERSITY OF BRITISH COLUMBIA

November 2005

© Jacky Man-Lam Cheng, 2005

Abstract

In this work, the effects of temperature and time were investigated on the microstructure and properties of Transient Liquid Phase bonds in the directionally solidified superalloy CM 247 LC with a commercial braze filler material MBF-80 (Ni-Cr-B-C). Specimens were bonded at 1070°C, 1125°C and 1170°C for durations of 15 minutes, 1 hour and 4 hours. The resultant microstructures were then examined metallographically using optical and scanning electron microscopes. The mechanical properties were determined by micro-hardness and tensile tests.

The microstructure of bonded joints contained blocky and acicular precipitates in the base material. The chemical compositions of these precipitates were found to be similar and were nickel depleted and tungsten rich compared to the base metal. Mechanical tests made it evident that completion of the isothermal solidification in a TLP bond joint does not guarantee satisfactory joint properties. Extensive precipitation of hard and brittle phases and chemical inhomogeneity in the joint microstructure warrants further post-bond heat treatment.

Models of the TLP bonding process, available in the literature, were applied in this work. The apparent activation energy for the diffusion of boron in CM 247 LC was found to be 219 kJ/mol. Analytical models predicted isothermal solidification times in close agreement with experimental observations.

Two numerical models were developed in this work included a moving boundary model based on diffusion coefficients and equilibrium compositions and a phenomenological model coupled to thermodynamic and atomic mobility databases. The moving boundary model predicted satisfactory isothermal solidification times. The phenomenological model predicted times which were generally lower than those found experimentally. From this work, it is apparent that the mobility data available for boron is insufficient for the current system.

Table of Contents

Abstract.....	ii
Table of Contents	iii
List of Tables	v
List of Figures.....	vi
List of Symbols	ix
Acknowledgement	xiii
Chapter 1 - Introduction	1
Chapter 2 - Literature Review	4
2.1 The Metallurgy of Superalloys	4
2.1.1 Superalloy Microstructures	4
2.1.2 Superalloy Chemistry.....	8
2.2 Component Repair Technologies for Superalloys	9
2.2.1 Fusion Welding.....	9
2.2.2 High Temperature Brazing	10
2.2.3 Transient Liquid Phase Bonding.....	15
2.3 Evolution of Microstructure in TLP Bonded Joints.....	19
2.3.1 Ideal Joints	19
2.3.2 Real Joints.....	20
Chapter 3 - Experimental Methods.....	26
3.1 Casting	27
3.2 DTA Analysis of the Interlayer Material	32
3.3 Brazing.....	34
3.4 Metallography	36
3.5 Mechanical Testing.....	37
Chapter 4 - Results and Discussion	39
4.1 Microstructure of TLP Bonded Joints.....	39
4.1.1 Centerline Eutectic.....	42

4.1.2	Isothermal Solidification Zone	47
4.1.3	Precipitation Zone	48
4.2	High Temperature Tensile Properties	52
4.3	Hardness Properties	56
4.4	Diffusion of Alloying Elements	60
Chapter 5	- Modeling Predictions	64
5.1	Analytical Models for TLP Bonding	64
5.1.1	Heat Up	65
5.1.2	Liquid Dissolution	66
5.1.3	Widening	68
5.1.4	Isothermal Solidification	70
5.1.5	Homogenization	71
5.2	Predictions from the Analytical Models	72
5.2.1	Thermodynamic Data of the Ni-B System	72
5.2.2	Diffusion Coefficient of Boron in Nickel	74
5.2.3	Analytical Model Predictions	78
5.3	Numerical Models for TLP Bonding	84
5.3.1	Moving Boundary Models	86
5.3.2	Predictions from the Moving Boundary Model	89
5.3.3	Phenomenological Model	93
5.3.4	Predictions from the Phenomenological Model	96
Chapter 6	- Conclusions	101
6.1	Summary	101
6.2	Recommendations for Future Work	104
References	106
Appendices	112
Appendix A	- Analytical Solution for the Interlayer Dissolution Stage	112
Appendix B	- Analytical Solution for the Widening and Homogenization Stage	115
Appendix C	- Analytical Solution of the Isothermal Solidification Stage	118

List of Tables

Table 1 – Composition of common Ni-base superalloys, in weight percent.	8
Table 2 – Compositions of common nickel-base braze fillers in weight percent.	12
Table 3 – Nominal chemical composition for CM 247 LC in weight percent.	26
Table 4 – EDS Analysis of globular and acicular precipitates adjacent to the braze/substrate interface and in the precipitation zone of the substrate material in a joint bonded at 1125°C for 1 hour.	50
Table 5 – High temperature tensile properties of TLP bonded CM 247 LC joints at 850°C.	53
Table 6 – Equilibrium compositions obtained from the Ni-DATA Superalloy Database, Kaufman Binary Alloy Database and ASM Phase Diagram in atomic fraction.	74
Table 7 – Diffusion coefficients for boron in nickel at 1170°C.	74
Table 8 – Apparent diffusion coefficients for boron in nickel-base superalloys at 1170°C.	78
Table 9 – Predicted dissolution width using the analytical model vs. average experimentally observed widths (microns).	83
Table 10 – Dimensionless solidification rate constants, K, calculated using the analytical model outlined by Ramirez et al. for equilibrium compositions defined by various sources at 1070°C, 1125°C and 1170°C.	83
Table 11 – The predicted solidification time using analytical models proposed by Ramirez et al. and Gale et al. vs. experimentally observed times (hours).	84
Table 12 – Predicted dissolution width using the moving boundary model vs. experimentally observed widths (microns).	92
Table 13 – Predicted solidification times using the moving boundary model vs. experimentally observed times (hours).	92
Table 14 – Predicted dissolution width using the coupled phenomenological model vs. experimentally observed widths (microns).	99
Table 15 – Predicted solidification time using the coupled phenomenological model vs. experimentally observed times (hours).	99

List of Figures

Figure 1 – Cut away diagram of the internals of a modern high-bypass gas turbine aero-engine (Rolls-Royce Trent 1000) [2].....	2
Figure 2 – Increases in temperature capability of superalloys over their historical development [9].....	5
Figure 3 – The evolution of Superalloy microstructures, showing beneficial phases above and deleterious phases below the diagram [12].....	7
Figure 4 – Discretized stages of the TLP bonding process showing composition variation with distance x . (A) Initial composition prior to TLP bonding (B) Dissolution of the interlayer, (C) Widening and homogenization of the liquid, (D) Isothermal solidification.	16
Figure 5 – (a) Ni-B phase diagram [46] (b) Schematic diagram of the evolved microstructure found in an incompletely isothermal solidified binary alloy joint A) Eutectic phase formed from the thermal solidification of residual liquid B) Solid-solution pro-eutectic phase formed during isothermal solidification C) Base material.	20
Figure 6 – Directional solidification furnace used for casting CM 247 LC substrates.....	27
Figure 7 – Schematic diagram of the hot zone of the directional solidification furnace used for casting CM 247 LC substrates.	28
Figure 8 – Longitudinal section of a cast and heat treated CM 247 LC nickel-base superalloy specimen (2.25 cm long x 3.55 cm diameter).	30
Figure 9 - Cast and heat treated CM 247 LC microstructure consisting of fine cuboidal gamma prime precipitates in a nickel-solid solution gamma matrix and globular carbides.	31
Figure 10 – EDS scan of a typical carbide precipitate in the cast and heat treated CM 247 LC base material.	31
Figure 11 – DTA curve for MBF-80 braze foil during the cooling regime.....	33
Figure 12 – (A) Molybdenum brazing support loaded with a specimen for the processing of tensile specimens in a butt-joint configuration. (B) Schematic diagram.....	34
Figure 13 - Vacuum furnace used for the TLP bonding experiments.....	35

Figure 14 – A test specimen loaded on the Electro-Thermo-Mechanical Tester [69].	38
Figure 15 – Typical microstructures of TLP bonds in CM 247 LC processed at various temperatures and times.	40
Figure 16 – EDS scans of the centerline phases in a joint produced by holding at 1070°C for 1 hour (A) Nickel rich eutectic (B) Chromium rich eutectic.	44
Figure 17 – EDS scans of the centerline phases in a joint produced by holding at 1125°C for 1 hour (A) Nickel rich eutectic (B) Chromium rich eutectic.	45
Figure 18 – EDS scans of the centerline phases in a joint produced by holding at 1170°C for 1 hour (A) Nickel rich eutectic (B) Chromium rich eutectic.	46
Figure 19 – Typical EDS scan of the isothermal solidification zone in a joint held at 1070°C for 4 hours.	47
Figure 20 – (A) Precipitation in the isothermal solidification zone of a joint bonded at 1170°C for 15 minutes. (B) Magnified image of the region indicated in (A).	48
Figure 21 – Diffusion induced precipitation zone in the base material of a joints bonded at 1070°C, 1125°C and 1170°C for 1 Hour.	49
Figure 22 – Typical EDS scan of precipitates bonded at 1125°C for 1 hour detecting the presence of boron.	51
Figure 23 – EDS map scan of precipitates adjacent to the braze/substrate interface on a sample bonded at 1170°C for 1 hour.	51
Figure 24 - EDS map scan of the diffusion induced precipitation zone in the base material of a sample bonded at 1170°C for 1 hour.	52
Figure 25 – Microstructure of a joint produced at 1170°C for 4 hours with joint loading.	53
Figure 26 – Fracture surface of a tensile specimen bonded at 1170°C for 4 hours and tested at 850°C.	54
Figure 27 – EDS point scan of precipitates found in the fracture surface of a joint bonded at 1170°C for 4 hours and tested at 850°C.	55
Figure 28 – Schematic diagram of micro-hardness testing locations.	56
Figure 29 – Hardness data for samples bonded without joint loading.	57
Figure 30 – Hardness data for ETMT tensile samples processed with joint loading.	58

Figure 31 – Element concentration profile of a joint held at various temperatures and times.....	62
Figure 32 – Schematic of the interlayer dissolution mechanism.	67
Figure 33 – Nickel-Boron phase diagrams generated using Thermo-Calc and (A) Ni-DATA Superalloys Database [77] (B) Kaufman Binary Alloy Database [76] (C) Nickel-Boron phase diagram [46].....	73
Figure 34 – Residual liquid measurement of samples processed at 1070°C, 1125°C and 1170°C.	76
Figure 35 – The linear relationship between $\ln(m)$ and $1/T$ used to measure the apparent diffusion coefficient from TLP bonding experiments in CM 247 LC specimens.	77
Figure 36 – Increase in liquid width with varying isothermal holding temperature and initial gap widths.....	79
Figure 37 – Effect of saturation of MPD in the substrate and supersaturation in the liquid filler metal on solidification time.....	80
Figure 38 – Change in the dimensionless solidification rate constant with temperature..	81
Figure 39 – Required processing time with initial gap sizes at varying temperatures.	82
Figure 40 – Schematic diagram of interface node. The liquid/solid interface is shown by the dashed line and is located in sub-system $S_k = X = S_2$	87
Figure 41 – Validation of the moving boundary model against other MBM (Zhou & North and Illingworth) and experimental data from Zhou & North [74, 85].	90
Figure 42 – Moving Boundary Model simulations of TLP bonds at 1070°C, 1125°C and 1170°C with Ni-0.078 at% B substrates and Ni-18.1 at% B filler material.	91
Figure 43 – Phenomenological model simulation of TLP bonding at 1070°C, 1125°C and 1170°C with Ni-0.078 at% B substrates and Ni-18.1 at% B filler material.	98

List of Symbols

Analytical Model Symbols

$C_i^{\infty,S}, C_i^{\infty,L}$	Initial solute concentration of species i in a specific phase, mol/m ³
C_i^{SL}, C_i^{LS}	Equilibrium solidus and liquidus concentrations for species i respectively, mol/m ³
D_i^S, D_i^L	Diffusion coefficient of the solute atom in a specified phase, m ² /s
D_{eff}	Effective diffusion coefficient proposed by Shewmon, m ² /s
D_o	Pre-exponential term for the diffusivity of a solute atom, m ² /s
h	Half-liquid thickness, m
K^α, K^β, K	Dimensionless growth constants
Q	Activation energy of diffusion, J/mol
R	Universal Gas Constant = 8.3144 J mol ⁻¹ K ⁻¹
T	Temperature, K
t	Time, s
x	Thickness of the copper interlayer lost through diffusion during the heat-up stage as proposed by Niemann and Garrett. m
W_m	Theoretical maximum width of the liquid, m
Z	Interface displacement by widening via dissolution of the base material, m
ρ_S	Density of the solid substrate, kg, m ³
ρ_L	Density of the liquid interlayer, kg/m ³

Moving Boundary Model Symbols

${}^i C_i^{S_k}$	Concentration of species i in sub-system S_k at time t , mol/m ³
f^L	Liquid phase fraction
I_k	Interface k
$J_i^{I_k}$	Flux of solute species i across interface I_k , mol/m ² s
S_k	Vector denoting sub-system k
Δt	Time step, s
X	Vector indicating sub-system containing the solid liquid interface
\bar{V}_m	Molar volume, m ³ /mol
x_i	Molar fraction of solute species i
Δz	Sub-system width, m

Phenomenological Model Symbols

g	Gibbs energy of a phase, J/mol
g^{ref}	Reference Gibbs energy, J/mol
g_{mix}^{id}	Gibbs energy of ideal mixing, J/mol
g^{ex}	Excess Gibbs energy, J/mol
g_i^o	Reference Gibbs energy of species i in a specific phase, J/mol
L_{jk}	Interaction parameter for the calculation of the excess energy
ΔG_i^*	Activation energy for the diffusion of species i , J/mol
G_i^j, G_i^{pj}	Interaction parameters for the species p and j
L_{ij}^k	Phenomenological parameter evaluated at the interface k , mol m ² J ⁻¹ s ⁻¹
L_{ij}	Phenomenological parameter evaluated at a subsystem
L_{ij}^S, L_{ij}^L	Phenomenological parameters evaluated at the equilibrium concentrations as defined by local equilibrium in the specified phase, mol ² m ⁻¹ J ⁻¹ s ⁻¹
M_j	Atomic mobility of species j , mol m ² J ⁻¹ s ⁻¹
M_o	Product of the atomic jump distance squared and jump frequency, m ² /s
$\mu_j^{S_k}$	Chemical potential of species j in sub-system S_k , J/mol
$\nabla \mu_j^{I_k}$	Chemical potential gradient of species j across the interface I_k , J/mol

Nomenclature

ADB	Activated Diffusion Brazing
ADH	Activated Diffusion Healing
CALPHAD	CALculation of PHase Diagrams
DFB	Diffusion Brazing
DS	Directional Solidified
DTA	Differential Thermal Analysis
EDM	Electro Discharge Machining
EDS	Energy Dispersive Spectrography
ETMT	Electro Thermo Mechanical Tester
EBW	Electron Beam Welding
GTAW	Gas Tungsten Arc Welding
HAZ	Heat Affected Zone
LBW	Laser Beam Welding
LIPIB	Liquid Infiltrated Powder Interlayer Bonding
LPM	Liburdi Powder Metallurgy™
MBM	Moving Boundary Model
MPD	Melting Point Depressant
PAW	Plasma Arc Welding
PWHT	Post Weld Heat Treatment
SEM	Scanning Electron Microscope
SX	Single Crystal
TLIM	Transient Insert Liquid Metal
TLP	Transient Liquid Phase
TLPS	Transient Liquid Phase Sintering

Acknowledgement

The author would like to thank his supervisors, Dr. Roger C. Reed and Dr. Ainul Ahktar for their invaluable guidance and encouragement throughout this work. I am grateful for the financial support and helpful discussions with Dr. Prakash Patnaik of the IAR NRC.

As a considerable amount of equipment was created for this study, a great many thanks go out to the technical support staff at UBC for their assistance with special mention to Rudy Cardeno, Ross McCleod, Carl Ng, Dave Torok and Mary Mager. In addition, I would like to acknowledge the invaluable aid provided by Matt Brooks of the NPL, UK for assistance on the ETMT.

I would also like to thank my family and friends for their encouragement over the years and I would like to dedicate this thesis to them.

Chapter 1

Introduction

A high bypass gas-turbine engine (Figure 1) is composed of four sections. A fan located at the front of the engine accelerates the incoming air producing thrust. A portion of the incoming air is passed through the core of the engine which is passed through a compressor, compressing it into a high pressure stream that is mixed and combusted with fuel in the combustion chamber located in the midsection. The hot, high pressure off-gas stream is passed through the end section consisting of a series of turbine blades which extract energy from the gas to power the compressor and fan sections. But long before gas-turbines were envisioned for use as jet engines, they were being developed for use as superchargers in aircraft internal combustion engines to provide a pressurized air/fuel mixture, because of the lower air pressure at higher altitudes [1].

In the 1940s major advances in the gas turbine prompted a need for high strength alloys capable of being operated at elevated temperatures. It was found that the compressor outlet and turbine inlet temperatures are direct factors for engine efficiencies prompting the development of materials with superior properties. The term "Superalloy" was coined for a group of materials that were designed for this purpose and encompasses a range of materials including nickel, nickel-iron, cobalt and titanium base alloys.

While the history of the development of the jet turbine engine is intertwined with the advances in superalloys, there have been many other applications where these materials with superior strength, high temperature capability and resistance to corrosion and oxidation have found a home including land-based turbines, helium reactors, heat exchangers, furnaces and sour gas equipment.

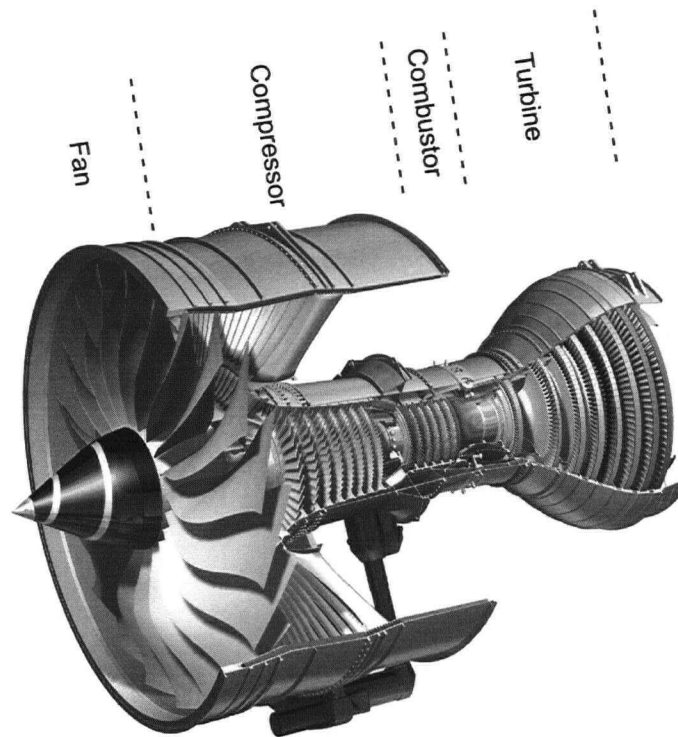


Figure 1 – Cut away diagram of the internals of a modern high-bypass gas turbine aero-engine (Rolls-Royce Trent 1000) [2].

Superalloys are created from carefully tailored microstructures from which these materials inherit their properties. However, due to the harsh operating environment, the resulting damage accumulated by superalloy components limit their operating life. In the case of high performance components, the high cost of their fabrication makes it economical to repair damaged components even though complicated repairs may cost up to 2/3 of the cost of a new component [3].

A number of repair techniques are available for revitalizing hot engine components including fusion welding, brazing and more recently Transient Liquid Phase (TLP) bonding. The TLP bonding process is a repair process that is derived from high temperature brazing. However, unlike brazing, TLP bonding depends on the diffusion of melting point depressants (MPD) out of the liquid, subsequently raising the melting temperature of the liquid which induces solidification isothermally. With sufficient homogenization time, this allows a joint to be produced that has properties similar to those of the base material and avoids unwanted precipitation of secondary phases [4]. The creation of successful joints however requires the optimization of processing parameters as insufficient processing time or temperature results in poor joint microstructures, whereas excessive processing time results in poor economics. The development of repair technologies has traditionally been empirically based with emphasis only on process modeling in recent years [5]. With process modeling, the optimal processing conditions can be estimated without excessive experimentation thus resulting in cost and time savings.

The purpose of this work is to examine the TLP bonding process and develop a coupled thermodynamic/phenomenological diffusion model for determining the effect of bonding parameters on the nickel-base superalloy CM 247 LC. This alloy is a modified version of the popular polycrystalline superalloy MAR-M 247 which was created in the early 1970s by Danesi & Lund at Martin Metals Corporation (now Lockheed-Martin, USA). Modifications were made for improved directional solidification castability in thin walled structures such as gas turbine blades. Further modifications of the composition of CM 247 LC* have led to the series of nickel-base single crystal superalloys designated by the CMSX* name which are also used in turbine blade applications [6]. Experiments were performed in parallel to validate the model and to assess the quality of the joints produced by TLP bonding using various processing parameters. What follows is an overview of the metallurgy of superalloys, their repair techniques and TLP bonding.

* CM 247 LC and CMSX is the trademark of Cannon Muskegon Corporation (Muskegon, MI, USA)

Chapter 2

Literature Review

2.1 The Metallurgy of Superalloys

The critical role that superalloys played in the development of the gas turbine engine has been such that the limits of the materials properties have become the limits of the engine. The role of a turbine blade is to extract power from a hot stream of gas which generally imparts immense stresses on components. Higher operation temperatures are pursued to bring about increased efficiency which brings about reduced fuel consumption. Impurities in the fuel cause hot corrosion and the hot gas stream quickly oxidizes unprotected surfaces [7]. At the high temperatures and stresses employed by gas turbine engines, most materials tend to creep over time making them dimensionally unsuitable for the task. Since the materials operate in a temperature range from room temperature up to near their melting temperature, the issue of phase stability is critical. The reasons for the remarkable properties of superalloys can be found in their microstructure.

2.1.1 Superalloy Microstructures

The desired microstructure of a superalloy component is dependant on the role of that component. In turbine disc applications, the low-cycle fatigue from high loads during take-off and landing operations and low centrifugal forces experienced by these

components prompts the use of a fine grain equiaxed microstructure. Such a microstructure has superior fatigue resistance but relatively low resistance to temperature and environment. Whereas, in stationary turbine vanes and rotating turbine blades, components are typically made of high temperature resistant alloys which can be equiaxed or columnar grained or even have a single crystal structure depending on the proximity to the gas inlet. These components have superior creep resistance and stress rupture properties in addition to high temperature strength, corrosion, and oxidation resistance. The elimination of transverse grain boundaries in columnar grain structures and the elimination of all grain boundaries with single crystal technology resulted in improved high temperature creep properties because of the elimination of grain boundary sliding. Because of the high temperature and centrifugal stresses placed on these components, turbine blade alloys are compared to each other by their stress rupture properties. Figure 2 shows the increase in temperature capability with the development of better alloys and structures. CM 247 LC has similar temperature capability as MAR-M 200 Hf DS [8].

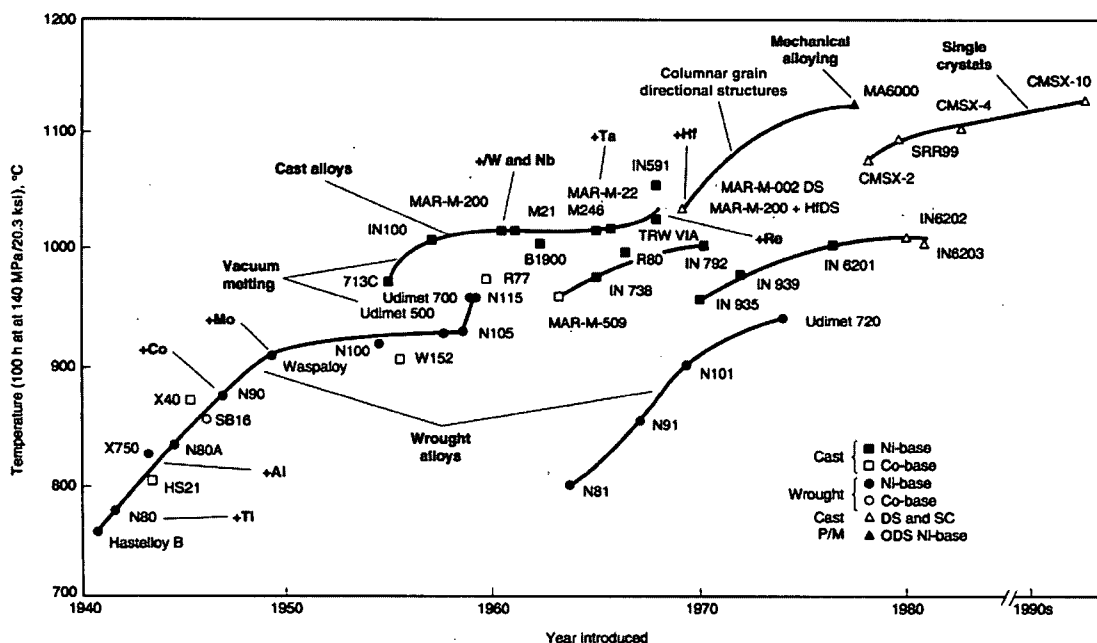


Figure 2 – Increases in temperature capability of superalloys over their historical development [9].

The primary constituent phases of most modern nickel-base superalloys are:

- 1) γ phase, FCC austenitic
- 2) γ' phase, ordered $L1_2$ intermetallic
- 3) carbides

The γ phase is the continuous austenitic matrix comprised primarily of Ni with solid solution strengthening provided by Co, Cr, Mo, W. While the alloy obtains a large portion of its strength from the γ phase which is a solid solution, the majority of the strengthening is gained from the ordered γ' precipitates found within the γ grains.

The γ' phase is an intermetallic with an ordered $L1_2$ structure represented by an A_3B compound where relatively electronegative elements, such as Ni or Co fill the 'A' position, and electropositive elements like Al, Ti or Ta fill the 'B' position. Thus, typically in a nickel-base superalloy, γ' could have the chemical formula $(Ni, Co)_3(Al, Ti, Ta)$ [10]. The γ' phase has a primitive cubic $L1_2$ crystal structure with the Al atoms forming the cubic crystal and the Ni atoms located at the face centers. The morphology of the precipitate is governed by the degree of lattice mismatch between the γ and γ' phases. Hagel and Beattie observed that for small mismatches of $< 0.05\%$, γ' precipitates are spherical, between $0.5\% - 1.0\%$ they have a cubic morphology and at those $> 1.25\%$, plates are formed [11].

Carbides are found in polycrystalline equiaxed grain and columnar grain microstructures. In both these alloys, carbon is added to form grain-boundary strengthening carbides which improve the strength by pinning dislocations at the grain boundaries and inhibiting grain boundary sliding [10].

Figure 3 shows the history of evolution of microstructures in typical superalloys showing the beneficial and the detrimental phases.

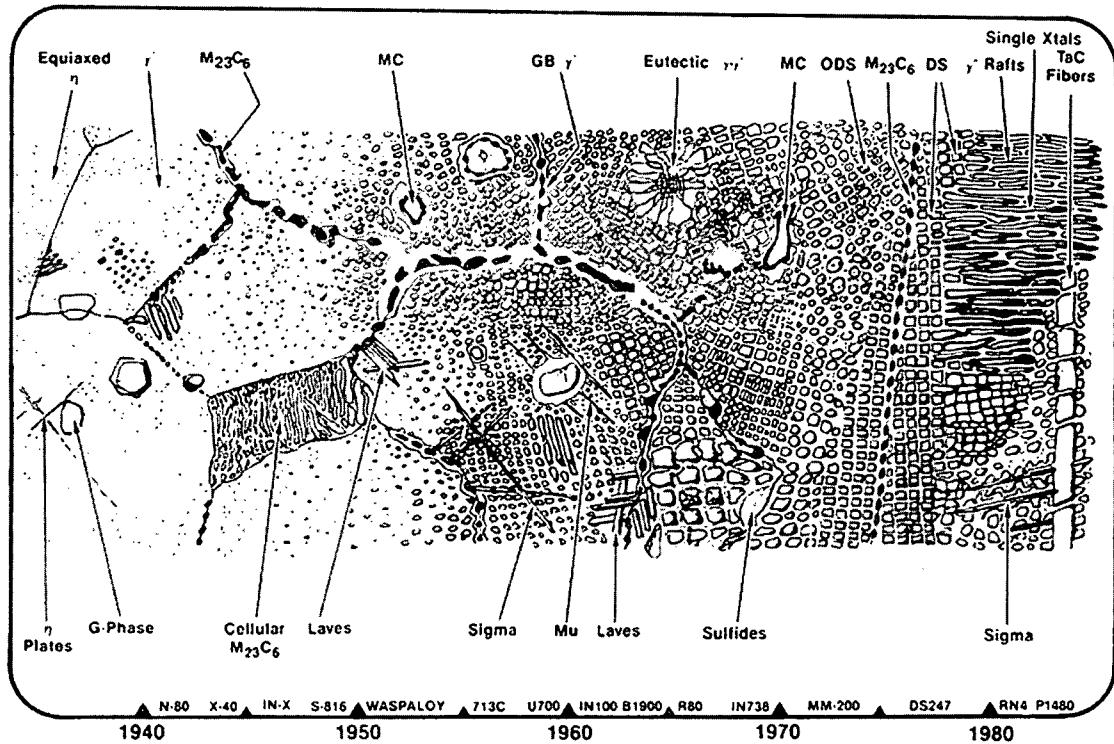


Figure 3 – The evolution of Superalloy microstructures, showing beneficial phases above and deleterious phases below the diagram [12].

In precipitation hardened alloys, the high strength properties are derived from interactions between the ordered γ' precipitates and the motion of dislocations. In order for a dislocation to cut through a γ' precipitate it must travel in pairs (superdislocations) due to a high energy penalty incurred by traveling through an ordered phase. A superdislocation is formed by the coupling of two dislocations linked by an anti-phase boundary [11].

The effectiveness of precipitates is influenced by the particle size and volume fraction. In the case of large precipitates, dislocations find it easier to bow between them and loop around them. With small precipitates, it requires less energy for dislocations to climb and bypass them rather than cutting through. The mechanical synergy between these two phases has been optimized in modern alloys that contain around 70% by volume γ' [13].

2.1.2 Superalloy Chemistry

Superalloy compositions are carefully tailored to produce a microstructure with specific properties. Modern nickel-based superalloys are composed of a complex chemical system comprised of as many as ten elements all of which are tailored for an alloy. Table 1 shows the variations in chemistry between different types of superalloys. IN-738 LC is a polycrystalline equiaxed grain superalloy, CM 247 LC is a directionally solidified (DS) superalloy that later was used to develop single crystal (SX) superalloys such as CMSX-2 (1st generation) and CMSX-4 (2nd generation) [14].

Table 1 – Composition of common Ni-base superalloys, in weight percent.

Alloy	Co	Cr	Mo	Al	Ti	Ta	W	Re	Hf	B	C	Zr	Nb	Ni
Inconel 738 LC	8.5	16.0	1.7	3.4	3.4	1.7	2.6	-	-	0.01	0.11	0.05	0.9	Bal
CM 247 LC	9.2	8.1	0.5	5.6	0.7	3.2	9.5	-	1.4	0.015	0.07	0.07	-	Bal
CMSX-2	4.6	8.0	0.6	5.6	0.9	5.8	7.9	-	-	-	-	-	-	Bal
CMSX-4	9	6.5	0.5	5.6	1	6.4	6	3	-	-	-	-	-	Bal

Elements used in alloying nickel-base superalloys can be categorized into four types. The first type of elements is called γ formers which segregate preferentially into the disordered Ni matrix, stabilizing and strengthening it through solid solution strengthening. Examples of such elements are Co, Mo, W, and Re. In the second category, elements preferentially segregate to the γ' precipitates and serve to stabilize and strengthen that phase. Al, Ti, Nb and Ta are examples of γ' formers. Grain boundary strengtheners form the third class of elements used. Typical grain boundary strengtheners found in polycrystalline superalloys are C, B, Nb, Zr, and Hf. These elements are added because they preferentially migrate to grain boundaries forming carbides which add strength to polycrystalline superalloys. Hf is a notable addition in DS alloys because it assists in strengthening the grain boundaries and avoids grain boundary cracking [14]. Al and Cr are also added because of their tendency to form oxide scales that provide environmental protection from oxidation and corrosion.

2.2 Component Repair Technologies for Superalloys

In cyclical duty engines such as those used in aero-engines, the primary modes of failure are thermal mechanical fatigue, high-cycle fatigue, rubs/wear and foreign object damage [15]. Aero-engine components are complicated cast components with specifically tailored microstructures, have a limited service life with expensive overhaul and replacement costs. The refurbishment of these components is complex; often this involves many steps including cleaning, pre-repair heat treatment, brazing or welding, machining, coating and post-repair heat treatment. However, due to the high costs of replacement it is economical to perform limited repairs to increase the life of components. For the repair of hot section components, the most common techniques used are fusion welding and brazing.

2.2.1 Fusion Welding

Typical blade repairs include restoration of blade tip or tip shroud dimensions to strict tolerances using weld overlay processes. Manual gas tungsten arc welding (GTAW) is commonly used for these tasks but plasma arc welding (PAW) [16], laser beam welding (LBW) [17] and electron beam welding (EBW) [18] are finding increased usage in overhaul processes. Weld filler compositions are derived from lean solid solution strengthened or gamma-prime precipitate strengthened alloys with modifications for component coating compatibility and joint strength. Consequently weld fillers commonly have small amounts of aluminum to increase coating compatibility with aluminide coatings by pack cementation and alloy additions which increase the strength of the joint [15]. However, repairs by fusion welding of superalloys with high aluminum and titanium content (> 6 wt. % Al + Ti) are complicated by micro-fissuring in the heat affected zone (HAZ) during welding and/or during post weld heat treatment (PWHT). Micro-fissuring in these alloys is attributed to the residual stresses induced by the rapid dissolution and reprecipitation of γ' in the weld joint [19,20]. Ojo has reported that a high volume fraction of γ' precipitates also contributes to the microfissuring during

welding by constitutionally liquidating the HAZ [21]. To avoid these problems long pre-weld and post-weld heat treatments are often employed and the chemistry of the filler material is carefully selected to create consequently weaker but more ductile joints than the base material [3]. As such, weld repairs are generally not made in highly stressed areas of engine components. Large microstructural changes are also induced in components repaired by fusion welding which are undesirable in DS and SX components. Many modern superalloys such as IN-617, IN-738 and MAR-M 247 are not easily weldable because of these problems.

2.2.2 High Temperature Brazing

Due to the limitations of fusion welds, high temperature brazing was developed as an alternative repair technique and is widely used for the repair of many engine components. Brazing techniques offer advantages such as low thermal exposures with little or no dissolution of the base material, low mechanical stresses and the ability to join complicated geometries, dissimilar materials and create joints with temperature capabilities approaching that of the base material(s) [22].

In high temperature brazing, a lower melting filler material is inserted between two base material surfaces. The assembly is heated above the liquidus of the filler material but below the melting temperature of the base material. The liquid filler material flows into the gap between the surfaces of the joint by capillary action and solutes from the joint and base material interdiffuse forming a metallurgical bond. The component is held for sufficient time such that the liquid flows and fills the gap. Solidification of the joint occurs during cooling. Following solidification, a post bonding heat treatment is often employed to homogenize the joint and dissolve unwanted secondary phases. Flux-less high temperature brazing is performed in vacuum using pressures in the order of 10^{-4} – 10^{-6} torr on nickel-base superalloys due to their affinity for oxygen at high temperatures. In the aerospace industry, high temperature brazing is used to repair stationary components such as vanes, stators and combustion liners. Critical, highly stressed locations on components are not permitted to be repaired by brazing methods because it

is considered unreliable due to the uncertainty that a crack is completely healed by the repair process [23]. Obtaining a sound brazed joint requires careful consideration of the following:

- Base material characteristics
- Filler material characteristics
- Surface preparation
- Gap design
- Temperature
- Time

2.2.2.1 Filler Alloy Selection

The following characteristics are considered in selecting a braze filler material: wetting of the substrate, flow characteristics, high stability to prevent reactions with the base material, and the ability to alloy with the base material to form a composition having a remelt temperature higher than the bonding temperature.

Wettability can be defined as the degree of local equilibrium established at the solid/liquid interface [22]. It can be measured by the contact angle between a liquid braze filler and the base material. However, adequate wetting does not imply good flow characteristics. The viscosity of a braze filler is also important for flow. Braze filler materials with narrow melting ranges close to eutectic compositions generally have lower viscosities resulting in better flow characteristics than those with wider melting ranges i.e. far from eutectic compositions [22].

A special class of commercial braze fillers called diffusion braze fillers are classified as braze fillers with fast diffusing melting point depressant (MPD). For example a Ni-B-Cr braze filler material is considered a diffusion braze filler because it contains boron as the only melting point depressant which is a fast diffusing interstitial atom. However, Ni-B-Si filler alloys are not considered diffusion alloys because in addition to boron, they

contain silicon which is a slow diffusing substitutional atom. However, all braze alloys have MPDs that diffuse to some degree. Diffusion brazing takes advantage of the diffusivity of these elements to drive the melting temperature of the joint up and dissolve brittle intermetallic phase that form upon resolidification. This can be extremely useful in high temperature joints for aero-engine applications. The compositions of a range of typical nickel-base brazes is shown in Table 2.

Table 2 – Compositions of common nickel-base braze fillers in weight percent.

Chemical System	Trade Name*	C	Cr	B	Si	Ni	Other	Solidus °C	Liquidus °C
Ni-B-Si	MBF 30	0.06	-	3.2	4.5	bal	-	984	1054
Ni-B-Si-Cr	MBF 50	0.08	19	1.5	7.3	bal	-	1052	1144
Ni-P	MBF 60	0.1	-	-	-	bal	11 P	883	921
Ni-B-Cr	MBF 80	0.06	15.2	4	-	bal	-	1048	1091

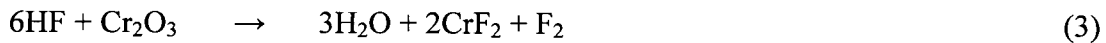
*Metglas Inc. (Conway, SC, USA) [24].

2.2.2.2 Surface Preparation

Braze flow is facilitated by capillary action which results from surface energy effects. The braze alloy contact angle is a measure of the surface free energy between the liquid/vapor, solid/vapor and liquid/solid interfaces. A low surface free energy at the solid/liquid interface results in a small contact angle and better spreading of the liquid over the solid. The presence of surface oxides increases the surface free energy and prevents wetting. Therefore, surface preparation is vital to the quality of a brazed joint. An excellent review on the theory of the wetting of surfaces by liquids in brazing can be found by Gale & Butts [25].

In practice components are chemically stripped to remove coatings, oils and greases followed by mechanical cleaning of the surface by grit blasting to eliminate persistent oxides. For narrow cracks, reactive gas treatments are commonly used [26]. In alloys with low Ti and Al contents hydrogen gas cleaning is deemed sufficient to clean the surface. Alloys with high Ti and Al, contents contain more persistent aluminum and titanium oxides which cannot be broken down in hydrogen gas. Hydrogen fluoride has

proven to be effective for removing stable aluminum and titanium oxides that form on nickel-base superalloy surfaces [27]. The following chemical reactions take place to remove the oxides from the surface [28].



In addition to removal of the oxides on the surface and within cracks, surface depletion of elements such as titanium and aluminum also occurs which enhances wettability by removing oxide formers.



2.2.2.3 Gap Size

Gap tolerances must be created such that they are narrow enough for the braze filler material to flow through them by capillary flow. In the extreme case, if a joint is too narrow then the alloy will be “sluggish” at the braze temperature and will not flow into the gap thus forming voids. On the other extreme, if the gap is too large, then the filler flows out of the joint because of a lack of capillary forces to hold the liquid in place. Moreover, wide gaps have a tendency to form voids due to shrinkage effects. Another drawback of large gaps is the formation of a large amount of eutectic due to insufficient diffusion and solubility of the melting point depressant contained in the braze filler alloy. Typically, narrow gap brazing clearances that range from 0.03 to 0.08 mm (0.001 to 0.003 in.) result in superior capillary action and greatest joint strength [22].

Wide gap joints are needed in applications such as the rebuilding of missing sections of an airfoil or building up the thickness in a section of a component. Wide gap braze fillers are formulated with a mixture of two types of materials often referred to as composite

braze filler materials. The mixture consists of some ratio of the base alloy and a high-temperature braze alloy powder with MPDs mixed in desired proportions. This modified filler material has a desirably inferior flow characteristic to that of conventional braze fillers since not all of the filler is molten at the brazing temperature [23].

2.2.2.4 Brazing Temperature and Holding Time

The brazing temperature is chosen such that it remains above the liquidus of the braze filler but below the solidus of the base material. Excessively high temperatures may cause undesirable changes in the base-material such as annealing, grain growth or warpage. However, higher temperatures also improve wetting, fluid flow and enhance the mobility of melting point depressants resulting in higher remelt temperatures. To avoid heat induced changes, the processing time is chosen to allow sufficient time for complete melting of the braze filler in the joint(s) and to achieve capillary flow and limited to avoid excessive thermal exposure. In a typical brazing cycle, a soak time of 15 – 30 minutes is usually employed.

Heating rates are initially kept low to prevent thermal shock and the possibility of spalling or distortion of the braze filler on the substrate. After a soak at a temperature below the filler material solidus, a fast heating rate to the brazing temperature is employed to prevent the liquidation of the braze filler where the lower melting point constituents melt separately from the bulk. Rapid cooling is usually employed to reduce thermal exposure but it is controlled to avoid cracking or distortion of the part.

2.2.2.5 Brazing Defects

In the event that insufficient time is provided for post bond heat treatment, the brazed joint would have a melt-back temperature lower than expected, especially if unwanted stable low melting phases are formed. Improper surface preparation, excessive gap sizes, entrapped gas or improper fixturing can lead to porosity or cavities within a joint. This can be catastrophic unless detected through non-destructive evaluation. Through visual inspection the exterior would appear sound while damage could exist underneath.

Another limitation of high temperature brazing is the formation of brittle eutectics upon cooling from the bonding temperature. This is caused by insufficient diffusion of the MPDs from the bond region and result in a joint having poor ductility.

An alternative to high temperature brazing is diffusion brazing also known as Transient Liquid Phase (TLP) bonding. Joints in TLP bonding are prepared similarly to high temperature braze joints and share all the same processing equipment. TLP bonding shares many of the advantages of high temperature brazing such as being a capillary joining process which allows for multiple joints to be performed at the same time and a higher degree of geometrical freedom and has the added advantages of avoiding secondary phase precipitation and joint properties similar to the base material.

2.2.3 Transient Liquid Phase Bonding

Transient liquid phase bonding, a derivative of high-temperature fluxless vacuum brazing, is widely used in aerospace, land-based power generation and other industries for primary fabrication and post-service repairs. In common with brazing TLP bonding depends upon the use of a thin liquid-forming interlayer (typically less than 50 μm thick), with a melting-point (initially) below that of the substrate material [25,29,30]. However, unlike in brazing, extensive interdiffusion between the interlayer and the substrate occurs resulting in isothermal solidification during processing and a joint results that has composition and mechanical properties similar to those of the base material. Because of the similarities, furnaces used to perform vacuum brazing, materials such as commercial brazing foils and fundamentals regarding wetting and joint design can be shared.

In the TLP bonding processes, a thin interlayer containing MPDs is placed in between two mating surfaces. The assembly is then heated to the bonding temperature under an inert atmosphere or vacuum. As the assembly is held at the joining temperature, the quickly diffusing MPD components diffuse into the substrate, locally increasing the melting point of the interlayer adjacent to the substrate [4]. In this way, a joint is produced by isothermal solidification without the precipitation of unwanted phases [30].

The solidified structure can be homogenized to reduce the solute gradient at the joint to produce composition, microstructure and mechanical properties similar to those of the substrate [31].

Figure 4 is a schematic diagram of the bonding process. The TLP process is described as consisting of five stages consisting of heat-up, dissolution, widening, isothermal solidification, and homogenization [29]. These can be divided into four distinct phases as follows.

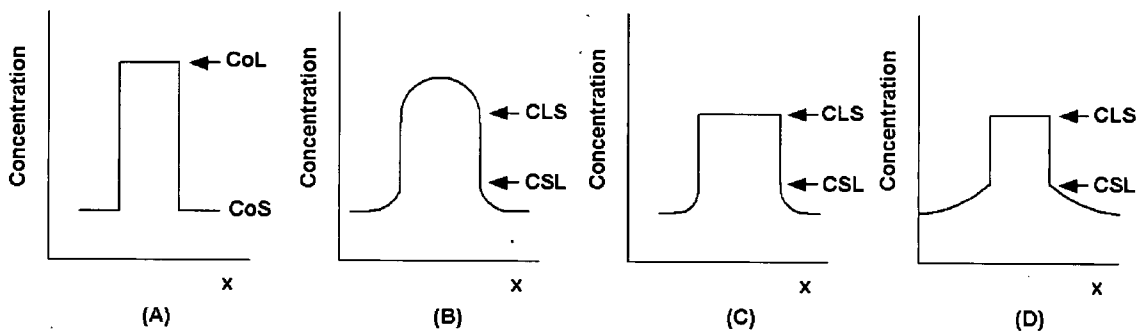


Figure 4 – Discretized stages of the TLP bonding process showing composition variation with distance x . (A) Initial composition prior to TLP bonding (B) Dissolution of the interlayer, (C) Widening and homogenization of the liquid, (D) Isothermal solidification.

Phase I is referred to as the 0th Stage or heat-up. In this phase, the assembly is heated up from room temperature to the brazing temperature. Diffusion of solute from the interlayer into the substrate consequently must be accounted for, especially for thin interlayers where a portion of the interlayer can be consumed during heating.

Phase II consists of two stages: dissolution of the interlayer (if it is not already molten at the processing temperature) and widening of the liquid through dissolution of the base material. These two stages are combined into one phase because they occur simultaneously during bonding. At the bonding temperature, an interlayer can initially be in the liquid or solid state depending on its composition and the chemical system. In the case of a solid interlayer at the bonding temperature, Stage I - Dissolution will occur. In Stage I, MPDs from the interlayer diffuse into the parent material which will simultaneously lower the equilibrium solidus and liquidus temperatures of the substrate

and interlayer materials. This results in the formation of liquid regions at the interfaces between the interlayer and the substrate. In this model it is assumed that discrete solid-liquid interfaces exist between the substrate and liquid and the liquid and the interlayer with two-phase regions that are infinitely narrow. As the assembly is held at the bonding temperature the liquid regions grow and the interlayer is consumed. Stage II - Widening is the widening of the liquid which is shared by TLP bonding with both of the types of interlayers described above. In this stage the MPD continues to diffuse into the substrate material further dissolving the parent material. At the completion of Phase II - Stage II - Widening, the liquid region is assumed to have reached its maximum width which corresponds to when the composition of the liquid has reached a value where its liquidus temperature is equal to that of the bonding temperature. Similarly, the substrate material immediately adjacent to the solid-liquid interface would have a composition equal to a value where its solidus temperature is equal to the bonding temperature.

Phase III is called isothermal solidification. This is the most time consuming phase since it depends on the width of the liquid created by the dissolution and widening of the joint and the relatively slow rate of diffusion of the MPD through the solid substrate. During this stage, the MPD continues to diffuse into the base material, decreasing the solute concentration in the liquid region driving isothermal solidification. During the isothermal solidification of a binary alloy system, the compositions on either side of the solid/liquid interface are respectively equal to the solidus and liquidus compositions as defined by the equilibrium tie lines according to the local equilibrium assumption.

In Phase IV the solute concentration peaks are reduced in the assembly in the so-called homogenization stage. This process occurs similarly to homogenization processes in a conventional heat treatment. Normally, this stage is continued until the concentration peaks are reduced to a predetermined maximum level. This theoretically will improve the mechanical properties and increase the melt-back temperature of the joint.

2.2.3.1 Variants and Applications of TLP Bonding

Transient liquid phase bonding is a term that has been used interchangeably in the literature with diffusion brazing (DFB) and Transient Liquid Insert Metal (TLIM) bonding. In many cases the authors have not distinguished it from high temperature brazing because there are many similarities between both processes. Also, there have been many patents obtained on similar technologies which utilize common solidification mechanisms but different configurations such as Activated Diffusion Healing (ADH) [32], Liburdi Powder MetallurgyTM (LPM) [33] Transient Liquid Insert Metal (TLIM) [34], Transient Liquid Phase Sintering (TLPS) [35] and Liquid Infiltrated Powder Interlayer Bonding (LIPIB) [36]. Activated Diffusion Braze/Bonding (ADB) [37] is also commonly confused with TLP bonding. In ADB a bond is created by conventional brazing methods, it is then heat-treated to dissolve precipitates that form upon thermal solidification.

TLP bonding can be used to join a variety of material systems including nickel-base superalloys, titanium, boron-aluminum composites and semiconductor materials. The process can also be potentially expanded to include any class of materials where the diffusion of a MPD from an additive interlayer leads to the creation of a liquid and further diffusion of the MPD leads to solidification. Over the last 30 years, several variants of TLP bonding have been produced by various companies and research groups for different materials systems [30] including joining of ceramics [38], intermetallics [39-41] and fabrication of ceramic fiber reinforced metal matrix composites [42].

There are three general classifications of TLP interlayers which have been used in the literature. In Type I processes, the interlayer is a pure metal which is the MPD. It either melts and diffuses into the base material or interacts with the base material to create a lower melting liquid. This type of interlayer exhibits extensive widening of the liquid region [43]. Type II processes use an interlayer composition close to that of the parent and thus the widening/homogenization stage is reduced or avoided. Composite interlayers form the third type. The interlayers comprise of a lower melting constituent

and a higher melting constituent, the latter with a higher level of alloying [34]. These interlayers are particularly useful in filling wide gap TLP bond joints [36].

2.3 Evolution of Microstructure in TLP Bonded Joints

In common with conventional brazing, the quality of the microstructure created in TLP bonding depends on the processing parameters employed. The chemical system, gap size, processing temperature, joint loading, and the microstructure of the base material can all have considerable influence on the final microstructure.

2.3.1 Ideal Joints

In a binary chemical system, an ideal joint that has completely solidified by isothermal solidification would not precipitate secondary phases. In the special case of the bonding of two single crystals, an epitaxial growth mechanism would produce a joint with no grain boundaries [44]. It has been shown that with post-bond solution heat treatment and aging heat treatments it is possible to eliminate all traces of an interface, however, this can take several days of heat treatment [45].

In the event of incomplete isothermal solidification, the residual liquid would solidify in the same way as in a brazed joint. For example, in the case of a binary Ni - 4 wt% B alloy, a Ni₃B eutectic would form from the solidification of the residual liquid (Figure 5).

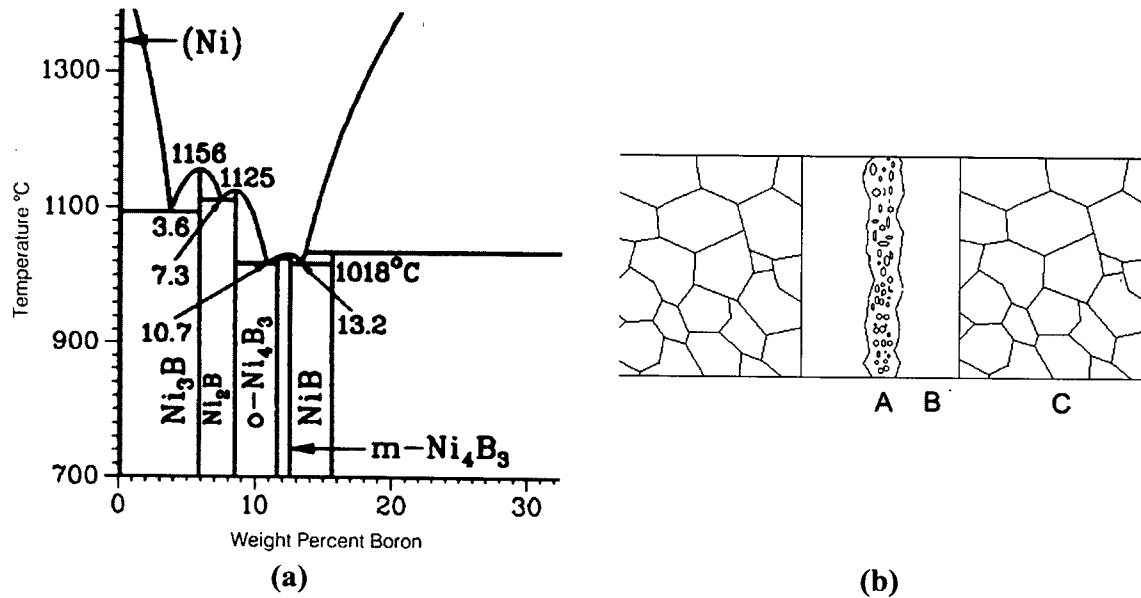


Figure 5 – (a) Ni-B phase diagram [46] (b) Schematic diagram of the evolved microstructure found in an incompletely isothermal solidified binary alloy joint A) Eutectic phase formed from the thermal solidification of residual liquid B) Solid-solution pro-eutectic phase formed during isothermal solidification C) Base material.

2.3.2 Real Joints

In contrast to the chemical systems used in the ideal binary alloy model, real commercial systems consist of complex, highly alloyed base materials and filler materials. This creates complicated chemical systems where deviations from the conventional model may occur. Gap widths which are carefully controlled can still vary slightly and processing parameters such as bonding temperature and joint loading have significant influence over the final microstructure. There is also evidence obtained recently that base material grain boundaries and fast diffusing, low solubility MPDs such as boron can also cause deviations from ideal models of TLP bonding [47].

2.3.2.1 Effect of Composition

The addition of alloying elements in the filler material or substrate increases the complexities of chemical interactions in the bonding system. Although there is limited work reported in the literature on the effects of a change in the chemistry of the base

material, variations in filler material chemistry have been quite extensively researched for brazing nickel-base superalloys [48,49].

In commercial nickel-base braze fillers, boron, silicon, phosphorous or combinations of these are commonly used as MPDs. In TLP bonding, boron is preferred because it has the highest diffusivity amongst the MPDs mentioned and very little boron is needed to depress the melting point of nickel [50]. However, its low solubility in nickel can lead to the formation of brittle intermetallic boride phases decreasing the mechanical properties of the component. Boron also has a strong driving force for combining with chromium to form Cr_3B_4 and Cr_3B_5 which results the adjacent regions becoming chromium depleted and decreased corrosion resistance [51]. However, Wu argues that boron segregation is not entirely detrimental to the mechanical properties of the joint since the tensile properties of some boron containing stainless steels have similar tensile properties to other stainless steels with similar compositions without boron [52,53]. Boron preferentially segregates to grain boundaries [51] forming borides which provide grain boundary pinning resulting in favorable stress rupture properties as it decreases the tendency for grain boundary sliding during high temperature creep. Borides on grain boundaries also inhibit grain growth resulting in smaller grains adjacent to the joint interface than further away from the joint [52].

In single crystal superalloys, the grain boundary strengthening elements are removed because they lead to lower melting temperature structures which can result in non-optimal heat treatment. However, when TLP bonding these alloys, a small misorientation of the crystal structures can lead to the creation of a grain boundary. Since these joints would not have the required grain boundary strengtheners to pin the grain boundaries, the joints would exhibit poor mechanical properties [54]. In properly aligned TLP bonded specimens, mechanical tests performed on single crystal CMSX-2 showed tensile strengths and low cycle fatigue properties similar to base material properties. However, the elongation was notably lower than in the base material, this being attributed to the possibility of borides pinning low angle grain boundaries [31].

As with high temperature braze fillers, the composition of TLP bond fillers benefits from the addition of chromium to increase the corrosion resistance of the joint. This alloying addition however has an impact on the chemical system of the joint. For example, Ohsasa [55] observed that the solidification products of a Ni-Cr-B residual liquid precipitated a ternary eutectic made up of a nickel solid solution, Ni_3B and CrB upon cooling from 1100°C.

Alloying additions present in the base material can enter the joint via a mixing of the dissolved base material with the liquid filler and through diffusion during bonding and the following heat treatment. The degree of interdiffusion increases with temperature but is relatively slow compared to that during isothermal solidification due to the sluggish diffusion of heavy alloying elements [56]. The interdiffusion of these elements is the primary goal of the homogenization stage following completed bonding, because the braze filler often does not contain vital strengthening additions as they can slow the rate of isothermal solidification [45].

2.3.2.2 Effect of Gap Size

For very narrow gaps, it is important to increase the heating rate of the bonding process to ensure proper melting and flow of the filler material. When slow heating rates are used, MPDs are lost to the base material during heating and can prevent the proper formation of a joint due to premature solidification [57].

In wide gaps the need for longer processing times to complete isothermal solidification arises. If a conventional filler material were used in wide gap applications, the total quantity of MPD can quickly saturate the base material, especially in the case of boron where the solubility in nickel is low. This results in long bonding times for large gaps. It is observed that for a given processing time and temperature, an increase in gap size results in an increased volume of eutectic [58].

Composite interlayers have been found to be better for wide gaps than conventional filler materials and are similar in composition to wide-gap braze fillers. TLP bonding with wide gap braze fillers are performed at temperatures above the lower melting point constituent which contains MPDs but below the higher melting point constituent which is highly alloyed but does not contain MPD [34]. As with wide-gap braze fillers, it is intended that the composite filler material have poor flow properties during bonding and thus become useful for filling wide gaps or building up surfaces that have been worn away. The rate of solidification of a wide gap joint is increased when using composite filler materials because of the lower total amount of MPD as well as a decreased diffusion distance since the higher melting constituent acts as a sponge for the MPD [49].

2.3.2.3 Effect of Bonding Temperature

The diffusivity of MPDs increases with temperature, promoting a shorter isothermal solidification stage. An increased bonding temperature also increases the dissolution of the base material due to lower solubility of MPD at the base material-liquid interface. But raising the temperature is generally restricted to avoid damaging the base material microstructure by excessive thermal exposure during long bonding cycles. There has been evidence that elevated temperatures can also influence the rate of isothermal solidification negatively. Idowu observed that the wide-gap TLP bonding of IN 738 LC with a Ni-Cr-B filler material resulted in a slower isothermal solidification rate when bonding at temperatures of 1160°C and 1175°C as opposed to 1130°C and 1145°C due to enrichment of the liquid with solutes from the base material [59]. Slower diffusing MPDs such as Ti, Zr and Nb were suspected to have diffused from the base material into the liquid and influenced the solidification path of the joint.

2.3.2.4 Effect of Joint Loading

Rabinkin reported that a slight load on braze joints improved the microstructure and subsequent mechanical properties of high temperature braze joints due to the so-called “ejection model” [51]. In this model, it is postulated that an increase in joint loading assists in reducing the amount of eutectic by squeezing out liquid from the joint. This

also decreases the time for complete isothermal solidification. A reduction in gap size also reduces the diffusion distances required for heat treatment thus reducing the processing time required to produce a joint with similar structure to that of the base material. Similar observations were made in TLP joints in polycrystalline MAR-M 247 [60] and single crystal CMSX-2 [31].

2.3.2.5 Effect of Grain Boundaries

The existence of grain boundaries in the base material can assist in the breakdown of planar interfaces by liquid penetration along the grain boundaries. Small atoms such as boron are known to segregate to grain boundaries and move quickly along them. It has been suggested that the grain boundaries facilitate liquid penetration into the substrate past the primary joint interface resulting in non-planar interfaces [52]. Grain boundaries have also been shown to accelerate the isothermal solidification rate by increasing the interfacial area [61]. The grain boundary effect was noted by Saida who observed that single crystal materials had the slowest rate of solidification when compared to coarse grain and fine grain materials, with the fine grain material having the highest rate of solidification [62].

2.3.2.6 Deviations from Local Equilibrium

Most models of TLP bonding assume that a state of local equilibrium is reached at the solid-liquid interface. All stages of the bonding process are also assumed to remain sequential and do not occur in parallel. Because of these assumptions, the formation of secondary phases cannot occur if the joint is allowed to completely solidify by isothermal solidification. However, there is recent evidence that deviations from local equilibrium occur in real systems. Ojo observed a deviation from local equilibrium in TLP bonded IN-738 LC with a Ni-Cr-B filler alloy which contained intragranular and intergranular precipitation of Cr and Ni rich boride precipitates in regions adjacent to the braze joint interface at temperatures below the Ni-B eutectic temperature (1080°C) and just Cr rich borides above the Ni-B eutectic temperature (1140°C) but below the Cr-B eutectic temperature (1500°C) [63]. Gale also reported similar evidence in Ni joints made with

Ni-Si-B filler alloys [47]. Ni-rich borides were observed adjacent to bond-lines after 1 minute at 1065°C and remained stable even after completion of isothermal solidification. At 1150°C extensive liquidation of the substrate was observed especially at the substrate grain boundaries. In the experiments performed by Ojo and Gale the concentration of the boron exceeded the solubility limit in the base material resulting in anomalous precipitation of borides. This is counter to conventional TLP bonding models which assume local equilibrium would have taken place and would not account for these precipitates. Gale postulated that this deviation might occur only when fast diffusing MPDs are used and that the unexpected precipitation in the isothermal solidification region occurred prior to the establishment of local equilibrium at the solid liquid interface [25].

Chapter 3

Experimental Methods

The experiments were conducted with two objectives in mind. First, the effect of bonding parameters on the TLP bonding of the superalloy CM 247 LC was examined. This information is currently lacking in the literature. Secondly, quantitative evaluation was made of the microstructures so as to compare the results with the predictions of the modeling work conducted in this work.

Table 3 shows the nominal chemical composition for CM 247 LC. Cast CM 247 LC is a precipitation hardened nickel-base superalloy yielding a 65-68 volume percent fine coherent γ' precipitates [14].

Table 3 – Nominal chemical composition for CM 247 LC in weight percent.

Co	Cr	Mo	Al	Ti	Ta	W	Hf	B	C	Zr	Ni
9.2	8.1	0.5	5.6	0.7	3.2	9.5	1.4	0.015	0.07	0.015	Bal

The braze filler material used in this study is MBF-80, a quaternary Ni-Cr-B-C nickel-base diffusion braze filler. The nominal composition of MBF-80 by weight percent is

15.2 Cr, 4 B, 0.06 C, balance Ni and has a solidus and liquidus of 1048°C and 1091°C respectively as listed in Table 2.

3.1 Casting

Specimens were cast into columnar grain structures with a directional solidification furnace. The casting furnace is shown below in Figures 6 and 7. The raw sample material was obtained from a 7.6 cm diameter x 15 cm long polycrystalline cylindrical charge. This charge contained solidification shrinkage along the cylinder axis and exhibited a large degree of chemical segregation inherent in castings of this type. The charge was divided longitudinally using wire-feed electric discharge machining (EDM) to form uniform wedge shaped charges for subsequent remelting and directional solidification.

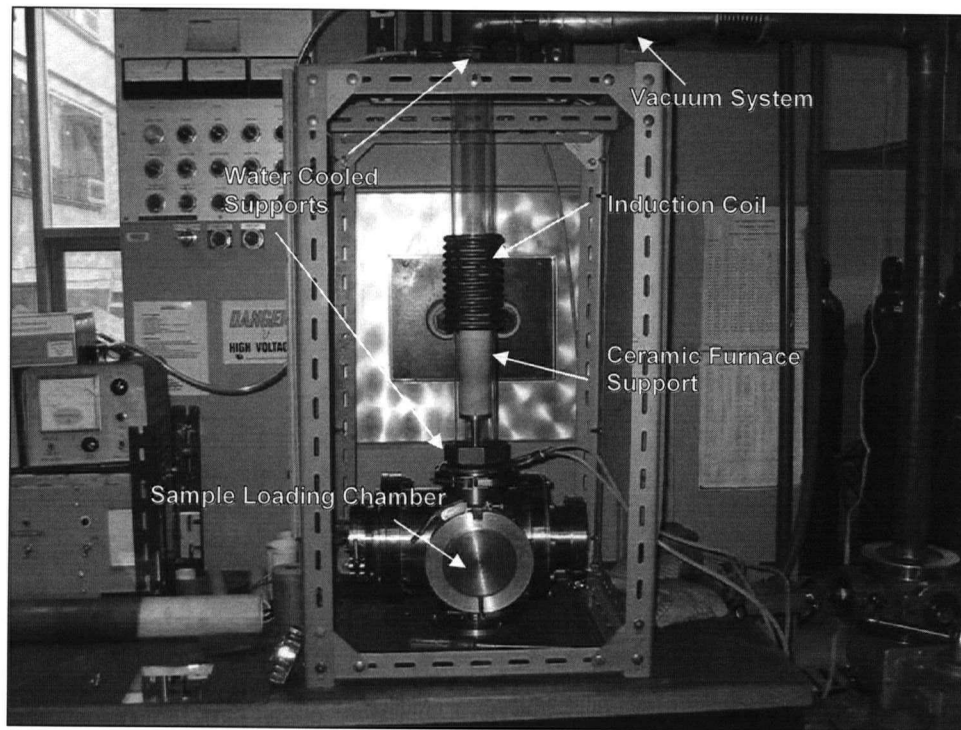


Figure 6 – Directional solidification furnace used for casting CM 247 LC substrates.

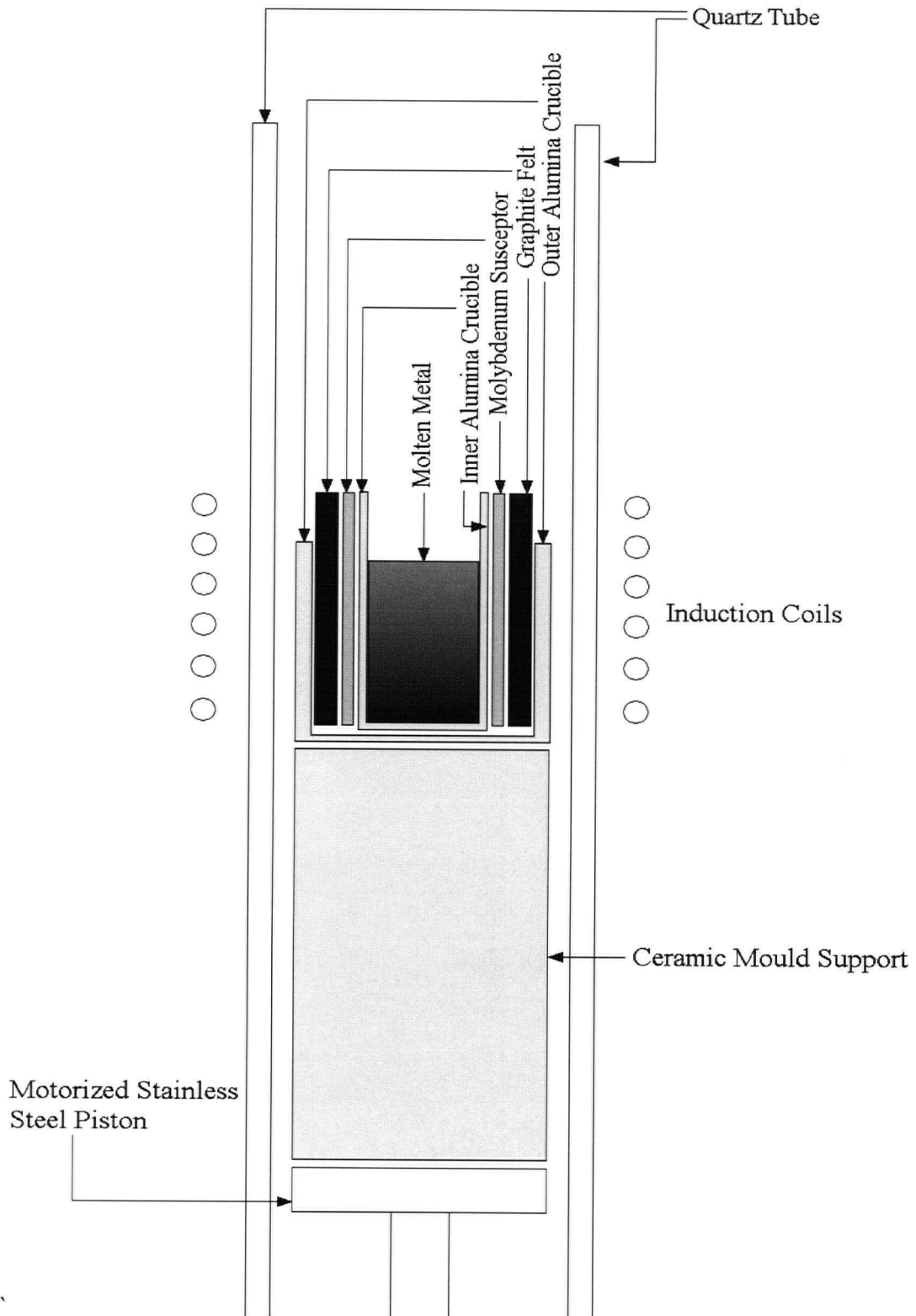


Figure 7 – Schematic diagram of the hot zone of the directional solidification furnace used for casting CM 247 LC substrates.

The directional solidification furnace was constructed by using a 58 cm long x 6.35 cm OD fused quartz process tube to form the hot zone of the furnace. The hot zone was created using a high frequency induction heater and a molybdenum susceptor fixed to the ceramic mould. A stainless steel chamber at the base of the furnace was used to load and unload castings. Melting was carried out in a controlled atmosphere. The following procedure was used. First, a diffusion pump and roughing pump combination produced a vacuum of better than 1×10^{-5} torr. Then, the furnace was back-filled with a static argon atmosphere during casting. Oxidation was further reduced by employing titanium wire as a getter. A titanium wire was heated using a Variac transformer in the cold zone of the furnace during the entire melting and solidification process. In addition, a titanium wire was wrapped around the susceptor and heated via induction heating to prevent oxidation in the hot zone of the furnace.

To effect the translation of the solid/liquid interface across the sample and promote directional growth, the furnace employs a motorized stainless steel platform on which sits a non-cooled ceramic mould support which acts to insulate the stainless steel platform from the high processing temperature. This support is sealed from the surrounding environment by a double o-ring seal located at the base of the furnace. A withdrawal rate of 0.6 cm/min was used for all castings. The cylindrical castings produced by this furnace were approximately 5 cm long x 3.55 cm in diameter.

Heat treatment of the CM 247 LC substrates was performed according to Harris [14]. The treatment consists of solutionizing of the eutectic γ' for reprecipitation as a fine uniform γ/γ' structure and to reduce chemical segregation acquired during casting [64,65]. The solution heat treatment and cooling was performed in an atmospheric superkanthal[†] furnace at 1232°C for 2 hours/1243°C for 2 hours/then quenched by air cooling.

The subsequent oxidation layer formed by the lack of a protective atmosphere was removed via sandblasting. EDM cutting was employed to remove the top of the casting where defects in the casting are more likely and the bottom of the casting where an

[†] Kanthal Super® is a registered trademark of Kanthal (AB, Sweden)

equiaxed grain structure would exist. The top and bottom of each sample was surface ground to produce flat surfaces that were at right angles to the casting direction. The final dimensions of the semi-cylindrical substrates are 2.25 cm long x 3.55 cm diameter.

The microstructure of the cast and heat treated CM 247 LC substrates consists of large columnar grains oriented along the casting direction of the casting. Figure 8 shows the longitudinal section of a directionally cast and heat treated specimen that was polished and etched with aqua regia (1 HNO₃ : 3 HCl). At a higher magnification under an SEM, a finely distributed, coherent γ/γ' precipitation strengthened structure with inter and intra-granular carbides was observed (Figure 9). As CM 247 LC is a DS superalloy, the composition is engineered to produce a favorable distribution of carbides.

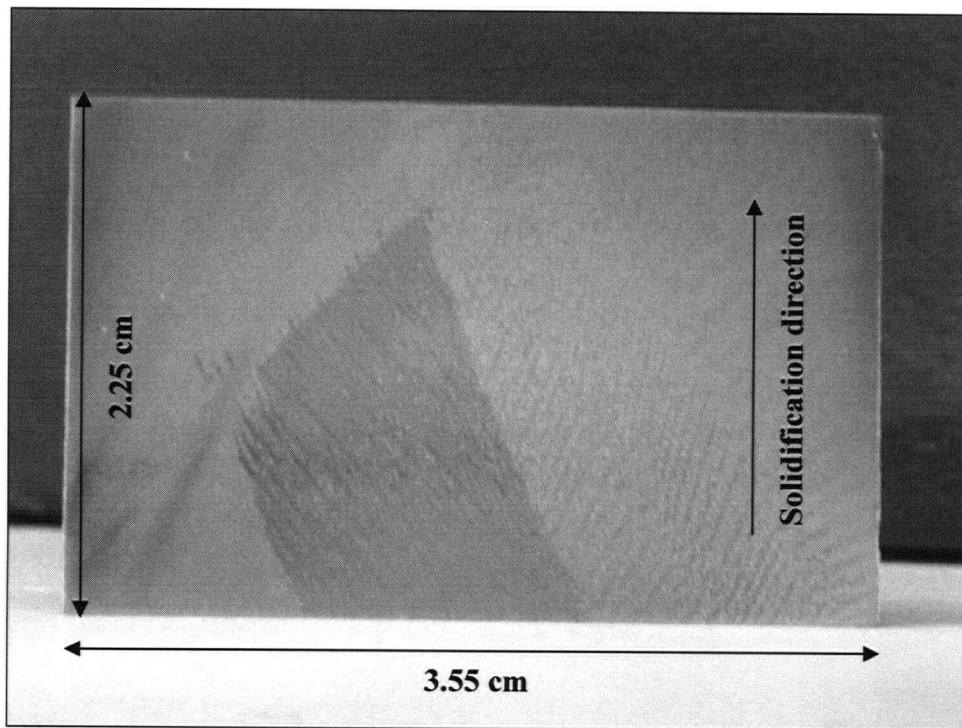


Figure 8 – Longitudinal section of a cast and heat treated CM 247 LC nickel-base superalloy specimen (2.25 cm long x 3.55 cm diameter).

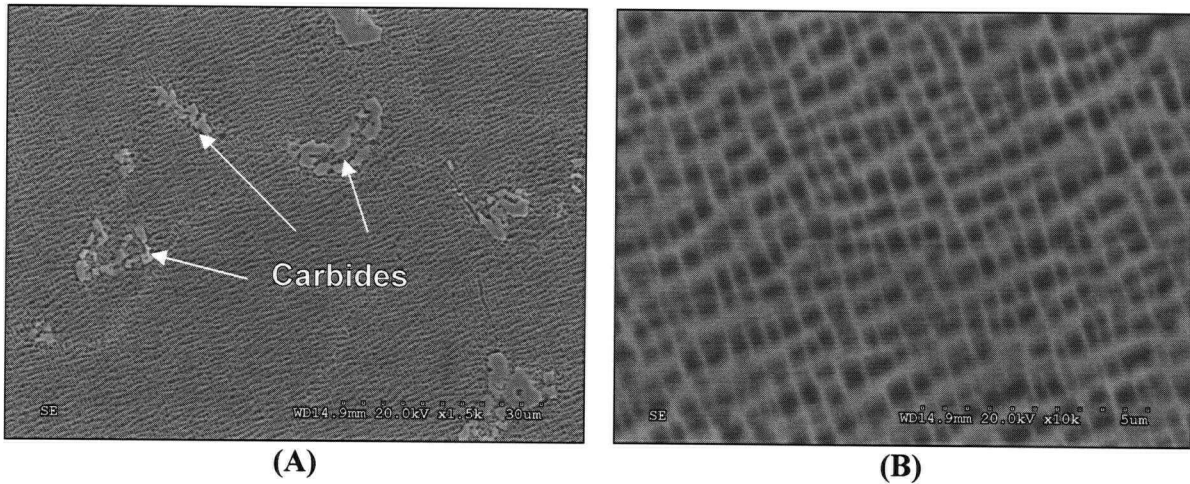
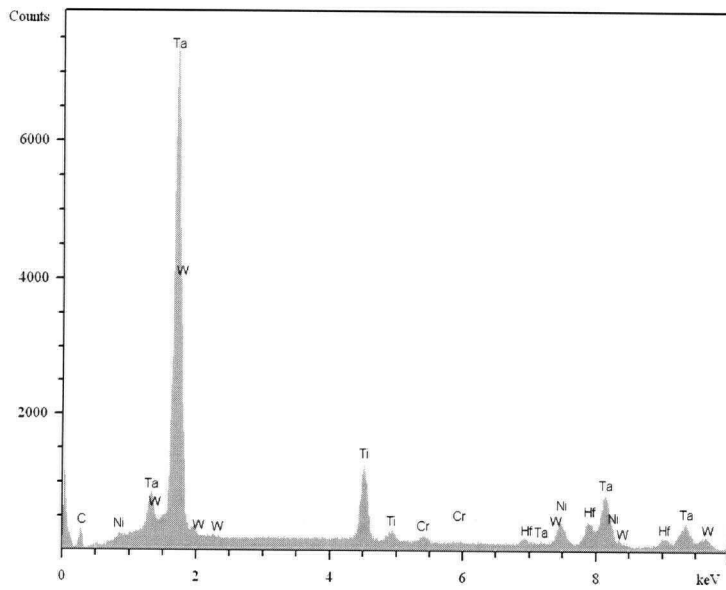


Figure 9 - Cast and heat treated CM 247 LC microstructure consisting of fine cuboidal gamma prime precipitates in a nickel-solid solution gamma matrix and globular carbides.

EDS analysis of the carbide showed them to be titanium, tantalum, tungsten and hafnium rich (Figure 10). These microstructural features were similar to those reported in the literature [14].



	wt%	at%
Ti	10.1	25.8
Cr	0.9	2.1
Co	1.1	2.2
Ni	7.2	15.0
Hf	22.7	15.6
Ta	55.2	37.3
W	2.9	2.0

Figure 10 – EDS scan of a typical carbide precipitate in the cast and heat treated CM 247 LC base material.

3.2 DTA Analysis of the Interlayer Material

Differential Thermal Analysis (DTA) was performed on the MBF-80 braze filler to determine the solidus and liquidus temperatures of the braze filler. This information was then used to select suitable temperatures for the brazing experiments.

DTA was performed with a Linseis L81/1750 thermo gravimetric/differential thermal analysis apparatus under an inert flowing argon atmosphere to limit oxidation. DTA analysis involves the measurement of the temperature difference between the specimen and an inert reference during controlled heating or cooling. During cooling there will always be a slight thermal lag due to differences in thermal properties between the sample and reference. This results in a roughly linear DTA signal. However, large differences in the temperature between the sample and the reference can indicate a change in state in the specimen due to the release of energy during such transformations [66]. In the case of exothermic reactions the DTA signal would result in a peak whereas an endothermic reaction results in a trough. Changes in heating rate can also result in a DTA signal due to the thermal lag produced by differences in heat capacity between the sample and reference. It is important to properly interpret a DTA curve when determining the start and finish points of a phase transformation. For an exothermic phase transformation during the cooling regime, the start of the phase transformation is defined as the onset temperature. This temperature is the point on the DTA signal curve where deviation occurs from linear behavior. The finish of the phase transformation is the point on the DTA signal curve where linear behavior is re-established.

In the present work a 0.1 g sample of the brazing foil was used in the measurement. Alumina crucibles were used because they are inert towards the sample alloy. An empty alumina crucible was utilized for the reference. The sample was heated at a rate of 15°C/min to a temperature of 1200°C and held for 30 minutes. A controlled cooling rate of 3°C/min was used to cool the specimen to 800°C whereupon the sample was furnace cooled to room temperature. Figure 11 shows the DTA curve through the liquid to solid phase transformation during the cooling regime.

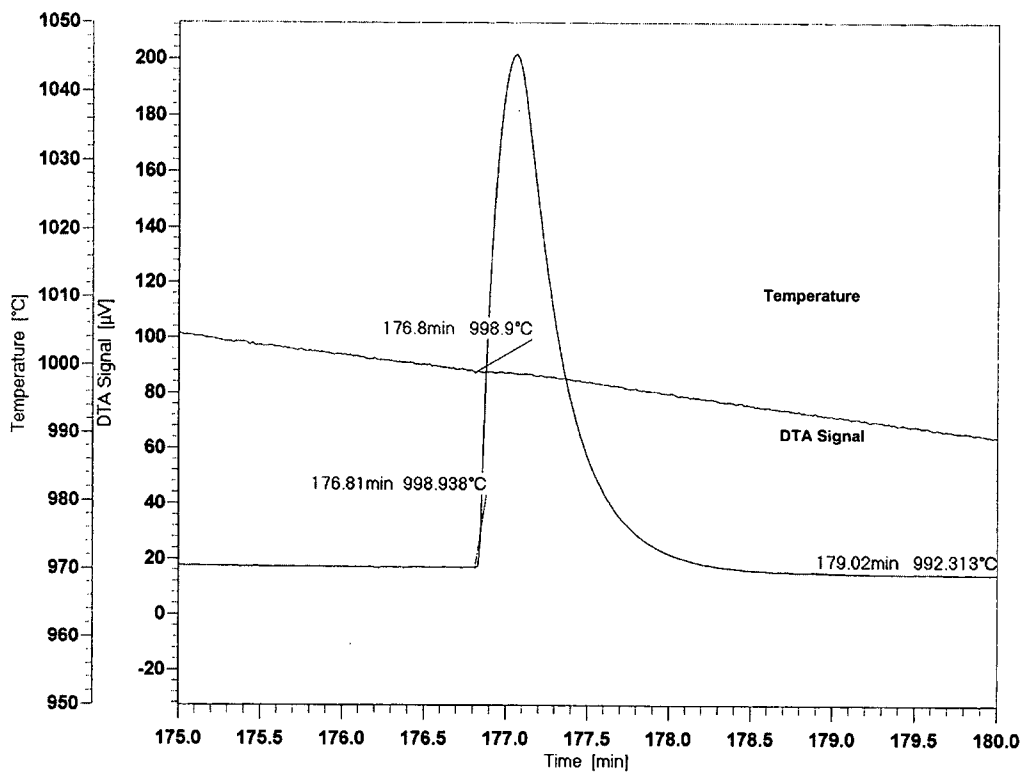


Figure 11 – DTA curve for MBF-80 braze foil during the cooling regime.

The data obtained in the present work show that the solidus and liquidus temperatures are 992°C and 999°C respectively, which is a significant difference from the values of 1048°C and 1091°C reported by the manufacturer [24]. The solidus and liquidus temperatures for a Ni - 4 wt% B binary alloy are 1090°C and 1130°C respectively according to the Ni-B phase diagram. All bonding temperatures were selected above the liquidus temperature of the braze filler but were also either below, in-between, or above the solidus and liquidus temperatures of the Ni - 4 wt% B binary alloy as suggested by Gale [47]. Bonding temperatures of 1070°C, 1125°C and 1170°C were selected.

3.3 Brazing

Butt joints were created by placing a 40 micron thick foil in between two 5 mm thick x 15 mm x 15 mm CM 247 LC substrates cut from the recast and heat treated bars. Spot welding was used to keep the gap width fixed throughout the brazing operation.

To evaluate the tensile properties of the resultant TLP bonds 45 mm long tensile samples were bonded in butt joint configurations as follows. The cylindrical CM 247 LC castings were cut longitudinally using EDM cutting. The ends of each semi-cylinder were then surface ground to a uniform length. This created two equal 22.5 mm long x 35.5 mm diameter semi-cylindrical specimens. A 40 micron thick braze foil was placed between the two substrates and fixed in place by spot welding and placed in a molybdenum brazing support. This configuration resulted in a small load being applied during bonding due to the difference in thermal expansion between molybdenum and CM 247 LC. The bonding configuration is shown in Figure 12.

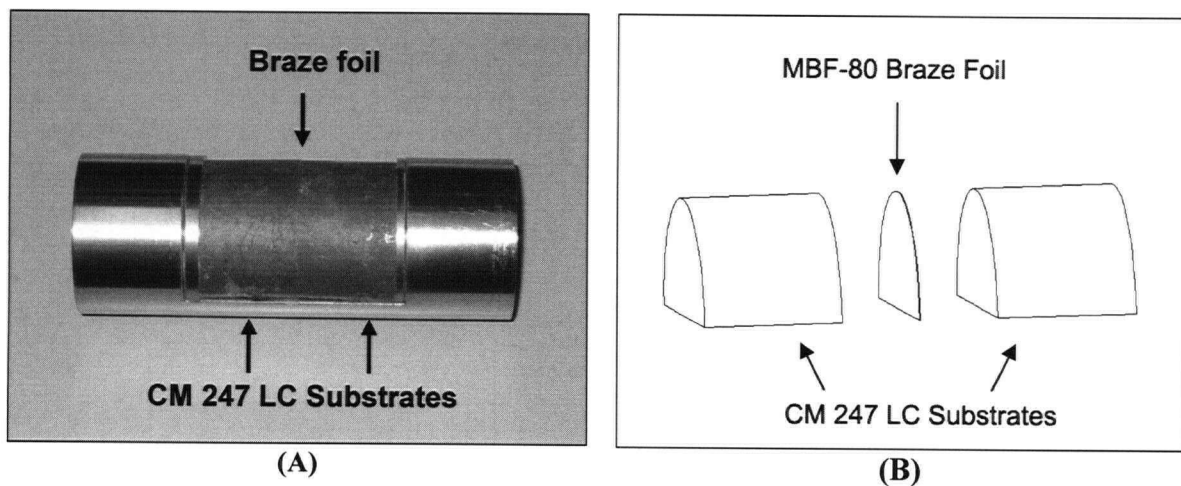


Figure 12 – (A) Molybdenum brazing support loaded with a specimen for the processing of tensile specimens in a butt-joint configuration. (B) Schematic diagram.

Prior to joining, all bond faces were polished flat using 1200 grit silicon carbide paper and ultrasonically cleaned in acetone to leave a flat surface without surface oxides. Upon fixing the braze foil to the substrates by spot welding, the assembly was then loaded into

a tube-type resistance heating vacuum furnace. A K-type (chromel-alumel) thermocouple was positioned close to the joint. High vacuum was achieved by employing a diffusion pump-roughing pump combination on a fused quartz process tube. The process tube was sealed on both ends with water-cooled brass end-caps with o-ring seals. The vacuum brazing furnace is shown in Figure 13.

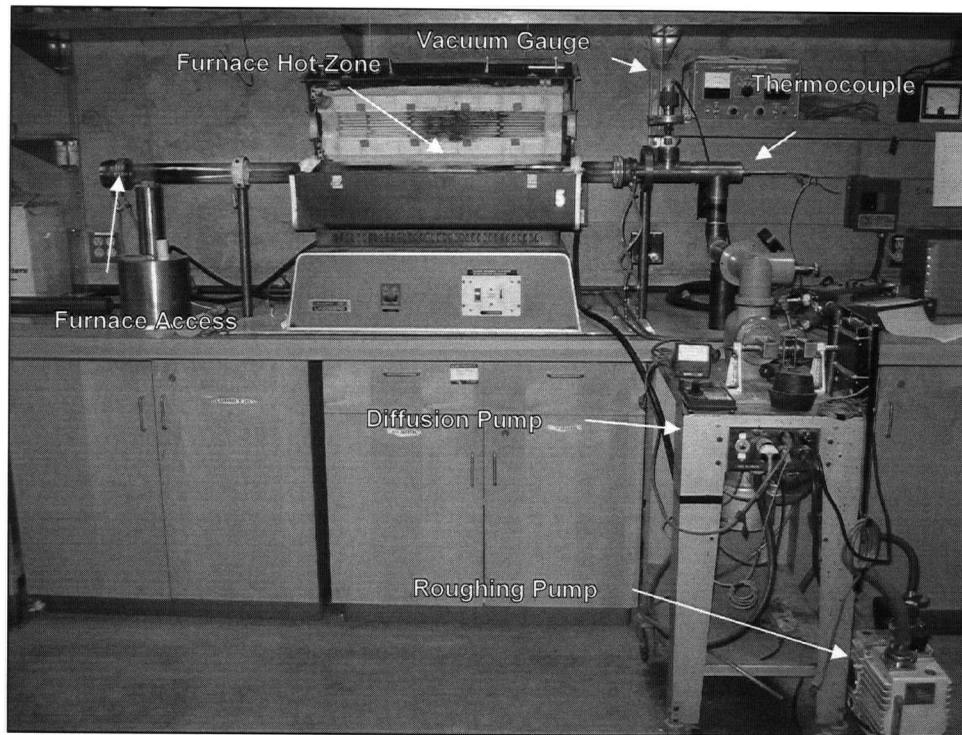


Figure 13 - Vacuum furnace used for the TLP bonding experiments.

Brazing was performed in vacuum at better than 10^{-5} torr to reduce oxidation during processing. Samples were bonded by heating the specimen to the bonding temperature, holding for a specified time and cooled in vacuum by shutting down the furnace. The heating and initial cooling rates employed were measured to be approximately $5^{\circ}\text{C}/\text{min}$ and $9^{\circ}\text{C}/\text{min}$ respectively. Post-bonding heat treatment which is commonly employed in industrial practice to improve joint properties was not used in this work.

3.4 Metallography

Metallographic samples were sectioned perpendicular to the joint interface after joining by an abrasive cut-off wheel to reveal the internal structure of the bond. Samples were polished to a 1 micron diamond finish and etched using Pratt & Whitney Etch #17 (150 mL H₂O + 100 mL HCl + 100 mL HNO₃ + 3 g MoO₃) which dissolves γ' precipitates preferentially [67]. Tensile specimens were machined into 1 mm x 2 mm x 40 mm tensile bars using wire-fed EDM. Eight samples from each brazing condition were created and one specimen from each brazing condition was polished to a 1 micron diamond finish, etched and examined to determine the quality of the bonded joint. These samples were taken to be representative for the other test specimens in the group.

The joint microstructures were examined by optical microscopy using a Nikon Epiphot 300 inverted optical microscope with CLEMEX vision image processing software. Scanning electron microscopy was performed under an accelerating voltage of 20 kV on a Hitachi S-3000N scanning electron microscope. A 5 kV accelerating voltage was used to detect boron. The system is equipped with a Quartz XOne Energy Dispersive Spectroscopy (EDS) system which was used to semi-quantitatively measure the change in chemical composition across the joint. The Quartz XOne software package applies ZAF correction factors to account for the effects of atomic number, absorption and fluorescence on the resulting EDS spectrum. Selected area EDS scans were performed on regions up to 300 microns away from the joint interface on polished but not etched samples to obtain the change in the average chemical composition across the joint.

The EDS analysis of superalloy materials warrants a few points that one must keep in mind. In general, EDS quantification of light elements requires large ZAF correction factors which limit the reliability of these measurements [68]. Thus the boron and carbon content in these structures can only be determined qualitatively. In the same regard, aluminum is also considered a light element in this alloy due to the heavy matrix in which it resides. This also results in large correction factors which can result in large errors. Furthermore, the analysis of cobalt and nickel can lead to some errors as they reside in

similar peaks. A similar argument also exists for the quantification of tungsten, tantalum and hafnium.

3.5 Mechanical Testing

Hardness measurements were made on the various phases contained in the bonded microstructures. Tests were performed on a microhardness tester with a 25 g load. 3 measurements were taken per zone in 5 zones across the joint interface and an average value is reported.

High temperature tensile tests were performed on an Electro-Thermo-Mechanical-Tester (ETMT) designed by the National Physical Laboratory (NPL, Teddington, UK) [69]. The ETMT enables high temperature tensile tests as well as creep and stress rupture tests to be carried out. Heating to the desired temperature is achieved by the ETMT through resistance heating. An R-type 0.1 mm diameter thermocouple (Pt/Pt-13%Rh) was spot welded to the joint interface to measure and control the temperature of the specimen. The strain on the specimen may be obtained in the ETMT either through a measurement of the displacement of the grips by capacitance measurements or through the change in resistance of the specimen. Resistance measurements across the gauge length of the specimen were made by spot welding 0.1 mm diameter platinum 1 mm to each side of the thermocouple. Samples were tested at 850°C with a strain rate of 5×10^{-4} /s. Tests were performed twice for each bonding condition.

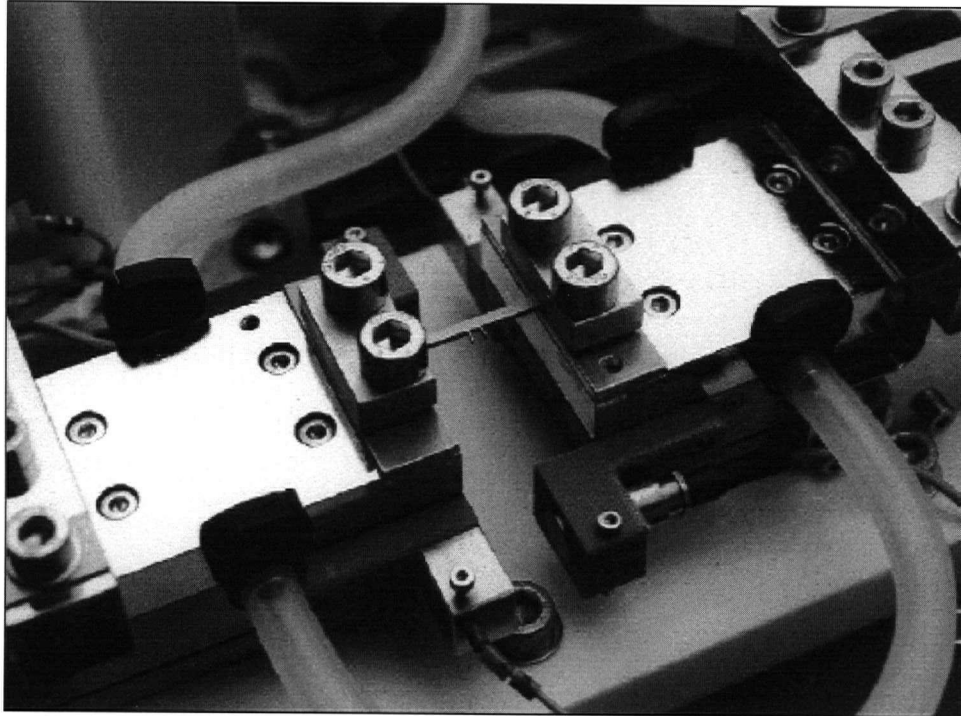


Figure 14 – A test specimen loaded on the Electro-Thermo-Mechanical Tester [69].

Chapter 4

Results and Discussion

The objective of the experiments was to determine the effects of bonding time and temperature on the quality of the TLP bonds produced in the superalloy CM 247 LC. In these experiments, the exposure times selected at a given temperature to produce conditions which would result in partial and complete isothermal solidified joints. Samples in the butt-joint configuration were held at 1070°C, 1125°C and 1170°C each for durations of 15 minutes, 1 hour and 4 hours.

4.1 Microstructure of TLP Bonded Joints

The microstructures as observed on the transverse section are shown in Figure 15. The microstructure of the completely bonded joints consisted of a single solid solution phase. By contrast, incompletely eutectic phases were observed at the joint centerline when isothermal solidification had not progressed to completion. The centerline structure is indicated by **L**. The centerline eutectic phases are bordered by an isothermal solidification zone comprised of a proeutectic solid-solution region which fills the remainder of the joint. Bordering the joint region in both completely and incompletely isothermal solidified joints is a precipitation zone containing globular and acicular precipitates indicated by **P**. Further away from the center of the joint is the unaffected base metal indicated by **B**. The dissolution width is also indicated in the micrographs by arrows. Each of these regions is discussed in the following sections.

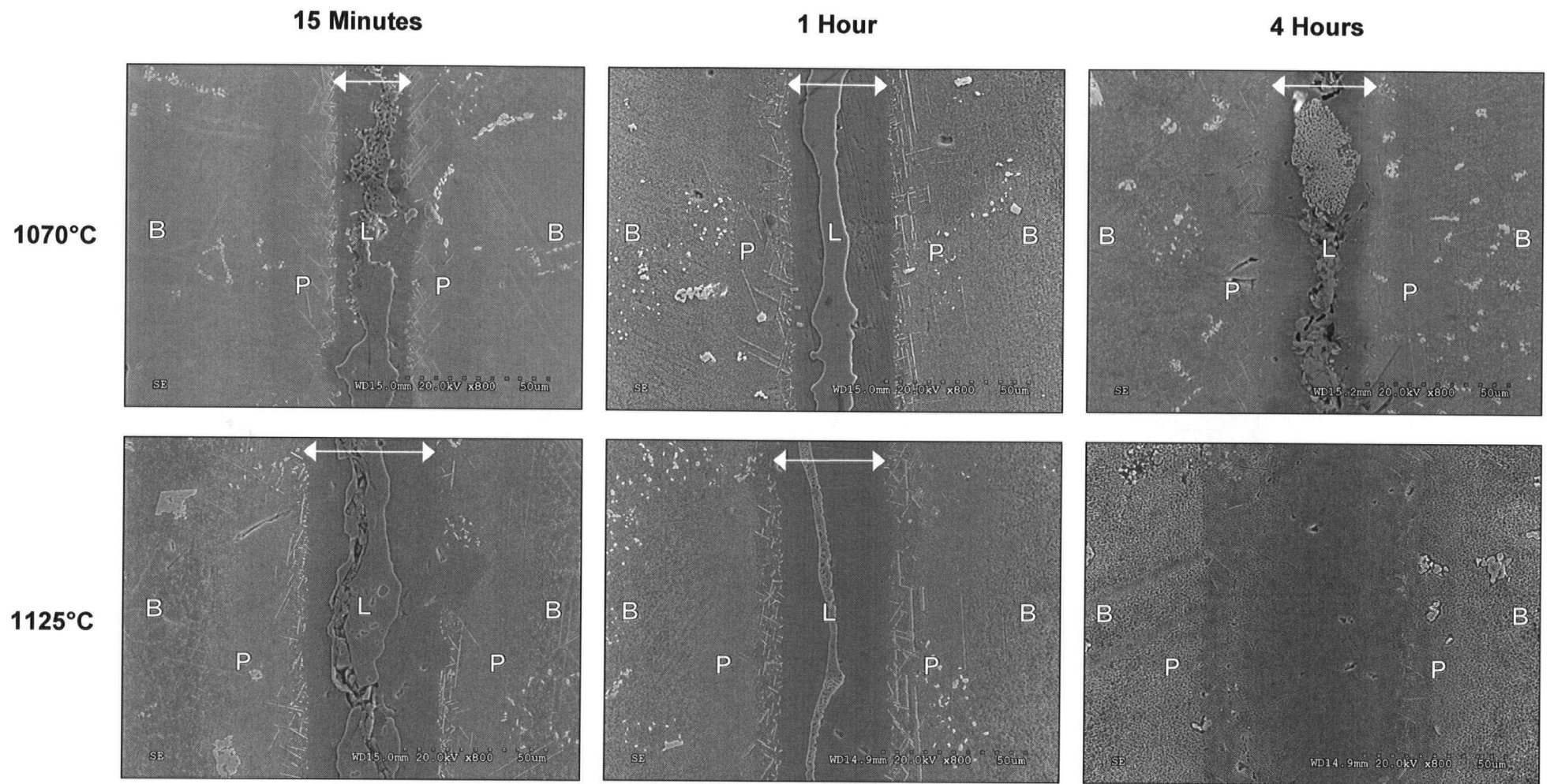
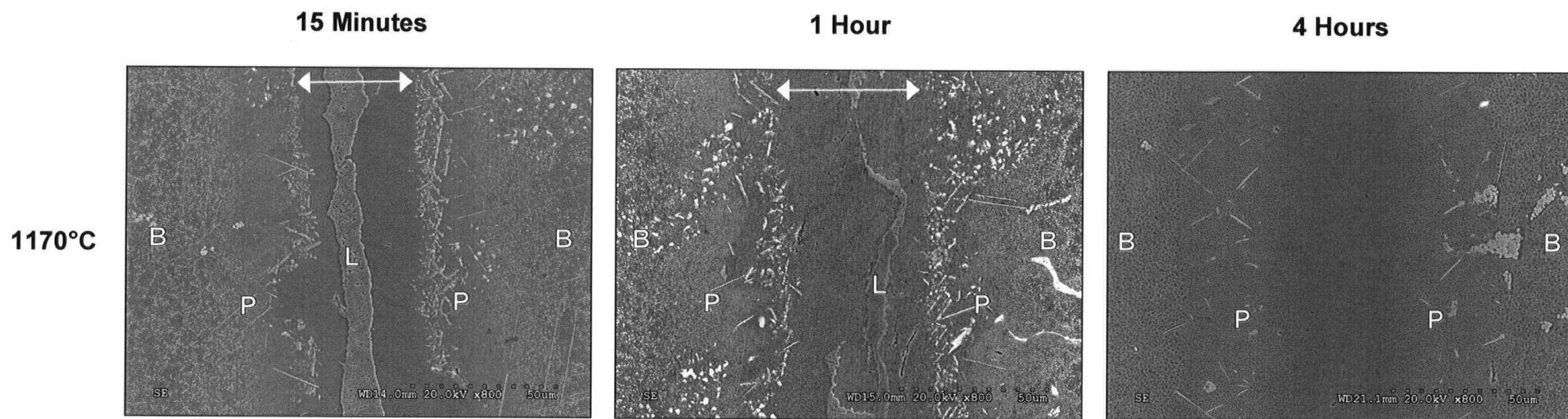


Figure 15 – Typical microstructures of TLP bonds in CM 247 LC processed at various temperatures and times.



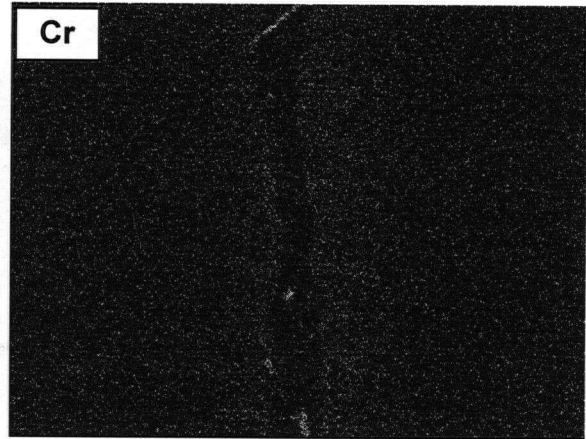
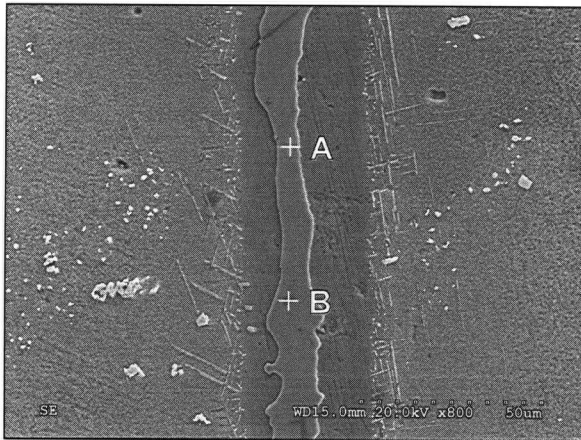
4.1.1 Centerline Eutectic

The centerline eutectic structures are formed as a result of the solidification of the residual liquid in the joint during the cooling of the specimen to room temperature. In Figure 15, the centerline eutectic is indicated by L and is typically found in the center of the joint microstructure. The width of the residual liquid in the joint was observed to decrease with increasing holding time. In the joint produced at 1070°C, the lower bonding temperature resulted in slower diffusion rates for the MPD. At the end of 4 hours of processing, the joint still contained a centerline eutectic structure with a width only slightly narrower than the joint produced after 1 hour holding time. In joints produced at higher temperatures, the isothermal solidification rate was higher resulting in a shorter processing time for the completion of the bond. For example, joints held at 1170°C were nearly solidified after only 1 hour holding due to the higher diffusion rate of the MPD.

EDS scans of the solidified structures in the residual liquid revealed two eutectic phases: a nickel rich phase and a chromium rich phase. In the microstructures observed, the nickel rich phases were present in large volumes in the form of a continuous chain running the length of the joint. The chromium rich phase was present in discrete islands. EDS point scans of these phases detect the presence of boron concentrations in these phases. Using EDS mapping, regions of high chromium content can be detected in the centerline eutectic phases which correspond to chromium borides. Figures 16 – 18 show regions of high chromium content within the braze microstructures produced at 1070°C, 1125°C and 1170°C and the presence of boron in both eutectic phases.

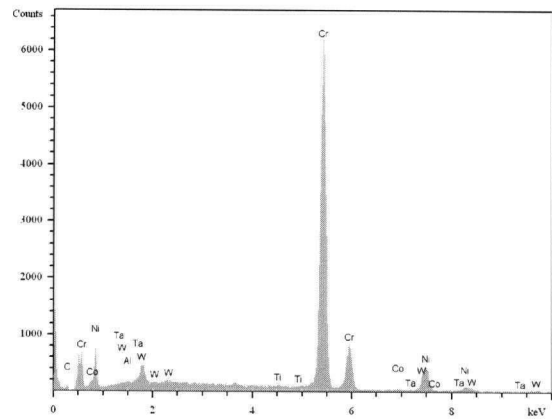
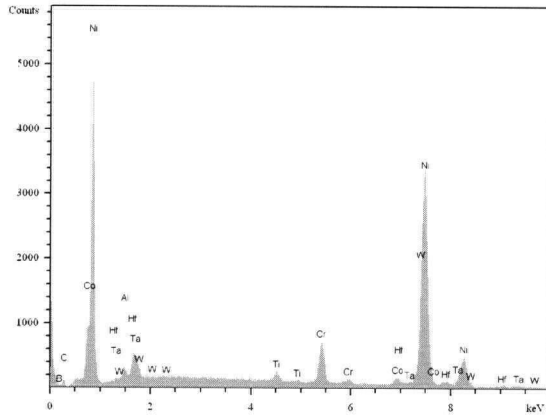
These observations are similar to those of Ohsasa who explored the solidification behavior of residual liquid in the TLP bonding of a pure nickel substrate using a Ni-Cr-B filler material [55]. It was shown that at the processing temperature of 1100°C, a nickel rich solid solution phase was formed by isothermal solidification. Upon cooling, a eutectic reaction producing Ni solid-solution and Ni₃B resulted at 1042°C. A ternary eutectic reaction would follow at 997°C which produced Ni solid-solution, Ni₃B and

CrB. Since these phases have lower solidus temperatures than the base material, the presence of these eutectic phases can have deleterious consequences on the operation temperature these materials can be used at. Furthermore, as these phases form brittle and continuous chains along the length of the joint, the existence of these phases would result in poor mechanical properties.



(A)

(B)



	wt%	at%
Al	1.4	3.2
Ti	1.0	1.3
Cr	6.5	7.5
Co	1.9	2.0
Ni	80.2	83.0
Hf	4.7	1.6
Ta	3.5	1.2
W	0.9	0.3

	wt%	at%
Al	0.3	0.6
Ti	0.3	0.3
Cr	81.5	85.5
Co	0.4	0.4
Ni	12.6	11.7
Hf	0	0
Ta	0.5	0.2
W	4.4	1.3

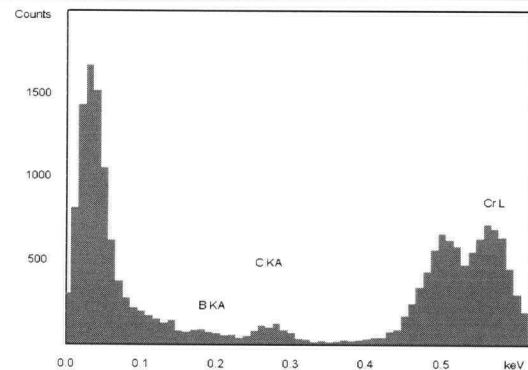
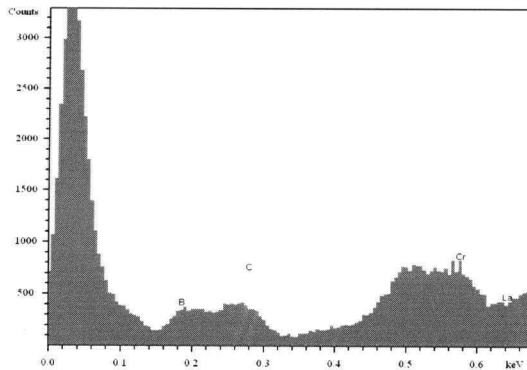
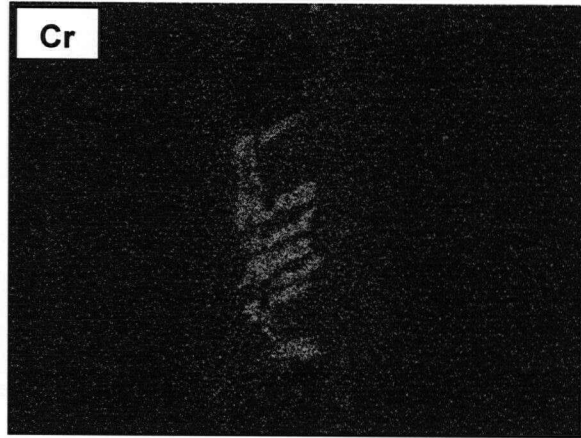
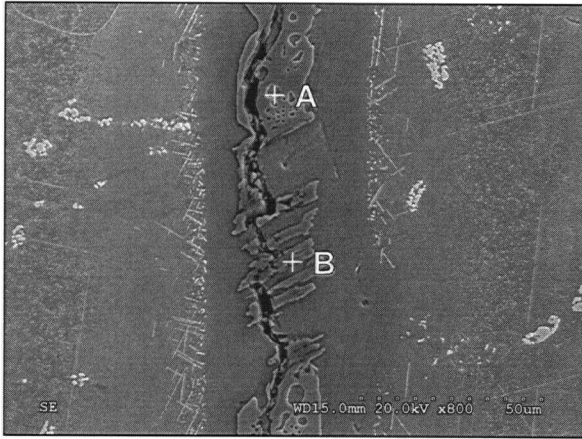
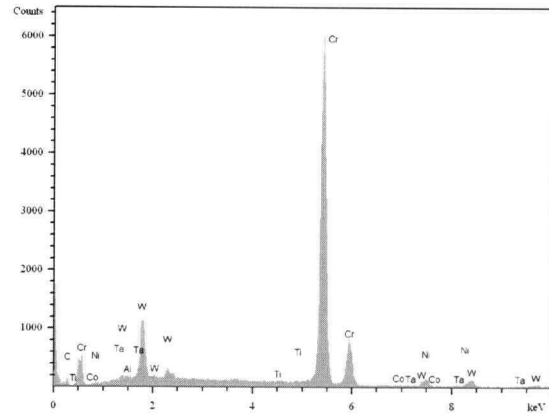
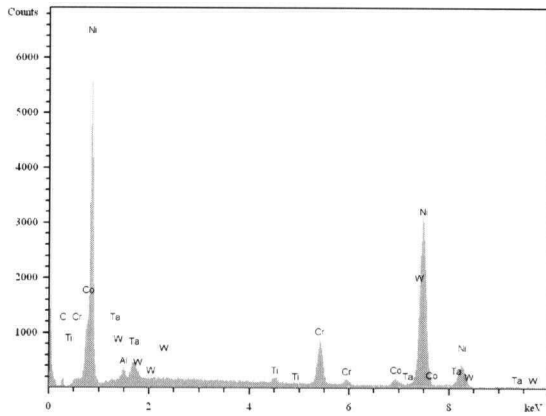


Figure 16 – EDS scans of the centerline phases in a joint produced by holding at 1070°C for 1 hour (A) Nickel rich eutectic (B) Chromium rich eutectic.



(A)

(B)



	wt%	at%
Al	1.9	4.3
Ti	0.7	0.9
Cr	8.6	9.9
Co	2.6	2.6
Ni	78.3	79.7
Hf	2.8	0.9
Ta	3.7	1.2
W	1.3	0.4

	wt%	at%
Al	0.3	0.6
Ti	0.2	0.2
Cr	83.2	91.8
Co	0	0
Ni	3.4	3.4
Hf	0	0
Ta	0.2	0.1
W	12.7	4.0

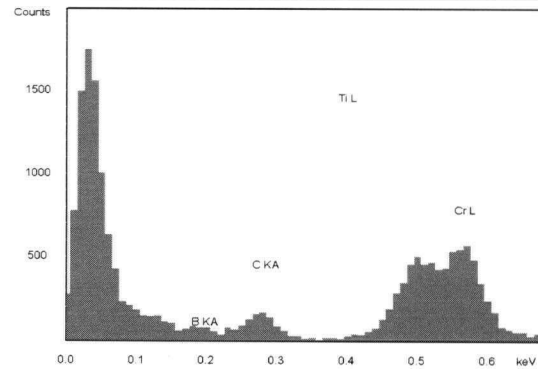
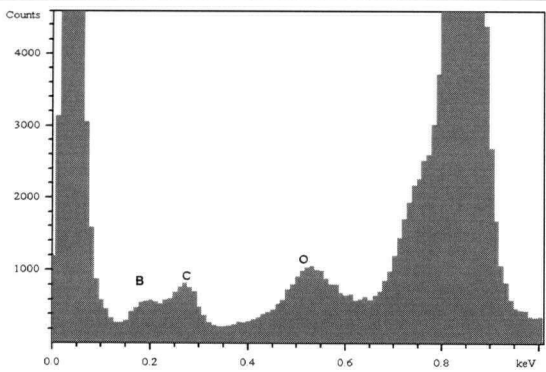
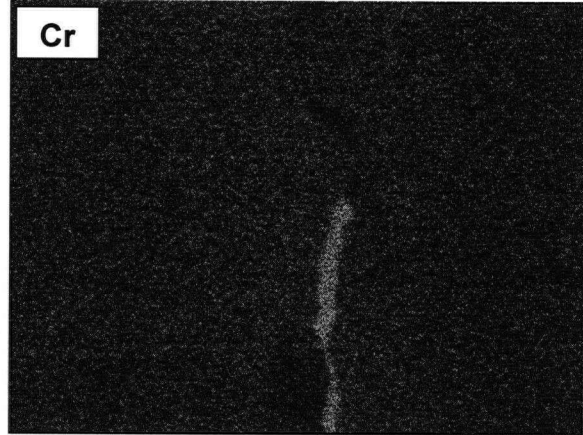
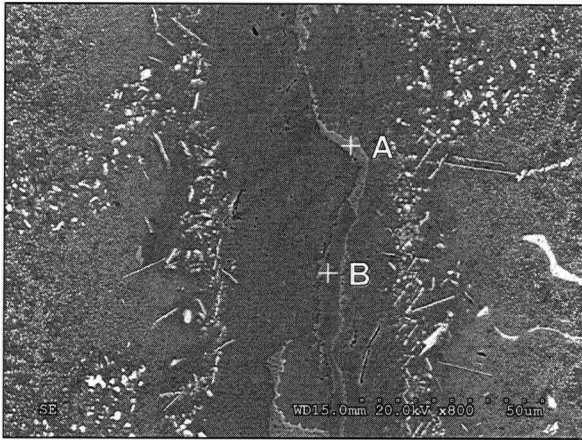
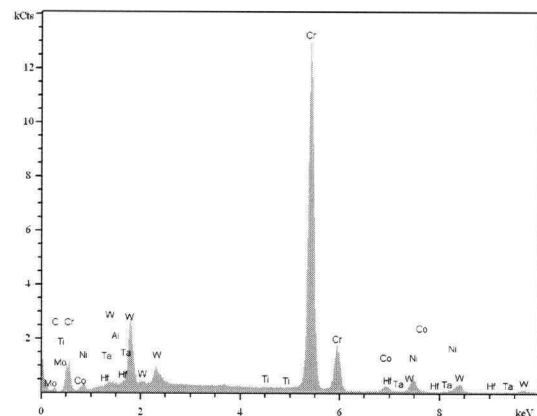
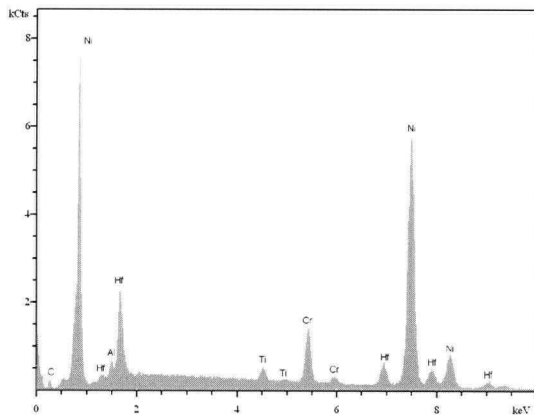


Figure 17 – EDS scans of the centerline phases in a joint produced by holding at 1125°C for 1 hour (A) Nickel rich eutectic (B) Chromium rich eutectic.



(A)

(B)



	wt%	at%
Al	1.30	3.1
Ti	1.13	1.5
Cr	6.62	8.2
Co	4.75	5.2
Ni	68.92	75.7
Hf	14.39	5.2
Ta	2.82	1.0
W	0.07	0.0

	wt%	at%
Al	0.21	0.5
Ti	0.14	0.2
Cr	78.66	87.4
Co	2.09	2.1
Ni	5.92	5.8
Hf	0	0
Ta	0.17	0.1
W	12.8	4.0

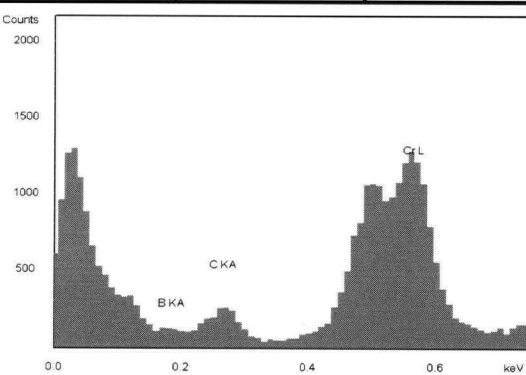
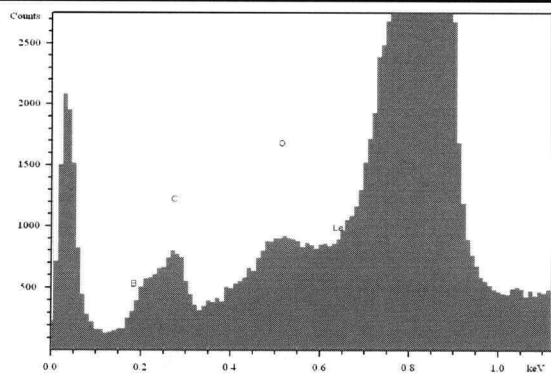


Figure 18 – EDS scans of the centerline phases in a joint produced by holding at 1170°C for 1 hour (A) Nickel rich eutectic (B) Chromium rich eutectic.

4.1.2 Isothermal Solidification Zone

The isothermal solidified region is located adjacent to the centerline eutectic in incompletely isothermal solidified joints. The isothermally solidified microstructure is composed of a proeutectic nickel rich phase and contained a level of chromium initially close to the braze filler composition (Figure 19). In a completely bonded joint, the entire joint would be comprised of this phase. The width of the joint was observed to widen during bonding due to base material dissolution. The final width was found to be a function of the bonding temperature. The widest joint width was found at the highest processing temperature and the narrowest joint was found in the lowest bonding temperature.

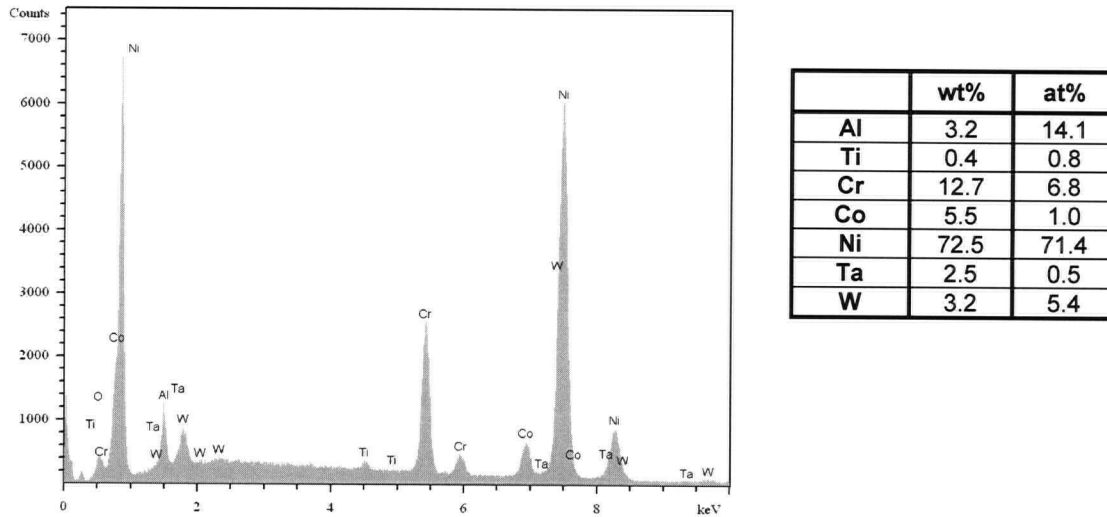


Figure 19 – Typical EDS scan of the isothermal solidification zone in a joint held at 1070°C for 4 hours.

Cuboidal precipitates were found in the isothermal solidification region in the TLP joints processed at 1170°C for all times and in 1125°C after an exposure of 4 hours. The average size of the precipitates closest to the substrate/filler material interface was approximately 0.5 microns and decreases towards the center of the joint. As will be shown later (Figure 34), in joints that were held at the processing temperature for longer times, EDS analysis detected alloying elements not initially present in the filler material in this region due to diffusion from the substrate material. These precipitates are

suspected to be γ' precipitates although this could not be confirmed in the present work. The formation of these precipitates may be the result of the diffusion of γ' forming alloying elements from the base material into the joint. For samples bonded at longer times and higher temperatures, precipitates were found to be larger and extended further into the joint. The longer processing time and higher temperature increase the diffusion distances for the alloying elements in the substrate into the joint, leading to homogenization of the joint. Figure 20 shows the typical morphology of the precipitates observed in the isothermal solidification zone.

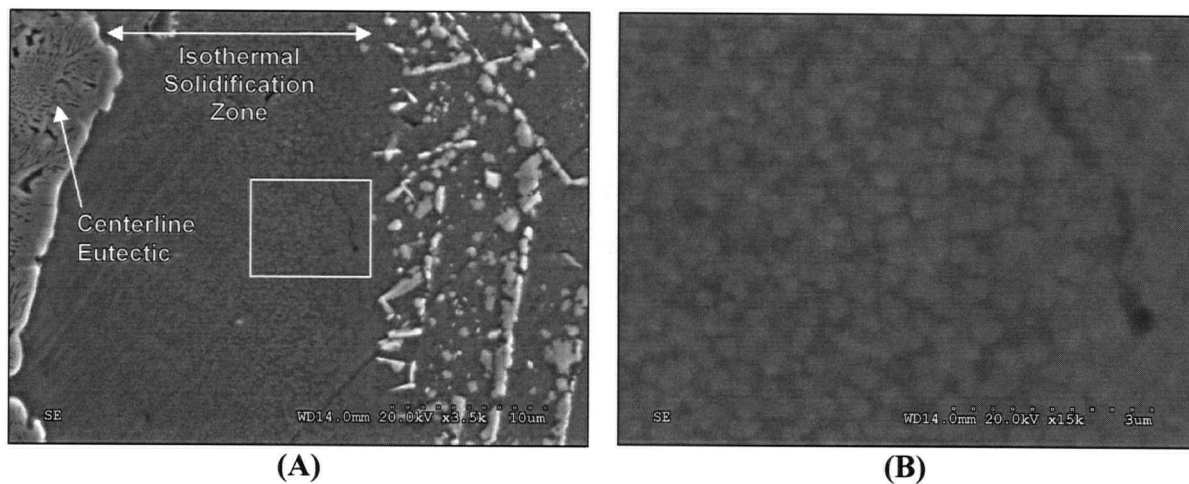
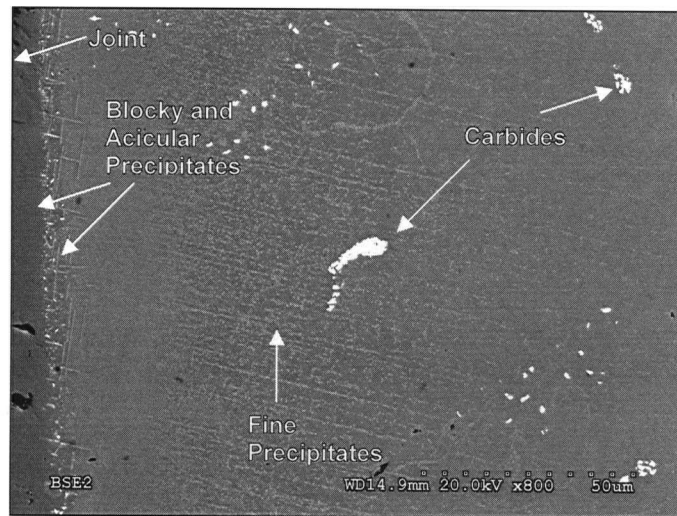


Figure 20 – (A) Precipitation in the isothermal solidification zone of a joint bonded at 1170°C for 15 minutes. (B) Magnified image of the region indicated in (A).

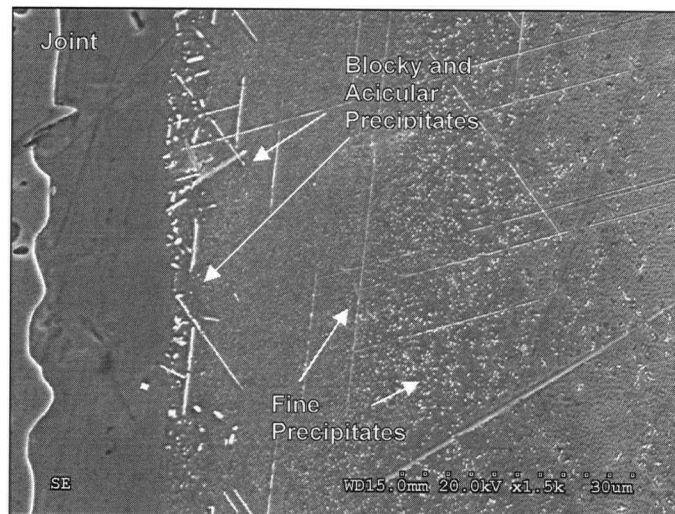
4.1.3 Precipitation Zone

A mixture of blocky and acicular precipitates were detected on the filler material side of the liquid/substrate interface. Further away from the joint centerline were zones of fine precipitates which grew in size with distance from the center of the joint as indicated on Figure 15 by P. These zones were composed of fine precipitates that were observed to have precipitated in the same orientation as acicular precipitates adjacent to the joint interface. In some samples, it was observed that coarser precipitates that were further from the joint centerline coalesced and formed long acicular structures. Comparative photographs are shown in Figure 21 of the precipitation zones in samples bonded at 1070°C, 1125°C and 1170°C for 1 hour.

1070°C



1125°C



1170°C

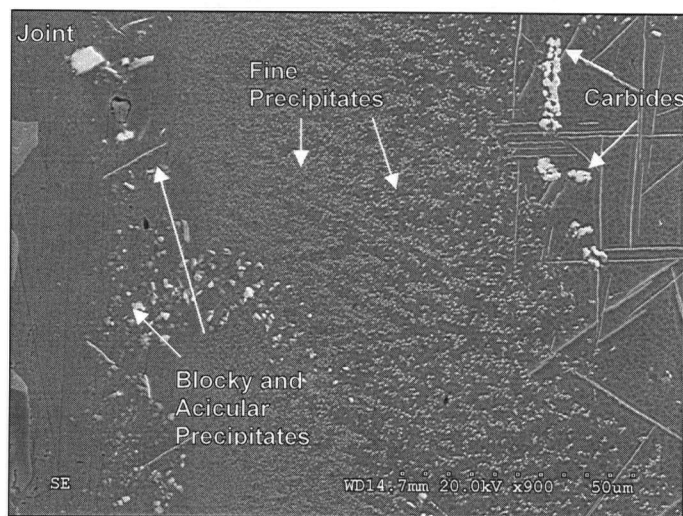


Figure 21 – Diffusion induced precipitation zone in the base material of a joints bonded at 1070°C, 1125°C and 1170°C for 1 Hour.

In the sample bonded at 1170°C for 1 hour (Figure 21 - C), blocky precipitates adjacent to the filler material/substrate interface were approximately 1-2 microns in diameter. Adjacent to this region, smaller densely packed blocky precipitates were present. They coarsened with distance from the center of the joint and reached a maximum size of 0.5 microns in diameter. Still further from these precipitates, acicular precipitates on the order of 10-20 microns long and 1 micron wide were present. Similar observations were made in joints produced at the other two temperatures and other bonding times. These precipitates were also found in the samples that had undergone complete isothermal solidification. Therefore, they could not have formed from the solidification of the residual liquid. The only mechanism for their formation is due to the exceeding of the solubility limit of the surrounding material.

EDS scans of the globular and acicular precipitates showed that they have similar compositions (Table 4). These compositions were similar in all samples. Both phases were found to be tungsten rich and slightly nickel depleted despite having very different morphologies. Boron was also detected in these precipitates indicating that the precipitates may be nickel-borides (Figure 22). The tungsten rich and slightly nickel depleted structures were identified by EDS Map scans. Figure 23 and Figure 24 respectively show EDS map scans of the precipitates adjacent to the filler/substrate interface and in the precipitation zone.

Table 4 – EDS Analysis of globular and acicular precipitates adjacent to the braze/substrate interface and in the precipitation zone of the substrate material in a joint bonded at 1125°C for 1 hour.

Element	Joint/Substrate Interface				Precipitation Zone			
	Blocky		Acicular		Blocky		Acicular	
	wt%	at%	wt%	at%	wt%	at%	wt%	at%
Al	6.0	14.7	3.8	10.7	6.1	14.9	3.9	10.9
Ti	1.0	1.4	0.8	1.3	1.0	1.4	0.8	1.3
Cr	6.7	8.5	10.8	15.6	6.8	8.6	11.0	15.9
Co	6.6	7.4	5.0	6.4	6.7	7.5	5.1	6.5
Ni	51.3	57.4	36.7	47.4	52.0	57.9	37.6	48.3
Hf	1.6	0.6	0.0	0.0	1.7	1.6	0.0	0.0
Ta	3.3	1.2	2.4	1.0	3.4	1.2	2.6	1.1
W	21.9	7.8	38.1	15.7	22.2	7.9	39.0	16.0

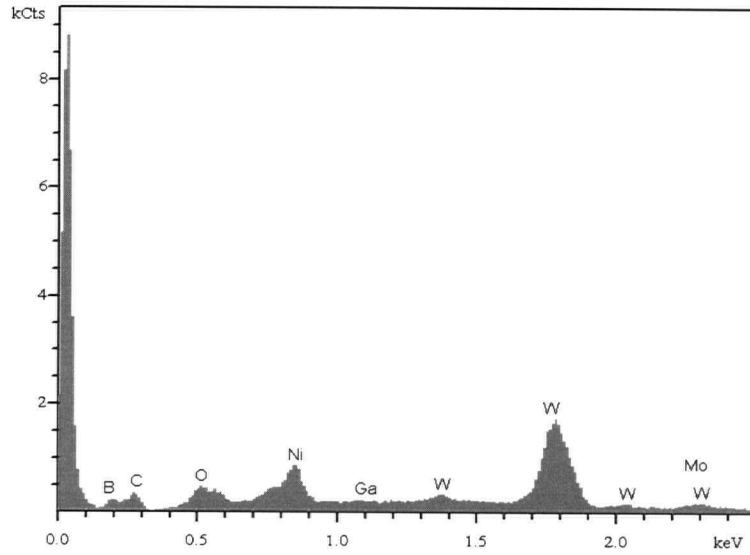


Figure 22 – Typical EDS scan of precipitates bonded at 1125°C for 1 hour detecting the presence of boron.

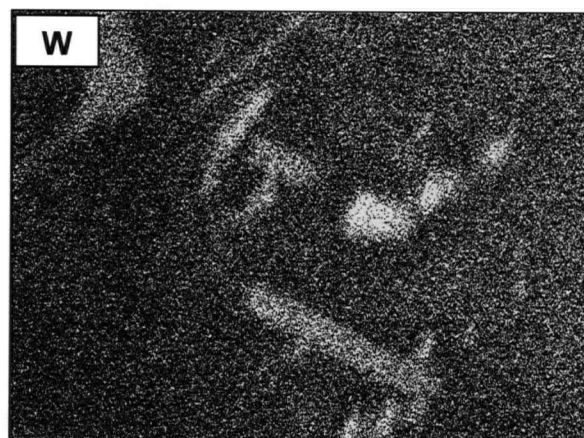
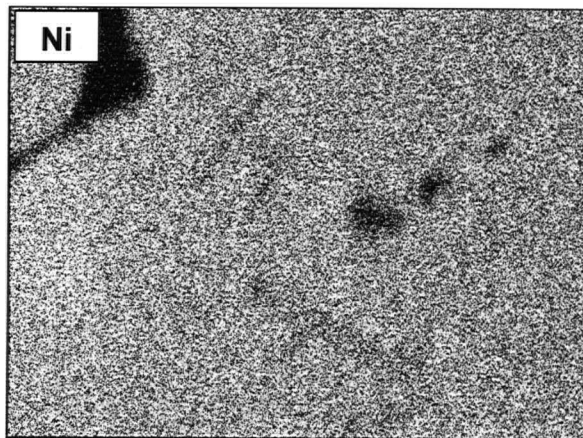
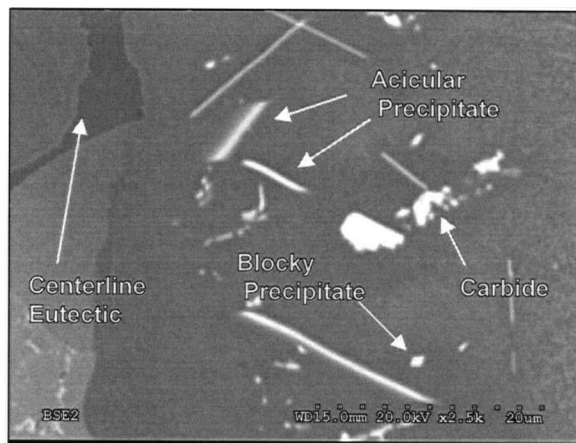


Figure 23 – EDS map scan of precipitates adjacent to the braze/substrate interface on a sample bonded at 1170°C for 1 hour.

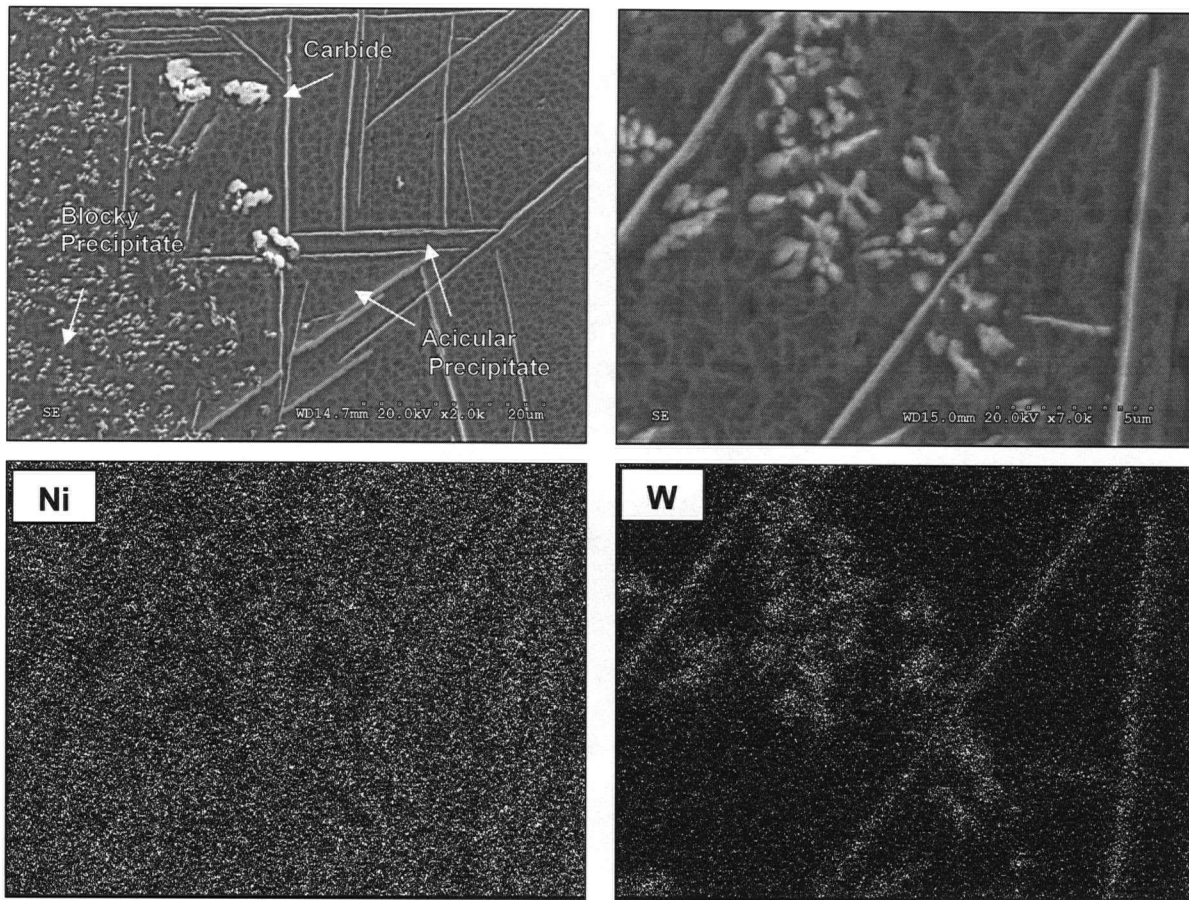


Figure 24 - EDS map scan of the diffusion induced precipitation zone in the base material of a sample bonded at 1170°C for 1 hour.

4.2 High Temperature Tensile Properties

High temperature tensile tests were conducted at 850°C. Joint loading was present in the fabrication of these joints as noted earlier. Nakahashi [60] has reported that loading during brazing improves tensile and stress rupture properties. In the tensile samples produced in this work, the microstructures contained considerably lower volume of residual liquid than in samples produced without loading. For example, a sample produced at 1170°C did not exhibit any eutectic structures even when processed for 15 minutes whereas the specimen bonded without load contained a 20 micron wide centerline eutectic structure. The typical joint width was also found to be approximately 30 microns from an initial width of 40 microns. This indicates the expulsion of liquid

from the joint which would accelerate the solidification process. Precipitation products in the substrate were found to be similar in morphology to those observed in samples processed for longer periods of time without bond loading (Figure 25). High temperature properties are reported in Table 5 and compared to values found in the literature [14].

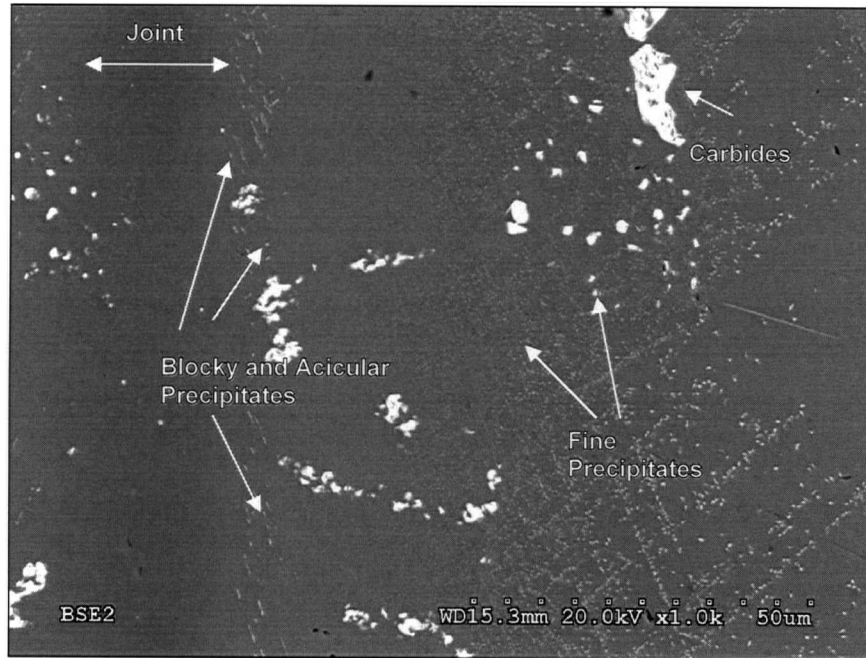


Figure 25 – Microstructure of a joint produced at 1170°C for 4 hours with joint loading.

Table 5 – High temperature tensile properties of TLP bonded CM 247 LC joints at 850°C.

Temperature	Residual Liquid Present	Time (h)	Yield Strength (MPa)	Ultimate Tensile Strength (MPa)	% Elongation
CM 247 LC [14].	-	-	819	830	10.5
1070°C	Yes	0.25	313	313	0
1070°C	Yes	1	468	468	0
1070°C	No	4	321	321	0
1125°C	Yes	0.25	30*	30*	0
1125°C	No	1	567	567	0
1125°C	No	4	512	512	0
1170°C	No	0.25	450	450	0
1170°C	No	1	390	390	0
1170°C	No	4	380	380	0

* Defects in bonded joint resulted in poor properties

In all samples, a brittle joint was observed with poor elongation measured. Necking in the samples was not observed and all joints broke suddenly. While this was expected in joints with residual liquid where brittle eutectic phases form, joints that completed isothermal solidification also exhibited poor properties. The fracture surfaces of tensile specimens revealed particles which were rich in refractory elements and slightly depleted in nickel (Figure 26). An EDS point scan of these particles showed they also contained a significant amount of boron (Figure 27).

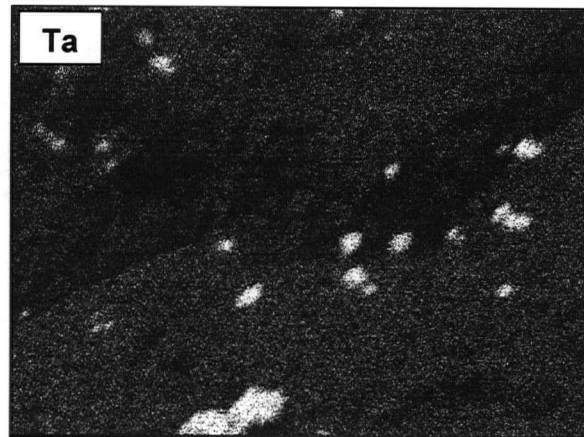
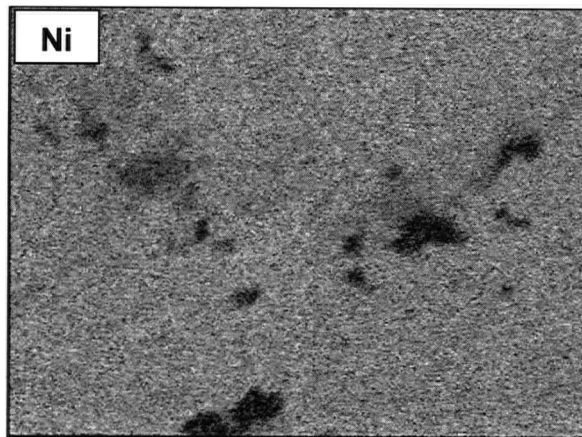
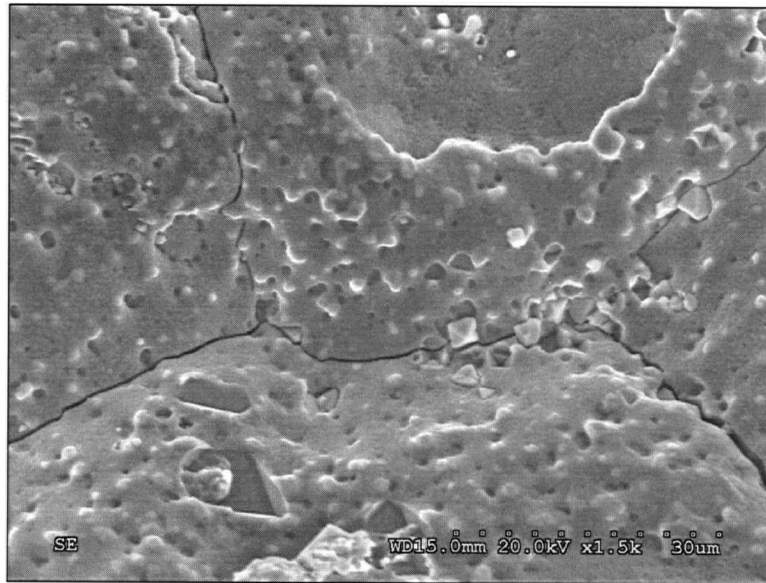


Figure 26 – Fracture surface of a tensile specimen bonded at 1170°C for 4 hours and tested at 850°C.

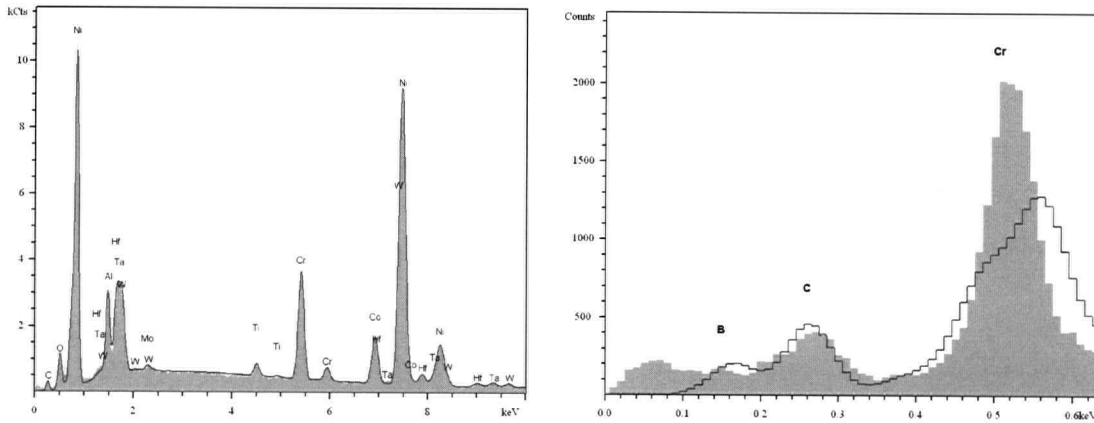
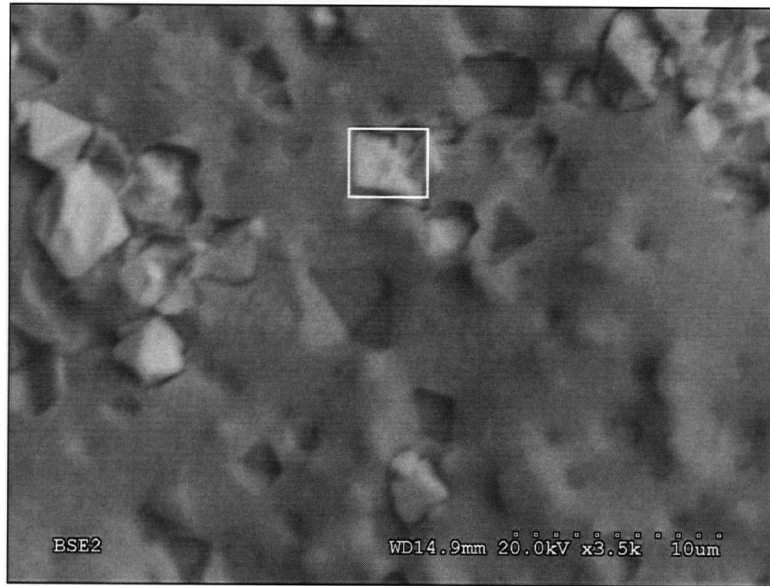


Figure 27 – EDS point scan of precipitates found in the fracture surface of a joint bonded at 1170°C for 4 hours and tested at 850°C.

The brittle centerline eutectic is detrimental to the properties of a joint because it forms a continuous fracture path and results in poor tensile properties. A possible reason for the poor properties in the completed joints is the presence of unwanted precipitation in the precipitation zone and the anomalous precipitation that occurred adjacent to the filler material/substrate interface. These precipitates could potentially reduce the ductility in the joint and result in poor properties. Furthermore, the lack of solid-solution strengthening elements in the filler alloy due to the lack of a proper post bond heat treatment can lead to a weak joint regardless of unwanted precipitation.

In the sample bonded at 1125°C for 15 minutes, the joint exhibited particularly poor properties. It is suspected that bonding defects that arose from contamination of the sample prevented proper bonding of this specimen.

4.3 Hardness Properties

Hardness testing was performed at 6 locations across the joint interface (Figure 28). These locations were chosen to represent (A) The centerline eutectic, (B) isothermally solidified solid-solution hardened phase, (C-D-E) diffusion induced precipitation zone, and (F) base material. Differences in sample widths due to processing are avoided using this selective zone hardness testing method.

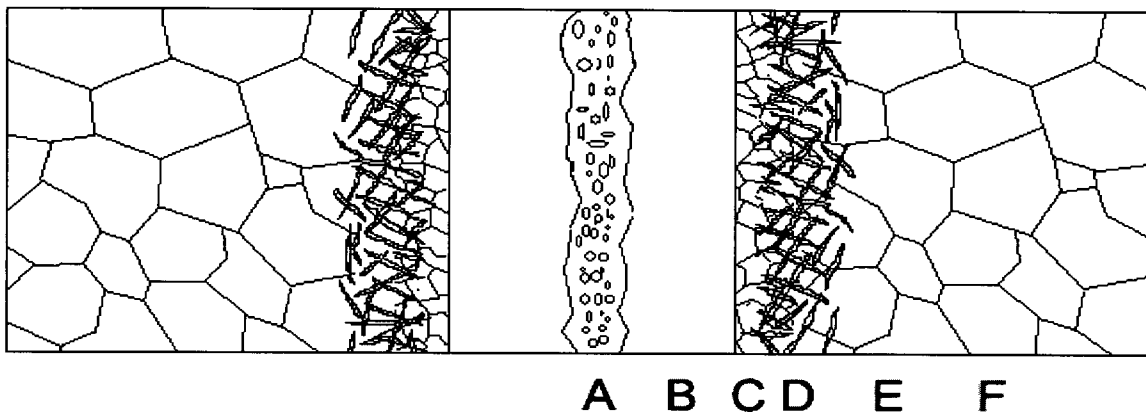


Figure 28 – Schematic diagram of micro-hardness testing locations.

Two sets of samples were examined: microstructural specimens processed without joint loading and samples taken from the ETMT tensile samples which were bonded with a compressive load. Figure 29 and Figure 30 show the hardness data obtained for samples with and without joint loading respectively.

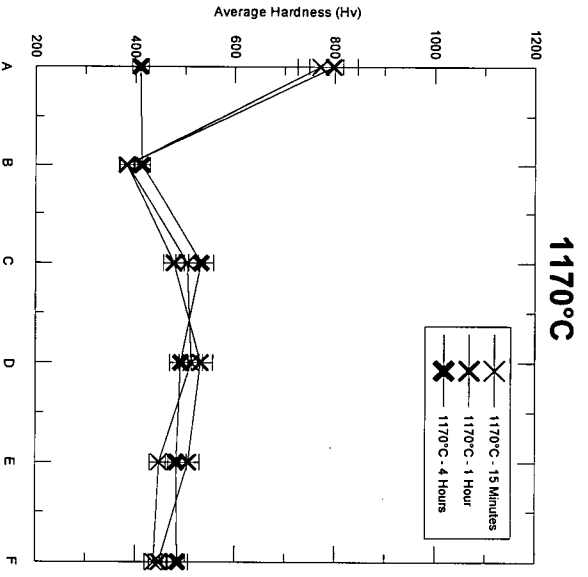
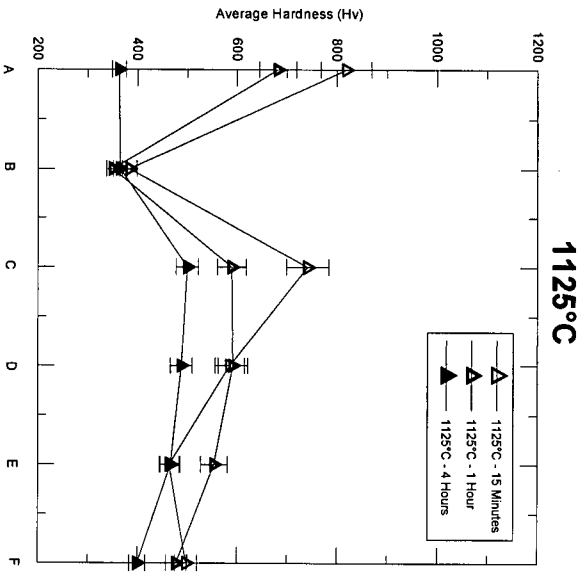
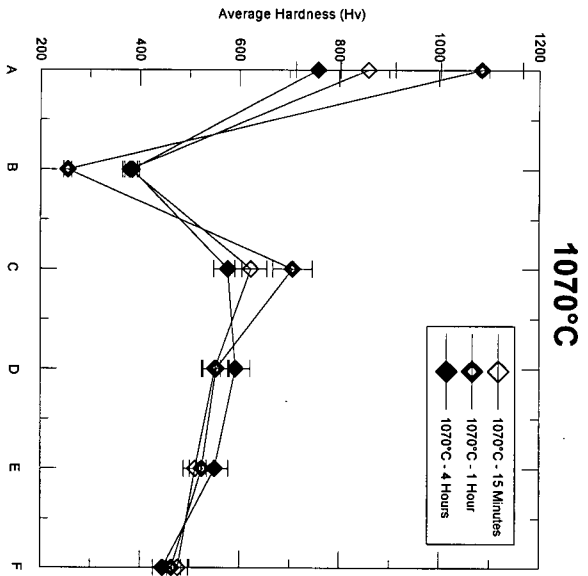


Figure 29 – Hardness data for samples bonded without joint loading.

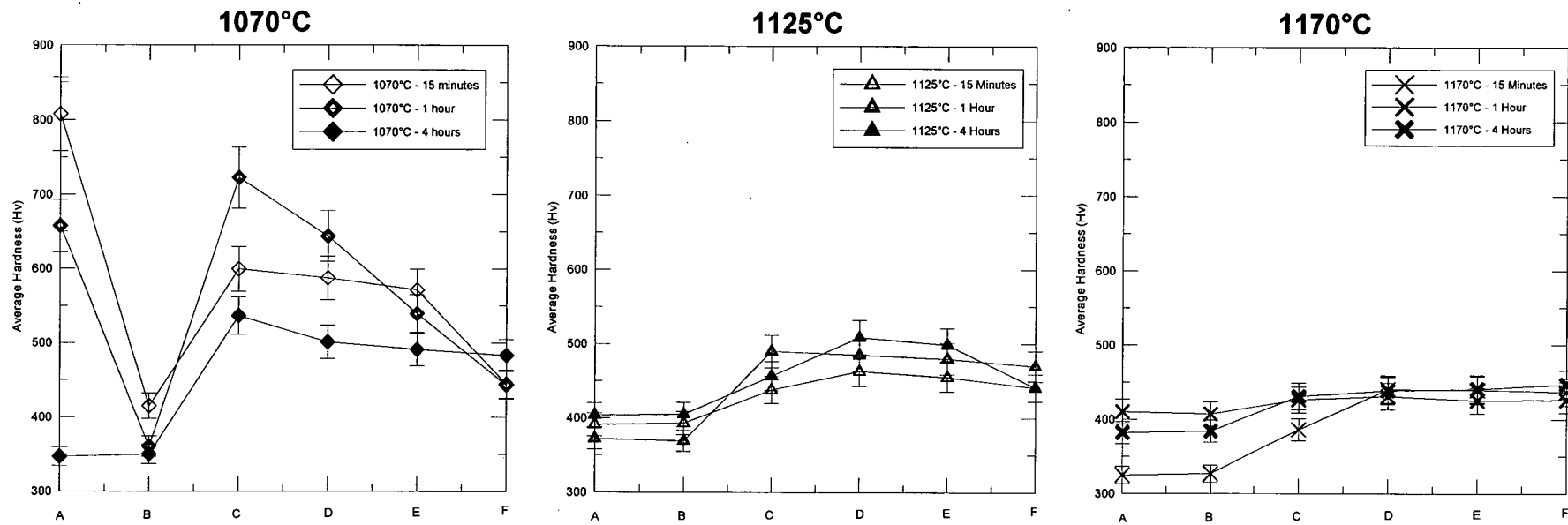


Figure 30 – Hardness data for ETMT tensile samples processed with joint loading.

In samples created without the joint loading, a hard centerline eutectic was found in incompletely isothermal solidified joints with an average micro-hardness of 850 HV0.0025 which is significantly higher than the base material that was found to have a micro-hardness of 450 HV0.0025. The high level of hardness in these phases suggests an embrittling effect which can allow propagation of a crack along its continuous length.

In the isothermal solidified region adjacent to the centerline eutectic was the proeutectic nickel solid-solution which had hardness levels of around 400 HV0.0025. In samples that had completed isothermal solidification, the centerline hardness was equal to the isothermal solidified region, both of which are slightly less than that of the base material. This indicates that the absence of strengthening alloy additions in the filler material results in the need for a longer post-bonding heat treatment. A longer exposure time would permit the diffusion of the desired elements from the base material into the region occupied by the filler, thus improving the properties of the joint.

The region adjacent to the joint was found to be harder than the base material in all cases with hardness levels decreasing with increased holding time and temperature. Average values adjacent to the joint were 600 HV0.0025 indicating that a large amount of brittle precipitates had formed in this region. As observed in this work, short holding times promoted the creation of the precipitates in the precipitation zone and longer holding times resulted in their dissolution due to homogenization.

The difference in thermal expansion between the brazing support and the superalloy substrate resulted in a load being applied during the preparation of the tensile specimen. This load squeezed liquid out of the joint during joining and resulted in liquid widths that were significantly narrower than in samples created without load. Since the gaps were narrower, the completion of isothermal solidification occurs sooner in these joints and less residual eutectic remained. Consequently, the peak hardness was lower in the tensile specimens as compared with that of specimens bonded without loading for an equivalent processing temperature and time (Figure 30). However, the joint loading did not have an

effect on the average hardness of the residual liquid that existed in samples that were incompletely isothermal solidified joints.

4.4 Diffusion of Alloying Elements

Due to the lack of strengthening alloy additions in the braze filler, the diffusion of chemical elements from the base material into the braze joint is vital for producing a high quality joint. An advantage of TLP bonding is that the homogenization of the bond can be performed in the same processing stage as the bonding by protracting the holding time. Selected area EDS analysis was used to map the composition gradient across the TLP bonded interfaces and the affected base material composition.

The analyzed elements were selected due to their role in the strengthening of the superalloy. Al, Ti and Ta are strongly partitioned into the γ' phase from which precipitation hardened superalloys derive their strength. Co and W are important solid solution strengthening additions for the γ phase. Due to the high concentration of Cr in the braze filler, it was also prudent to observe the changes in this element. While measurements were made up to 300 microns away from the center of the joint, only a distance of 150 microns is reported as no significant change was observed beyond this distance. The results of the scans are shown below in Figure 31.

Homogenization of a higher degree was observed in joints that had undergone completed isothermal solidification and in joints processed at higher temperatures and longer times. In specimens having undergone incomplete solidification during the isothermal treatment, steep chemical gradients remained between regions containing residual liquid and the isothermally solidified proeutectic region. Al was the quickest to homogenize in the joints. In the sample held at 1170°C for 4 hours, only a slight gradient was observed between the joint and the base material. The Al atom is among the smallest in the superalloy chemical system and has a relatively high diffusivity. At the higher processing temperature and longer holding times, the emergence of the cuboidal precipitates in the isothermal solidification zone is a product of the diffusion of this

element into the joint. Co atoms were observed to have diffused into the joint nearly as fast as Al atoms despite being larger than the Al atom. The Co concentration despite quickly diffusing into the joint was still deficient in the joint due to the high concentration normally present in the base metal. After 4 hours at 1170°C, the joint contained only 7 at% Co compared to the 11 at% in the base material. Conversely, the concentration of Ta and Ti were relatively low in the substrate but they quickly homogenized in the joint during the same processing time. As the joint was rich in Cr atoms due to the alloying of the filler material, it is interesting to note that the Cr concentration in the joint remained high even after the completion of solidification. The joint was also found to be W deficient and remained so even in samples held for 4 hours at 1170°C. This is expected since the diffusion of W in Ni is amongst the slowest in all the platinum-group metals [70].

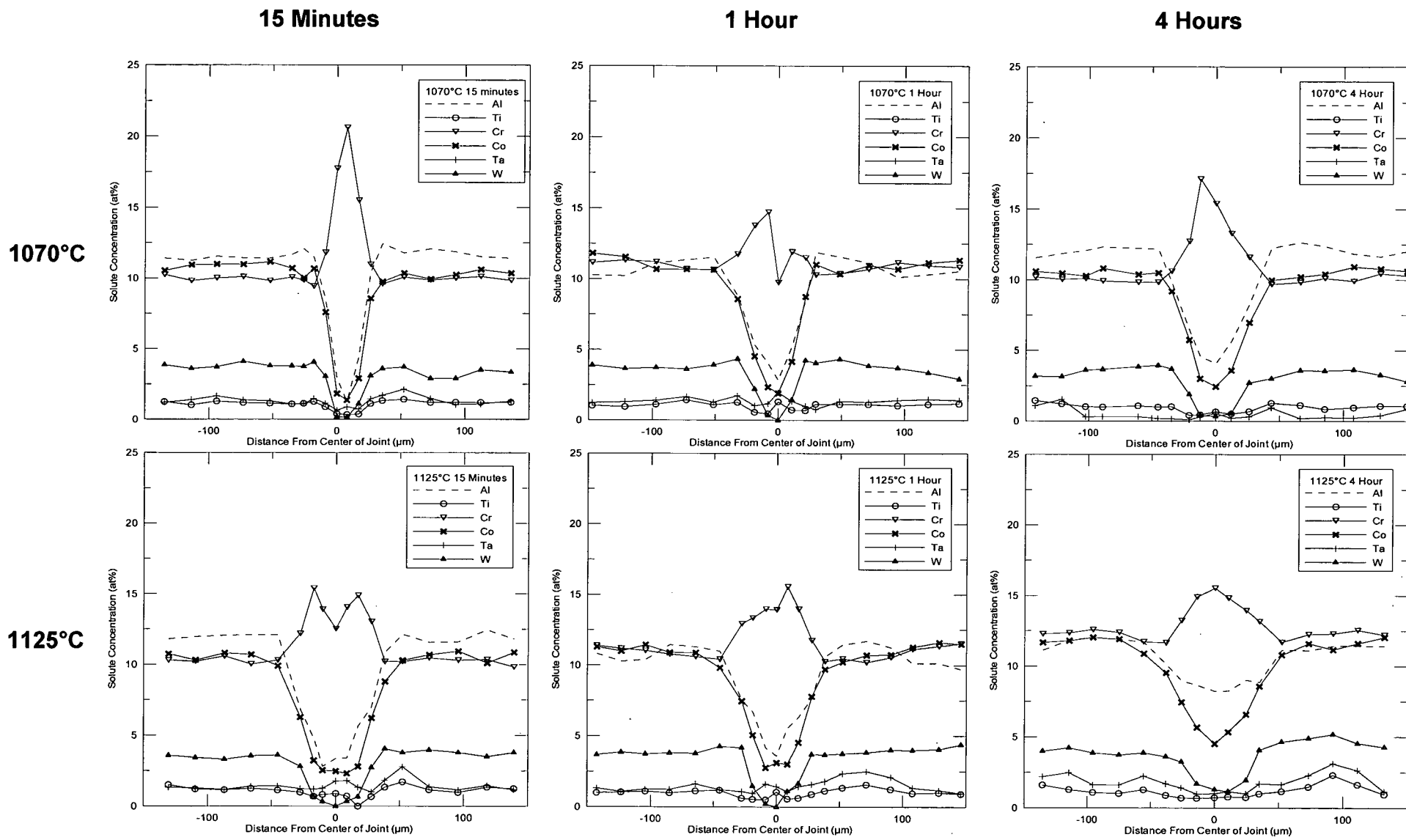
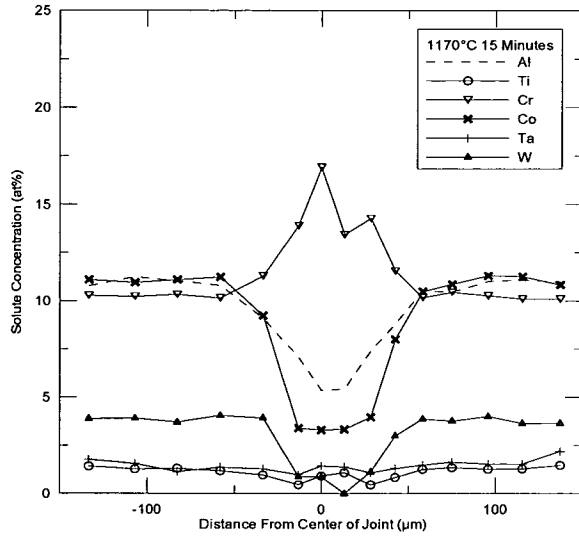


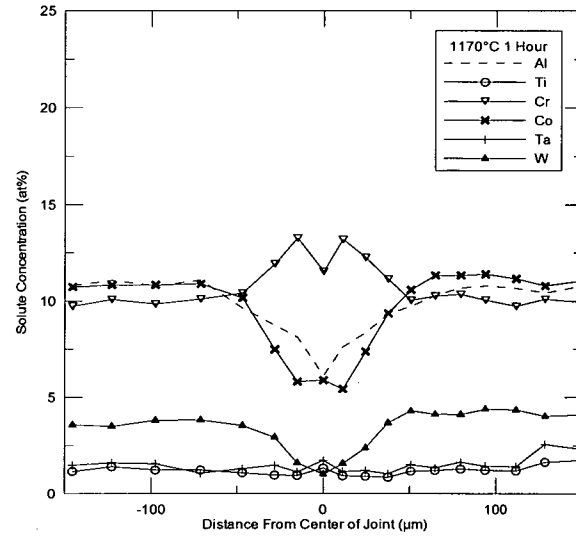
Figure 31 – Element concentration profile of a joint held at various temperatures and times.

1170°C

15 Minutes



1 Hour



4 Hours

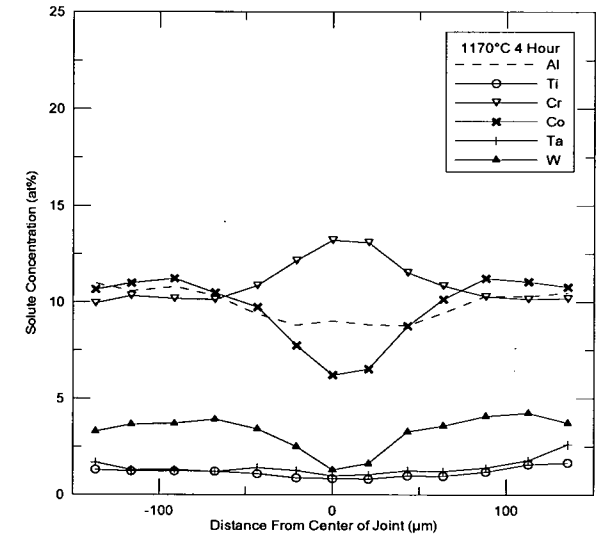


Figure 31 (cont.) – Element concentration profile of a joint held at various temperatures and times.

Chapter 5

Modeling Predictions

One of the advantages of the TLP bonding is the elimination of unwanted eutectic phases. However, as noted in the previous chapter, insufficient processing time leads to incompletely isothermal solidified joints that contain brittle intermetallic structures which can be detrimental to joint strength. Since there are many processing variables such as the bonding time and temperature, process modeling is a useful tool for the prediction of a final joint microstructure. Process models can fall into three categories: analytical, numerical and a combination of analytical and numerical. Analytical models present elegant although inflexible solutions for the bonding process but can provide useful information with fast calculations. Numerical models sacrifice speed for flexibility and the ability to accurately predict the behavior of real systems but are more complicated and slow. In combination models, numerical solutions are used but contain analytical solutions for portions of the calculations providing intermediate speed and accuracy. In this chapter, the various models in the literature are explored.

5.1 Analytical Models for TLP Bonding

Conventional models describe TLP bonding as discrete stages which are modeled separately from each other as: heating, dissolution, widening, isothermal solidification

and homogenization. In general, the models of TLP bonding depend on the diffusion of the MPD within the joint assembly. Accordingly, models are created by drawing on mathematical solutions to Fick's laws of diffusion and depend on the following assumptions [71, 72]:

- The materials compose a binary chemical system.
- A state of local equilibrium exists at the moving interface.
- The moving interface is planar.
- The diffusion coefficients, molar volume and activity coefficient of the solute are independent of composition.
- The molar volumes in different phases are equal.
- There is negligible liquid flow due to convection & stirring in the liquid phase.
- There is no effect of latent heat.
- The substrate is completely wetted by the molten filler material.
- Buildup of solute in the base material is negligible.
- Perfect mixing of solute in the liquid phase.
- The stages occur sequentially

5.1.1 Heat Up

Niemann and Garrett proposed this solution to account for the diffusion that occurs during the heat up of the component from room temperature to the brazing temperature [57]. This was proposed because of the observed loss of the electroplated copper layer during heat up from room temperature when joining B-Al composite materials using the eutectic bonding technique. This problem was found to be significant when a thin Cu interlayer was used to produce a liquid in the Al substrate because the interlayer could be consumed during the heat up stage before a liquid was formed. In Niemann and Garrett's solution to this problem:

$$x\rho_L = 1.1284\rho_S (C_i^{SL} - C_i^{\infty,S})(D^S t)^{1/2} \quad (6)$$

where x is the thickness of the copper interlayer lost through diffusion, D^S is the diffusion coefficient of copper in aluminum, t is time, C_i^{SL} is the solubility of copper in aluminum, $C_i^{\infty,S}$ is the initial copper concentration in the aluminum substrate, ρ_L is the density of copper and ρ_S is the density of the alloy. However, this was formulated using constant diffusion coefficients and solubilities, both of which are a function of temperature and cannot remain constant during the heating [5]. To account for this, MacDonald and Eager suggested that an effective diffusion coefficient be calculated as proposed by Shewmon [29]. Shewmon showed that the contributing diffusive flux occurred above 80% of the bonding temperature. Assuming the Arrhenius form of the diffusion coefficient, the solution takes the form of a slowly converging series function:

$$D_{eff} = \frac{D_o}{\dot{T}} \left[\frac{\exp\left(-\frac{Q}{RT}\right)}{T} \right] - \frac{Q}{R} \left[\ln\left(\frac{1}{T}\right) - \left(\frac{Q}{RT}\right) + \frac{1}{2 \cdot 2!} \left(\frac{Q}{RT}\right)^2 - \frac{1}{3 \cdot 3!} \left(\frac{Q}{RT}\right)^3 + \dots \right] \Bigg|_{0.8T_b}^{T_b} \quad (7)$$

where \dot{T} is the heating rate. It should be noted that this model does not take into account the change in solubility that would also occur during heating.

5.1.2 Liquid Dissolution

The dissolution of the liquid interlayer can be divided into two stages. Stage 1 occurs from the melting temperature of the interlayer to the brazing temperature of the joint. This requires the assumption of local equilibrium at the solid/liquid interface which changes with temperature as the temperature is ramped to the brazing temperature. Stage 2 occurs at the brazing temperature when the interlayer is undergoing isothermal dissolution. At the end of this stage, the liquid width reaches a maximum. While there have been no analytical solutions developed to model stage 1 dissolution, a considerable amount of work has been performed on stage 2 dissolution. MacDonald and

Eager [29] reported that dissolution occurs first at the interlayer-base material interface forming a liquid and expands in both directions to consume the interlayer and partially dissolve the base material (Figure 32). At the end of stage 2 dissolution, the interlayer is fully liquid.

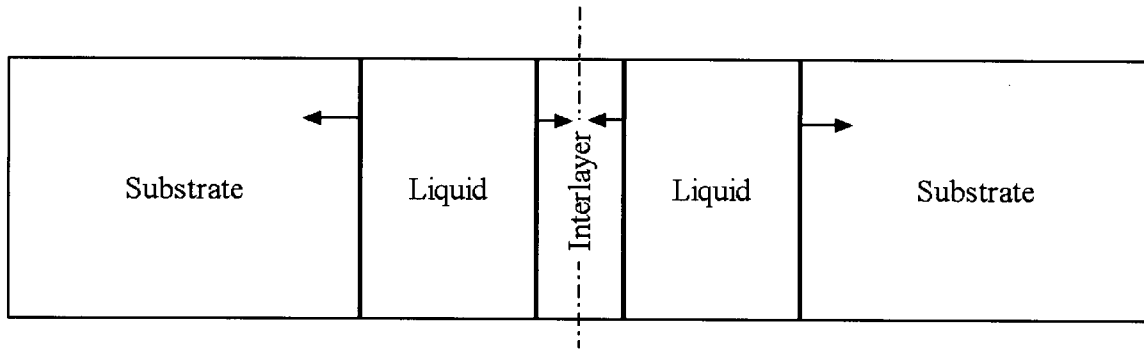


Figure 32 – Schematic of the interlayer dissolution mechanism.

Liu outlines a dissolution model that accounts for the dissolution front proceeding into the interlayer as well as into the base material. This model utilizes Fick's 2nd law subject to the following assumptions [29]:

- Uni-dimensional diffusion
- The liquid is static with no convection effect
- Constant diffusion coefficients
- Local equilibrium exists at the solid-liquid interface
- The base material is a semi-infinite domain
- The solid/liquid interfacial area remains constant

The liquid/base material and liquid/interlayer interfaces are assigned dimensionless growth constants K^{α} and K^{β} respectively. As the motion of both of these interfaces are linked, the growth constants need to be solved simultaneously by solving the two explicit functions derived for each interface:

$$\frac{C_i^{\infty,\beta} - C_i^{LS,\beta}}{C_i^{LS,\alpha} - C_i^{\infty,\alpha}} K^\beta \exp(K^{\beta^2} - K^{\alpha^2}) - K^\alpha = 0 \quad (8)$$

$$\frac{C_i^{\infty,\alpha} - C_i^{LS,\alpha}}{C_i^{LS,\alpha} - C_i^{\beta,\infty}} K^\alpha \sqrt{\pi} [\operatorname{erf}(K^\beta) - \operatorname{erf}(K^\alpha)] - \exp(-K^{\alpha^2}) = 0 \quad (9)$$

The time for dissolution of the braze interlayer of initial thickness $2h$ at a given temperature can be calculated from the following equation which is a function of the diffusion of the MPD in the liquid phase, D^L :

$$t_d = \frac{(2h)^2}{16K^{\beta^2} D^L} \quad (10)$$

The width of the liquid interlayer at the completion of stage 2 dissolution is:

$$W_L = 2h + 2K^\alpha \sqrt{D^L t_d} \quad (11)$$

These equations were re-derived in the present work and can be found in Appendix A.

5.1.3 Widening

Widening is the continued dissolution of the base material from the time after the interlayer is fully liquid until the liquid composition is reduced to the liquidus composition as defined by the equilibrium phase diagram. The widening problem was solved similarly by Ramirez & Liu by considering one interface rather than two [72]. Assuming that the diffusion of boron in the liquid is the limiting mechanism, the time of widening and homogenization can then be calculated with the following equation:

$$t_h = \frac{Z^2}{16K^2 \tilde{D}^L} \quad (12)$$

where K is a dimensionless parameter that can be calculated from the following equation [72, 73]:

$$K = \frac{1}{\sqrt{\pi}} \left[\left(\frac{C_i^{LS} - C_i^{\infty,L}}{C_i^{LS} - C_i^{SL}} \right) \frac{\exp(-K^2)}{\operatorname{erfc}(K)} - \sqrt{\frac{\tilde{D}^S}{\tilde{D}^L}} \left(\frac{C_i^{SL} - C_i^{\infty,S}}{C_i^{LS} - C_i^{SL}} \right) \frac{\exp\left(-K^2 \frac{\tilde{D}^L}{\tilde{D}^S}\right)}{\operatorname{erfc}\left(K \sqrt{\frac{\tilde{D}^L}{\tilde{D}^S}}\right)} \right] \quad (13)$$

The interface displacement, Z is calculated from the following equation:

$$Z = \left(\frac{W_m - 2h}{2} \right) \quad (14)$$

The theoretical maximum width of the liquid, W_m , is a function of the initial concentration, $C^{\infty,L}$, of the MPD in the interlayer of thickness, h , and the equilibrium liquidus composition, C^{LS} , at the processing temperature [72]:

$$W_m = 2h \frac{\rho_S}{\rho_L} \frac{C^{\infty,L}}{C^{LS}} \quad (15)$$

However, this equation does not consider the solute concentration in the base material and assumes that there is a negligible amount present. These equations were re-derived in the present work and can be found in Appendix B.

The use of an error function solution is considered a poor assumption for this stage because it is only applicable for a semi-infinite couple which is not satisfied in the thin liquid region [5]. It is also suggested that base material dissolution depends on a non-parabolic relationship and thus no single rate constant should be able to characterize the

motion [74]. Zhou et al. noted that numerical techniques have been more successful for modeling this stage of the bonding process than analytical solutions [5].

5.1.4 Isothermal Solidification

During this stage, MPD diffuses from the liquid resulting in the solidification of the joint. As this stage is the most time consuming, a number of models have been devised to determine the processing time required for the completion of this stage. Two of the more popular analytical models were devised by Ramirez et al. [72] and Gale et al. [47].

In the model presented by Ramirez et al., the diffusion controlled moving-interface problem is solved similarly to the previous dissolution and widening stages. The solute distribution in the liquid is considered uniform and therefore solute diffusion in the liquid can be ignored. In addition, the solid portion can be considered semi-infinite allowing for the use of error function solutions. The solution for the dimensionless growth constant can be solved from [72, 73]:

$$K = \frac{1}{\sqrt{\pi}} \left[\left(\frac{C_i^{SL} - C_i^{\infty,S}}{C_i^{LS} - C_i^{SL}} \right) \frac{\exp(-K^2)}{\operatorname{erfc}(K)} \right] \quad (16)$$

where C_i^{SL} and C_i^{LS} are the equilibrium solidus and liquidus concentrations as defined by the equilibrium tie lines at the bonding temperature. $C_i^{\infty,S}$ is the MPD concentration present in the substrate material. Solving the equation numerically, we can thus determine the time of solidification from the following equation which is a function of the diffusion of the MPD in the solid phase, D^S :

$$t_s = \frac{W_m^2}{16K^2 \tilde{D}^S} \quad (17)$$

These equations were re-derived in the present work and can be found in Appendix C.

Gale et al. successfully applied an alternative model [47] to the isothermal solidification stage. In their model of this stage, the assembly was treated as the diffusion of solute from a finite interlayer into a semi-infinite solid substrate. By utilizing Crank's solution of Fick's second law of diffusion [75], the concentration of a solute at a distance x from the center of the joint at a time t is calculated from the following equation:

$$C(x,t) = C^{\infty,S} + \frac{1}{2}(C^{\infty,L} - C^{\infty,S}) \left(\operatorname{erf} \left[\frac{h-x}{2\sqrt{D^S t}} \right] - \operatorname{erf} \left[\frac{h+x}{2\sqrt{D^S t}} \right] \right) \quad (18)$$

The completion of isothermal solidification can be determined by calculating the time when the composition of the center of the joint, $C(0,t_s)$, equals the solidus composition, C^{SL} . Substituting $x = 0$ and $C(0,t_s) = C^{SL}$ into the above equation we get:

$$C^{SL} - C^{\infty,S} = (C^{\infty,L} - C^{\infty,S}) \left(\operatorname{erf} \left[\frac{h}{2\sqrt{D^S t_s}} \right] \right) \quad (19)$$

5.1.5 Homogenization

The homogenization of cast alloys has been well studied separate from the TLP bonding process for which there are many suitable models. In general, Fick's law is used to determine the diffusion of solute away from the centerline where the concentration would be a maximum.

$$C = C^{\infty,S} + (C^0 - C^{\infty,S}) \operatorname{erf} \left[\frac{h}{2\sqrt{D^S t}} \right] \quad (20)$$

where C^o is the initial peak concentration of solute in the joint where $C^o = C^{SL}$ at the beginning of homogenization for a joint immediately following the completion of isothermal solidification.

5.2 Predictions from the Analytical Models

As mentioned in the previous chapter, of the various stages of the TLP bonding process, the isothermal solidification time and the maximum dissolution width hold the most practical importance. The error associated with ignoring the dissolution time is estimated to be approximately 30 seconds [47] which is insignificant when the time required for TLP bonding is measured in the order of hours. In this chapter, the models presented above were used to determine the predicted isothermal solidification times and dissolution widths. However, as the modeling predictions are sensitive to the data sources available, a critical assessment of the modeling parameters is essential. For the modeling of the TLP bonding process in CM 247 LC, data on the thermodynamic equilibrium of the nickel-boron chemical system and diffusivity of boron (MPD) in the superalloy substrate is required.

5.2.1 Thermodynamic Data of the Ni-B System

For the present work, equilibrium constants for the solubility of boron in nickel were obtained from several sources. Equilibrium constants were calculated by using the thermodynamic calculator Thermo-Calc[‡]. Two sets of equilibrium constants were provided by using the Kaufman Binary Alloys Database and the Rolls-Royce plc (London, U.K.) / Thermotech (Guilford, U.K.) Ni-DATA Superalloys Database. The Kaufman Binary Alloy Database was produced by Larry Kaufman of Man Labs Inc. (Boston, USA). The database was derived from data originally published in a series of articles in the Calphad journal which cover binary systems of Fe, Cr, Ni, B, C, Co, Mo, Nb, Ti, W, Mn, Al, Si and Cu [76]. The Rolls-Royce plc / Thermotech Ni-DATA database was obtained by measurement of thermodynamic properties directly from nickel-base superalloys and contains information on the Ni-Al-Co-Cr-Hf-Mo-Nb-Ta-Ti-

[‡] Thermo-Calc is a registered trademark of the Royal Institute, Stockholm, Sweden.

W-Zr-B-C system [77]. The ASM binary Ni-B phase diagram was also used to obtain a third set of equilibrium constants [46, 47].

Binary phase diagram tie-lines can be referenced to determine the equilibrium compositions established during isothermal solidification. However, the phase diagrams from these sources differ from each other. The eutectic temperature, solidus and liquidus lines all vary from one source to another. Furthermore, some phases are missing from the thermodynamic databases. Figure 33 shows the Ni-B phase diagram generated by Thermo-Calc using the Ni-DATA superalloy thermodynamic database in comparison to the ASM phase diagram. Since these diagrams vary, the equilibrium compositions will differ from each other as shown in Table 6.

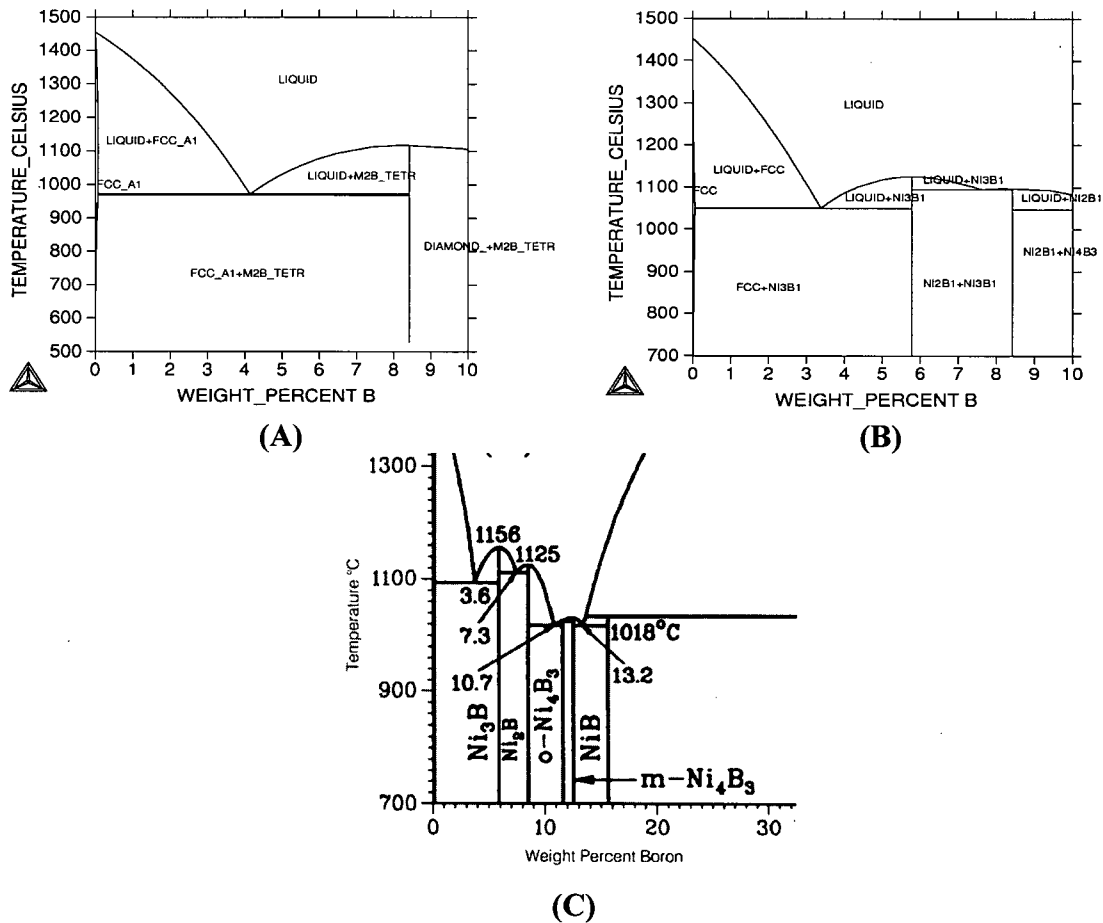


Figure 33 – Nickel-Boron phase diagrams generated using Thermo-Calc and (A) Ni-DATA Super alloys Database [77] (B) Kaufman Binary Alloy Database [76] (C) Nickel-Boron phase diagram [46].

Table 6 – Equilibrium compositions obtained from the Ni-DATA Superalloy Database, Kaufman Binary Alloy Database and ASM Phase Diagram in atomic fraction.

Temperature	Ni-DATA Superalloys Database		Kaufman Binary Alloy Database		ASM Phase Diagram	
	Solidus	Liquidus	Solidus	Liquidus	Solidus	Liquidus
1070°C	0.003	0.168	0.0028	0.1546	0.003	0.181
1125°C	0.003	0.153	0.0021	0.1391	0.003	0.165
1170°C	0.003	0.138	0.0017	0.1254	0.003	0.152

5.2.2 Diffusion Coefficient of Boron in Nickel

In general, when non-composition dependent diffusion coefficients are considered, the diffusivity can be calculated from the Arrhenius expression:

$$\tilde{D} = \tilde{D}_o \exp\left(\frac{-Q}{RT}\right) \quad (21)$$

Where Q is the activation energy for the diffusion jump in J/mol, R is the universal gas constant and T is the temperature. Thus the diffusion coefficient is temperature dependent.

Data on the diffusivity of boron in nickel is scarce in the literature. Only a handful of studies have been conducted in recent years partly because of the difficulty in detecting boron atoms (Table 7).

Table 7 – Diffusion coefficients for boron in nickel at 1170°C.

Source	D_o m ² /s	Q J/mol	D^s m ² /s
Wang [78]	6.60E-07	9.62E+04	2.170E-10
Nakao [34]	1.44E-01	2.26E+05	9.510E-11
Ramirez [72]	3.27E-04	1.66E+05	3.179E-10
Liping *	2.30E-07	7.95E+04	3.050E-10
Chu †	1.10E-06	9.99E+04	2.664E-10

* As cited by Ramirez & Liu [72]

† As cited by Campbell & Boettinger [56]

Wang [78] and Chu[§] measured the diffusivity of boron in nickel by performing particle tracking autoradiography experiments. Ramirez [72] and Nakao [34] observed similar results by measuring the rate of isothermal solidification during TLP bonding experiments with nickel-boron binary alloys.

Nakao showed that the apparent diffusion coefficients of boron in superalloys can also be calculated by measuring the residual liquid widths of incomplete isothermal solidified joints created from conventional braze filler materials and superalloys [34]. When plotted on a graph of the residual liquid width vs. the square root of time, the slope of each isotherm, m , is related to the activation energy of diffusion, Q , by the analytical solution of isothermal solidification:

$$\ln(m) = \ln \left[\frac{4C^{SL} / (V_s p^{1/2})}{C^{LS} / V_l - C^{SL} / V_s} \right] + 1/2 \ln(D_o) - \frac{Q}{2RT} \quad (22)$$

where C^{SL} and C^{LS} are the equilibrium concentration ratios of the melting point depressant and V_l and V_s are the molar volumes of the liquid and solid phases respectively. In real multi-component systems it is not possible to determine equilibrium concentrations of C^{SL} or C^{LS} . Instead, the first two terms are combined into a constant A . Thus the activation energy of diffusion is related to the isothermal solidification rate at a given temperature by a linear relation.

$$\ln(m) = A - \frac{Q}{2RT} \quad (23)$$

In the present work, the residual eutectic liquid width was measured at the end of each holding time by examining polished and etched transverse cross-sections of joints with an SEM. The experimentally measured average eutectic width was plotted against the

[§] As cited by Campbell & Boettinger [56]

square root of time as shown in Figure 34. Figure 35 shows the linear relation between $\ln(m)$ and $1/T$ for the above data.

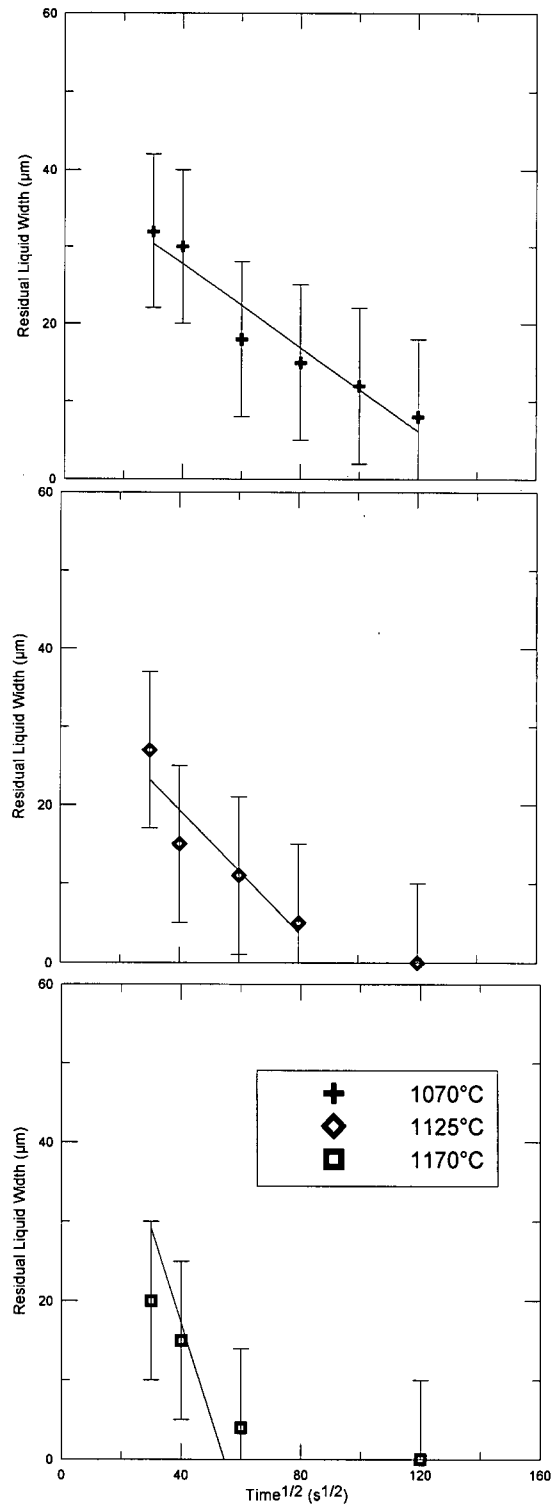


Figure 34 – Residual liquid measurement of samples processed at 1070°C, 1125°C and 1170°C.

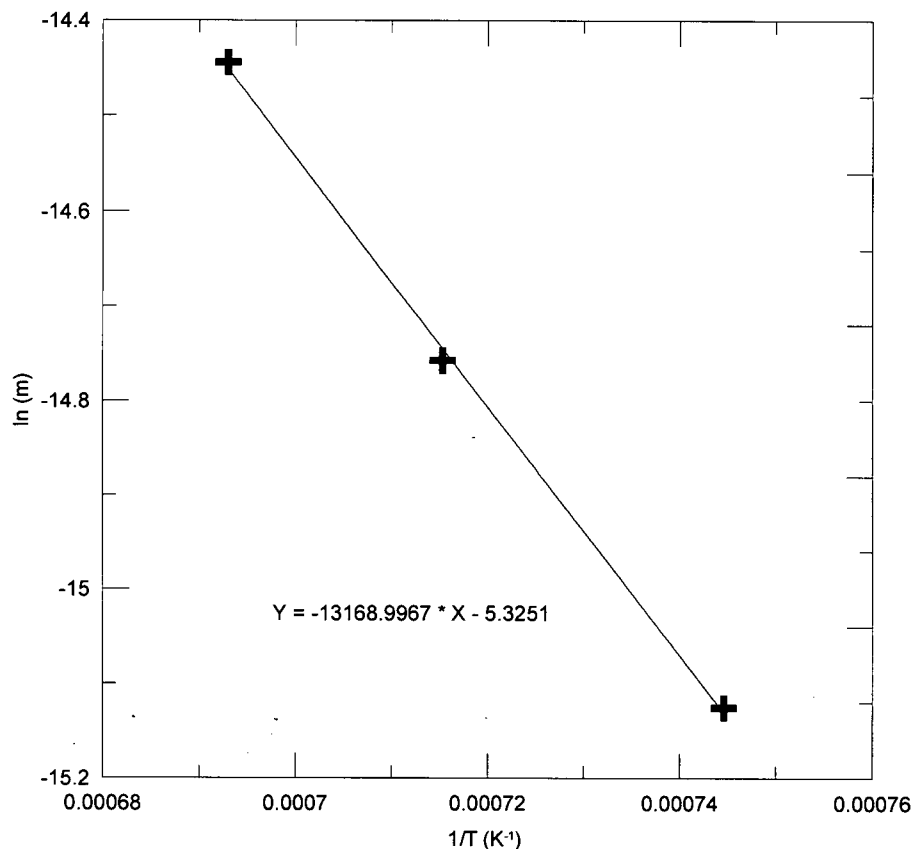


Figure 35 – The linear relationship between $\ln (m)$ and $1/T$ used to measure the apparent diffusion coefficient from TLP bonding experiments in CM 247 LC specimens.

The apparent activation energy of diffusion for boron in CM 247 LC was found to be 219 kJ/mol. The activation energy for CM 247 LC is similar to values found in the literature for boron diffusion in other superalloy measured by Nakao et al. [79]. The apparent diffusivities had activation energies in the range 199-219 kJ/mol for polycrystalline superalloys and 266 kJ/mol for single crystal CMSX-2. Ojo performed similar work on the diffusivity of boron in IN 738 LC with close correlation to values measured by Nakao et al. for polycrystalline superalloys.

Ojo cited a frequency factor, $D_o = 0.14 \text{ m}^2/\text{s}$, calculated by Nakao et al. [63]. However, Ojo found that a frequency factor of $D_o = 0.014 \text{ m}^2/\text{s}$ was more appropriate. This value was determined by first back calculating the diffusion coefficient of boron in the substrate at each temperature by using the isothermal solidification model outlined by

Gale et al. [47] in equation (19). The extrapolated time to completion of the isothermal solidification as measured from the plots of residual liquid width vs. the square root of time was used for this purpose. These diffusion coefficients and their respective activation energies were then used to determine a common value for D_o [63]. Using this technique, it was found that a D_o value of $0.0163 \text{ m}^2/\text{s}$ was appropriate for the present system. The diffusion coefficient calculated in the present work resulted in a value similar to those of other polycrystalline superalloys reported in the literature (Table 8). It should be noted that CMSX-2 has a diffusion coefficient about two orders of magnitude lower as compared with the other materials listed in the table. This is due to the absence of grain boundaries in CMSX-2 which is a single crystal superalloy.

Table 8 – Apparent diffusion coefficients for boron in nickel-base superalloys at 1170°C.

Source	Alloy	D_o m^2/s	Q J/mol	D^s m^2/s
Present Work	CM 247 LC	0.0163	2.19E+05	1.93E-10
Ojo [63]	IN-738 LC	0.0144	2.18E+05	1.85E-10
Nakao [79]	IN-713	0.144	2.11E+05	3.32E-09
Nakao [79]	IN-600	0.144	2.09E+05	3.92E-09
Nakao [79]	MAR M-247	0.144	1.99E+05	9.03E-09
Nakao [79]	MM 007	0.144	2.19E+05	1.70E-09
Nakao [79]	CMSX-2	0.144	2.66E+05	3.39E-11

5.2.3 Analytical Model Predictions

In comparison to other stages, the isothermal solidification stage is the most significant when determining the processing time as this occurs over several hours whereas other stages take a matter of seconds (with the exception of the post-bond heat treatment). The heat up stage is generally disregarded because it refers to the loss of the MPD in the interlayer through diffusion of solutes during slow heating of the assembly and can be overcome with faster heating rates. However, the dissolution stage is important due to its effects on the final liquid width. A large final liquid width is unwanted as it results in longer isothermal solidification times. Using the analytical dissolution model described earlier, it can be shown that accompanying an increase in temperature is an increase in

maximum joint width due to the lower solubility of boron at higher temperatures in the nickel-boron system (Figure 36). Furthermore, larger interlayer thicknesses also contribute to an increase in the liquid width due to the larger volume of solute contained in the interlayer. To illustrate these points, the final width of joints processed at different temperatures and initial gap widths were calculated for a filler material and substrate of constant composition and shown in Figure 36.

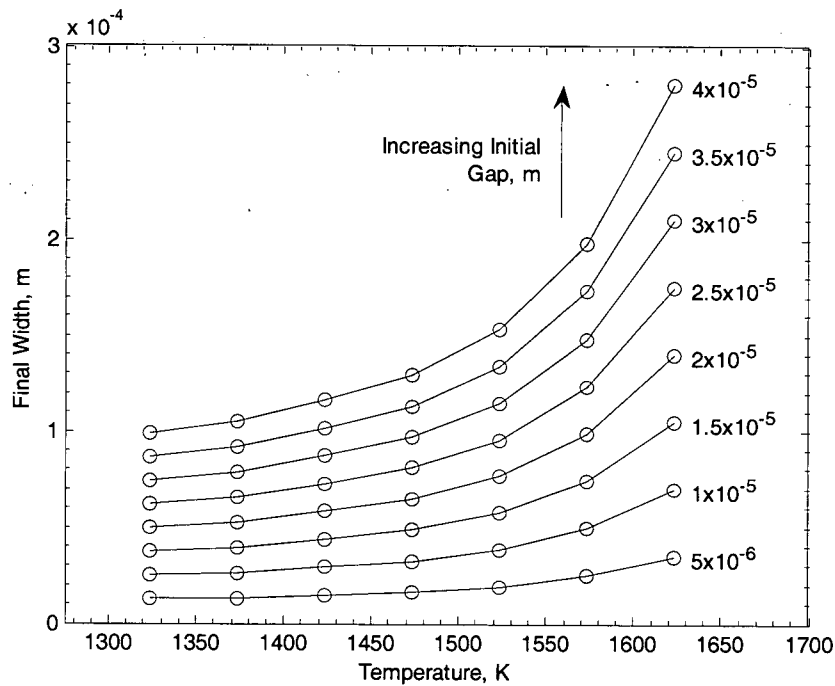


Figure 36 – Increase in liquid width with varying isothermal holding temperature and initial gap widths.

The dimensionless rate constant, K , responsible for the rate of solidification is a function of the saturation of the substrate. The saturation of the substrate is the amount of MPD that is nominally present in the substrate against the amount of MPD that is soluble in the solid phase. A larger solubility of the MPD in the substrate results in a shorter solidification time. The saturation in the substrate is defined as:

$$\text{Substrate Saturation} = \frac{C^{\infty,S}}{C^{SL}} \quad (24)$$

The nominal concentration of MPD in the interlayer is also of importance as supersaturation of the liquid results in widening of the gap. Supersaturation of the liquid occurs when the concentration of MPD in the liquid is above the liquidus composition. While this is unavoidable because one needs a sufficient concentration of MPD to depress the melting point of the filler material below the processing temperature, excessive amounts of MPD can lead to unnecessary widening and in-turn prolong the required processing time. The degree of liquid supersaturation can be determined by:

$$\text{Liquid Supersaturation} = \frac{C^{\infty,L} - C^{LS}}{C^{LS}} \quad (25)$$

Thus, higher solubilities of the MPD in the substrate and lower initial solute concentrations in the substrate and filler material promote a faster rate of isothermal solidification. This is seen in Figure 37 by the shorter bonding time for cases with lower substrate saturations. Increasing liquid supersaturations will result in longer bonding times due to the increase in substrate dissolution and increased widening of the gap.

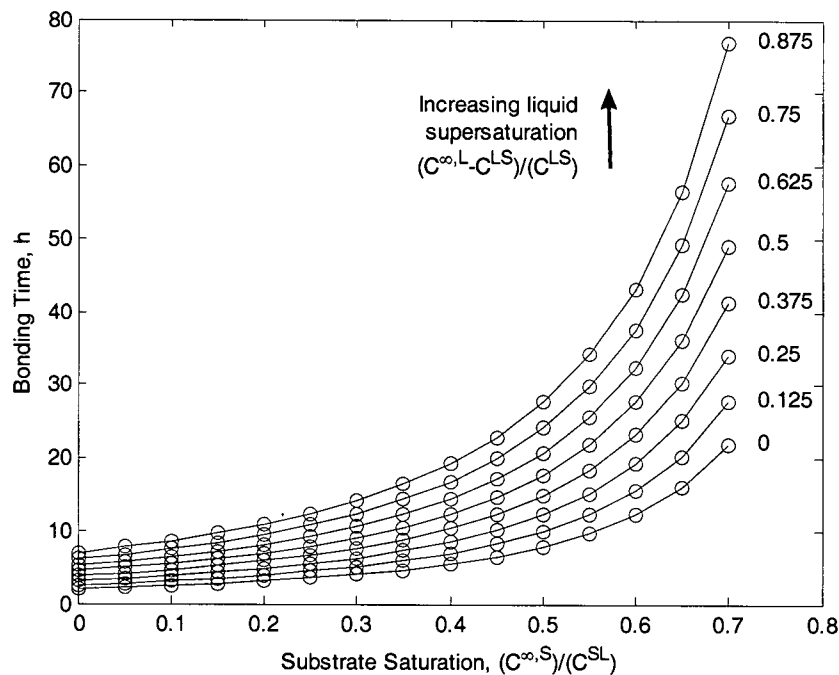


Figure 37 – Effect of saturation of MPD in the substrate and supersaturation in the liquid filler metal on solidification time.

In addition, for a given composition, the supersaturation of the liquid will decrease with temperature due to the decrease in the liquidus composition at elevated temperatures. This results in a higher solidification rate constant at elevated temperatures which aids the higher diffusion rate to produce a higher solidification rate (Figure 38).

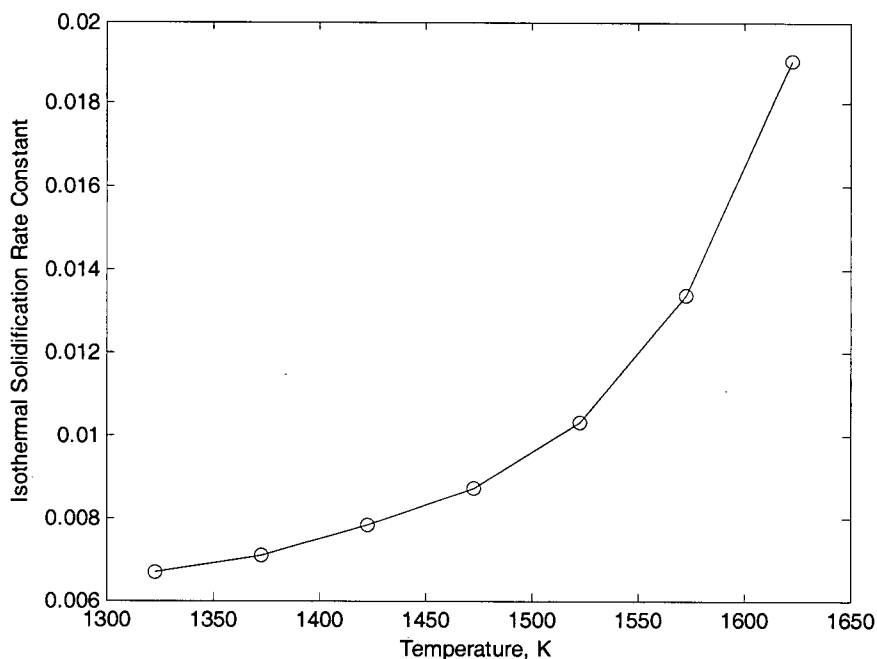


Figure 38 – Change in the dimensionless solidification rate constant with temperature.

The advantage of increasing the temperature to increase solidification rate can be nullified by the dissolution of the base material. At higher temperatures the maximum liquid width increases due to the equilibrium conditions, which results in only marginally faster processing times. Also, the increased economic cost of heating assemblies to the higher temperature along with the possibility of damaging the microstructure of the base material discourages very high processing temperatures. Figure 39 shows the variation of the total processing time due to the increase in temperature.

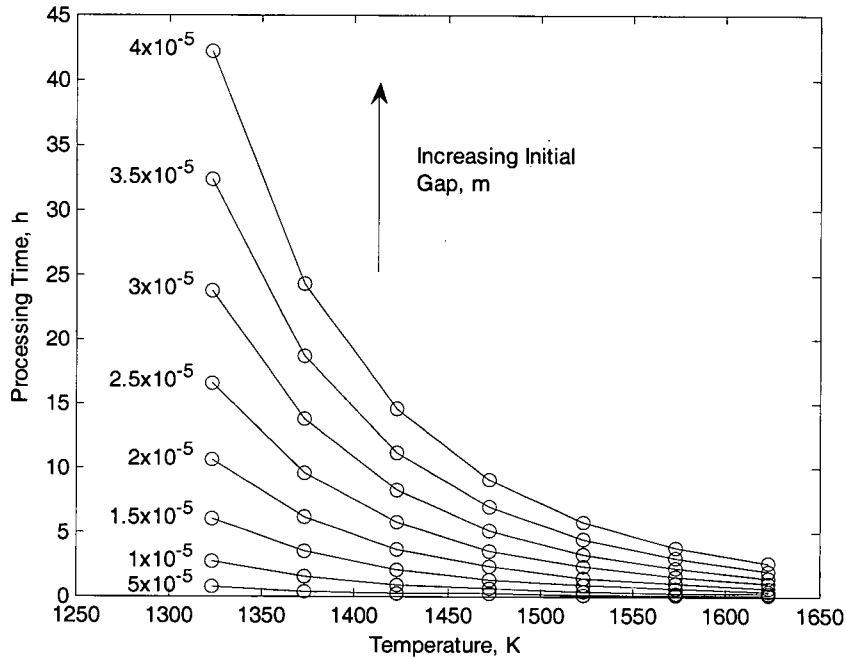


Figure 39 – Required processing time with initial gap sizes at varying temperatures.

Simulations of the bonds created in the experimental regime of this work were performed using the isothermal solidification models outlined by Ramirez et al. and Gale et al. A gap size of 40 microns was assumed for all bonds. The boron concentration of the filler and substrate materials were assumed to be 18.1 at% and 0.078 at% boron respectively which correspond to the concentrations of the MBF-80 filler material and CM 247 LC superalloy. The equilibrium compositions were taken from each of the three data sources listed in Table 6.

The predictions made in the present work based on the binary Ni-B system were compared with the results obtained experimentally in the present work on TLP bonding of CM 247 LC. Table 9 presents a comparison of two sets of data. The width was calculated according to equation (15) with the assumption of a constant density in both the liquid and the solid phases and no loss of solute to the base metal.

Table 9 – Predicted dissolution width using the analytical model vs. average experimentally observed widths (microns).

Temperature	Analytical			Experimental (+/- 2.5)
	Ni-DATA	Kaufman	ASM	
1070°C	42.86	46.57	40.09	47.5
1125°C	47.06	51.76	43.77	62.5
1170°C	52.17	57.42	47.32	67.5

Predictions from the Kaufman database were the closest to the experimental data. However, in all cases this equation underestimated the diffusion width observed experimentally. The deviation may be a consequence of the multi-component alloy used in the experimental investigation. In multi-component systems, the difference in diffusion rates of the alloying elements causes the local equilibrium to constantly change during bonding as noted by Sinclair [80]. The equation used in the above calculation cannot take this effect into account. Furthermore, the assumption of constant density between the liquid and solid phases is not realistic and is possibly another source of error.

The dimensionless solidification constants, K , for the various sources of data used in this work is shown below in Table 10. These values were then used to determine the isothermal solidification time using the model presented by Ramierz & Liu. Isothermal solidification time was also calculated using the model presented by Gale. Using the experimentally measured diffusion coefficient for the diffusion of boron in the nickel-base superalloy CM 247 LC and the predicted dissolution width, the predicted solidification times were calculated and compared to values extrapolated from experimentally observed data in Table 11.

Table 10 – Dimensionless solidification rate constants, K , calculated using the analytical model outlined by Ramirez et al. for equilibrium compositions defined by various sources at 1070°C, 1125°C and 1170°C.

Temperature	Ni-DATA Superalloys Database	Kaufman Binary Alloy Database	ASM Phase Diagram
1070°C	0.7657E-2	0.7572E-2	0.7093E-2
1125°C	0.8430E-2	0.5470E-2	0.7800E-2
1170°C	0.9376E-2	0.4216E-2	0.8487E-2

Table 11 – The predicted solidification time using analytical models proposed by Ramirez et al. and Gale et al. vs. experimentally observed times (hours).

Temperature	Ramirez Model			Gale Model			Experimentally Extrapolated
	Ni-DATA	Kaufman	ASM	Ni-DATA	Kaufman	ASM	
1070°C	11.12	13.4	11.16	4.70	5.68	4.71	5.66
1125°C	5.12	14.68	5.12	2.17	6.14	2.17	2.23
1170°C	2.82	16.88	2.84	1.21	7.01	1.21	1.27

Using equilibrium composition data from the Ni-DATA database and the Ni-B ASM binary phase diagram, the predicted isothermal solidification times predicted by the model proposed by Gale et al. were closer values to experimentally observed times than in the model by Ramirez et al. Predictions using the model by Gale et al. resulted in times only slightly underestimated from experimentally observed times. The model proposed by Ramirez et al. predicted times that overestimated the processing times.

The Kaufman Binary Database predicted poor results in both models. The predicted solidification times were found to increase with temperature using these equilibrium constants. This is due to increased substrate saturation because of the decrease in the solidus composition with increasing temperature. As shown above in Figure 37, an increase in substrate saturation results in a longer isothermal solidification time. Interestingly, the equilibrium values from the Ni-DATA and ASM data sources produced values very close to each other in both models. This is despite the difference in calculated initial width which was used as the starting point of isothermal solidification.

5.3 Numerical Models for TLP Bonding

A major disadvantage of analytical modeling is that it cannot be used to model the process as a whole. The process is divided into stages corresponding to the different stages and each is modeled individually. Consequently, solute fields that have formed in previous stages are ignored which is a source of error. Also, many solutions rely on a parabolic growth law and error function solutions which are only approximate. Numerical solutions have the advantage that they can be applied to complex geometries including 2 or 3 dimensional shapes and allows the modeling of dissolution, isothermal

solidification and homogenization in one continuous model [74]. There were several models created to model the motion of the solid/liquid interface in transient liquid phase bonding. Binary component models mainly differ in the approach used to discretize the joint assembly and in numerical techniques used to solve the resulting systems of equations.

Nakagawa [81] and Cain [82] made the assumption that the interface was located at one of the discretization points. By incrementing the position of the interface to adjacent points, the time required to remove the deviation from equilibrium was calculated using Fick's law. In this way, the motion of the solid liquid interface was modeled in a step-wise manner. However, as the interface was fixed on a discretized node, the resulting calculated solute flux would inherit errors from the inaccurate interface position. More recent models by Zhou & North [71] and Shinmura [83] attempt to use a conservation of mass across the solid/liquid interface coupled to Fick's second law to determine the motion of the interface. In this type of model, the interface motion is tracked and is free to exist in-between discretization points. This type of model is referred to as the moving boundary model (MBM). These techniques are similar to the method used by Matan [73] and Akbay [84] which used similar techniques to model the growth of 2nd phases in nickel-base superalloys and steel respectively. These models however differ in the numerical techniques used. Shinmura used explicit finite difference methods while Zhou used an implicit finite difference method to reduce the number of computation iterations for this problem. An implicit finite difference model was also created by Illingworth using variable space discretization which provided faster computation times and had excellent agreement with other MBMs [85].

In the explicit scheme, the values at the previous time step are used explicitly to calculate future values. This has the unfortunate disadvantage of only being stable for small time steps and step sizes which can lead to protracted computation time but has the advantage of being easy to solve. The implicit scheme is more computationally intensive than the explicit scheme requiring the need to solve simultaneous linear equations at each time

step. However, the method is unconditionally stable for time steps and step sizes and can potentially reduce computation time [86].

Variations of the basic MBM model have been created in attempts to improve the understanding of the TLP bonding process. For example, Natsume created a MBM model which takes into account large changes in volume in the bond region during the TLP bonding of Al-Cu joints [87]. The model also took into account the effects of variations in bonding loads through the modification of the surface tension terms. Another variation was created by Natsume to test the effect of deviations from the local equilibrium assumption at the solid/liquid interface during fast heating rates [88].

While the majority of numerical modeling has focused on binary alloy systems there is an effort to model real systems by extending the computational modeling to ternary systems by Sinclair [89], Campbell & Boettinger [56] and Ohsasa [55]. Sinclair modeled the TLP bonding of a ternary two-phase system using an explicit finite difference model and utilized the concept of shifting tie lines due to changes in local equilibrium during the bonding. Campbell & Boettinger and Ohsasa used commercial thermodynamic software (Thermo-Calc) to determine the equilibrium tie lines at the solid liquid interface. The advantage of using such software is its potential for extension to higher order systems due to its flexibility for determining phase composition in multi-component systems.

5.3.1 Moving Boundary Models

A MBM is based on a finite difference discretization of the standard solution to Fick's 1st law. These models assume constant diffusion coefficients and determine the driving force of diffusion on the composition gradient between discretized nodes. What follows is an explicit discretization of the TLP bonding problem.

In the model used in the present work, a 1-dimensional model symmetric about the center of the joint was created to model the TLP bonding process. The joint assembly is assumed to be heated infinitely fast to the processing temperature thus avoiding the

effects of the heat-up phase. The dissolution of the interlayer is also ignored and is assumed to be fully liquid at the processing temperature with a MPD concentration equivalent to the initial concentration of the filler material used. The joint is discretized into a number of sub-systems, S_k of width Δz and interfaces, I_k with negligible width. The joint is symmetric about $I_k = I_1$. Treatment of phase boundary movement is accomplished with the introduction of an inter-phase node containing the solid/liquid interface. Within this discretized assembly, there exists a single two-phase system containing the solid/liquid interface located at $S_k = X$. A state of local equilibrium is assumed to exist at this interface. The bond assembly can be seen schematically below in Figure 40.

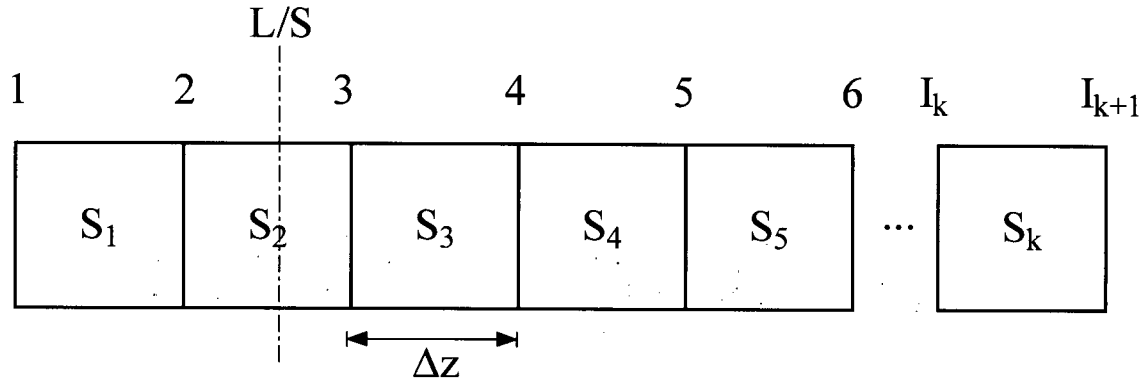


Figure 40 – Schematic diagram of interface node. The liquid/solid interface is shown by the dashed line and is located in sub-system $S_k = X = S_2$.

The molar volume is assumed to remain constant. The mass redistribution during a time step, Δt , can be calculated from the flux inputs and outputs according to Fick's 2nd law:

$${}^{t+\Delta t}C_i^{S_k} = {}^tC_i^{S_k} - [J_i^{I_k} - J_i^{I_{k-1}}] \cdot \Delta t / \Delta z \quad (26)$$

where C_i is the concentration of the solute species i in units of mols/m^3 . The flux of solute atoms between each sub-system, $J_i^{I_k}$, is calculated by Fick's 1st law:

$$J_i^{lk} = -\tilde{D}_i \cdot \frac{C_i^{S_k} - C_i^{S_{k-1}}}{\Delta z} \quad (27)$$

Where D_i refers to the diffusion coefficient of the MPD in the matrix present in that sub-system.

A liquid phase fraction vector f^L is used to represent the extent of solidification in the inter-phase node. Solidification is carried out such that it only occurs in the inter-phase node until complete transformation of that node is achieved. Once completed, the inter-phase system moves to the adjacent node until the entire assembly is solid. In this way, phase boundary motion is achieved discontinuously and the exact position of the interface can be determined by interpolation. The phase fraction is calculated by assuming that the compositions of the solid and liquid components of the inter-phase node are equal to their equilibrium compositions as defined by the binary phase diagram. Given the mean composition of the two-phase interface sub-system we can then determine the liquid phase fraction of the interface sub-system by the lever rule.

$$f^L = \frac{C - C^{SL}}{C^{LS} - C^{SL}} \quad (28)$$

where :

C = Concentration of the solute atom in the interface sub-system

C^{SL} = Solidus concentration of the solute atom

C^{LS} = Liquidus concentration of the solute atom

The fluxes on either side of the moving interface node are calculated using their relevant equilibrium compositions as determined by the isothermal processing temperature.

$$J_i^{lx} = -\tilde{D}^L \frac{C^{LS} - C^{X-1}}{\Delta z} \quad (29)$$

$$J_i^{l_{x+1}} = -\tilde{D}^s \frac{C^{SL} - C^{X+1}}{\Delta z} \quad (30)$$

where :

\tilde{D}^l = Diffusion coefficient of the solute species in the liquid phase

\tilde{D}^s = Diffusion coefficient of the solute species in the solid phase

Using this method, the solidification of the transient liquid is modeled discontinuously meaning at the end of solidification of one liquid sub-system, the following one must re-establish equilibrium before solidification continues.

5.3.2 Predictions from the Moving Boundary Model

The explicit MBM model was validated against models and experimental data by Zhou & North [74] and Illingworth [85] (Figure 41). In this simulation, the joining of plates of pure nickel was simulated using a Ni-19 at% P braze filler. Illingworth showed that the implicit model employed by Zhou & North did not conserve solute and exceeded the theoretical maximum width possible in the joint. The experimental data provided by Zhou & North also exceeded the theoretical maximum value, as determined by equation (15). It has been speculated by Illingworth that this error is the result of the questionable validity of the use of a constant molar volume assumption in the theoretical maximum width calculation used, or alternatively, the experimental results may have been affected by unaccounted liquid flow [85].

The moving boundary model used in the present work has excellent correlation with Illingworth's data produced by using an implicit numerical model. The predicted maximum width was similar to Illingworth's prediction and did not exceed the theoretical maximum width because the conservation of mass was also implemented in the MBM model created in the present work. The explicit scheme used in the MBM however is at a disadvantage in terms of computation speed when compared to implicit models. Illingworth's implicit model is reported to finish simulations such as the one shown in

Figure 41 in an order of minutes whereas the explicit model, which is limited by time step and step size instability, takes several hours for completion. However, this comparison shows the capability of this type of model to provide reasonable predictions for the processing time of a TLP bonding process.

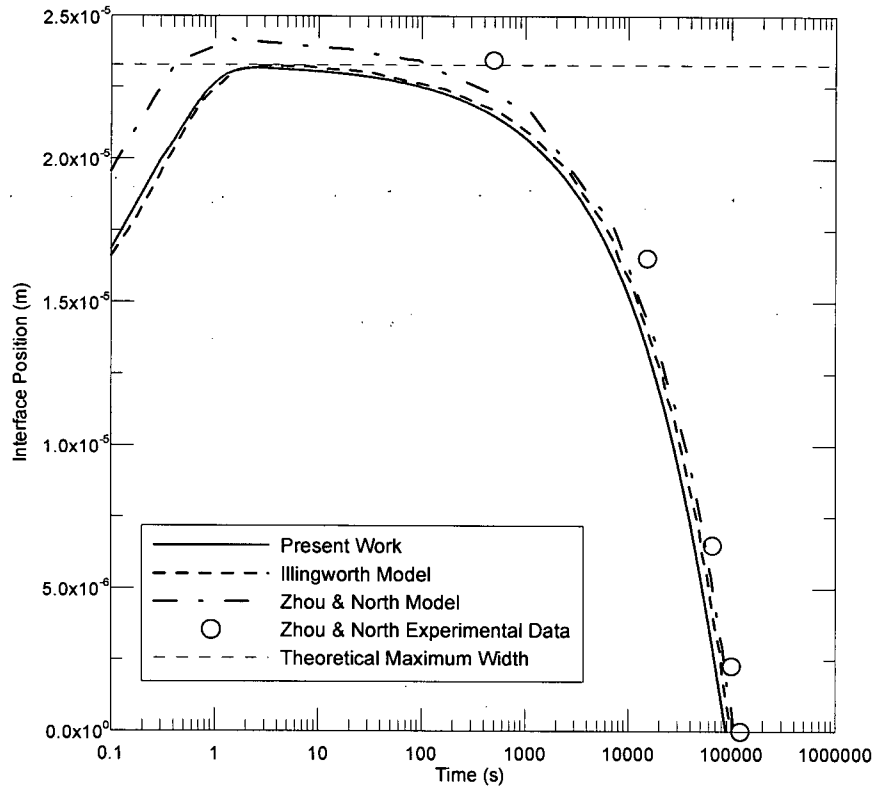
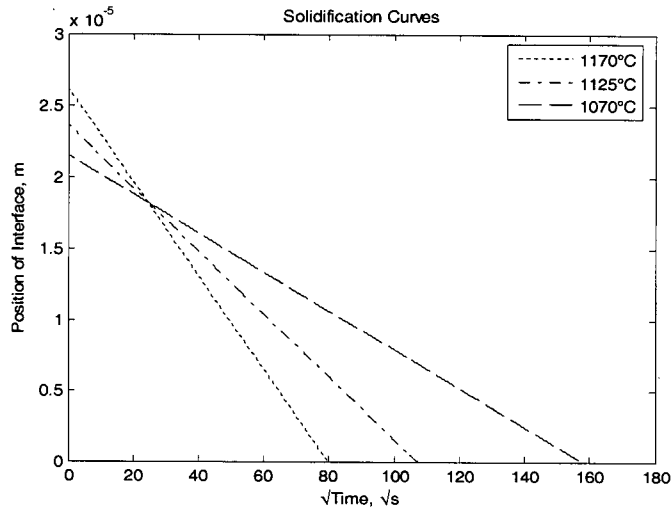


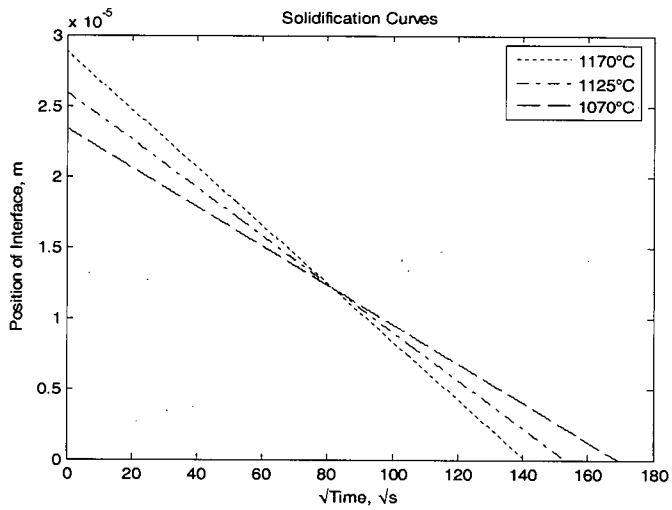
Figure 41 – Validation of the moving boundary model against other MBM (Zhou & North and Illingworth) and experimental data from Zhou & North [74, 85].

Simulations were performed of the bonding of joints at 1070°C, 1125°C and 1170°C with an initial half-liquid width of 20 μm . The compositions of the substrate and filler material were taken to be Ni-0.078 at% B and a Ni-18.1 at% B respectively. Equilibrium compositions are applied from the various databases as discussed earlier and the diffusion of boron in CM 247 LC is assumed from the experimentally measured value. The diffusion coefficient of boron in the liquid was taken to be $1 \times 10^{-8} \text{ m}^2/\text{s}$ [72]. The resulting eutectic width is plotted against the square root of time and is shown in Figure 42 and the predicted dissolution widths and times to completion of isothermal solidification are shown in Table 12 and Table 13.

Ni-DATA



Kaufman



ASM

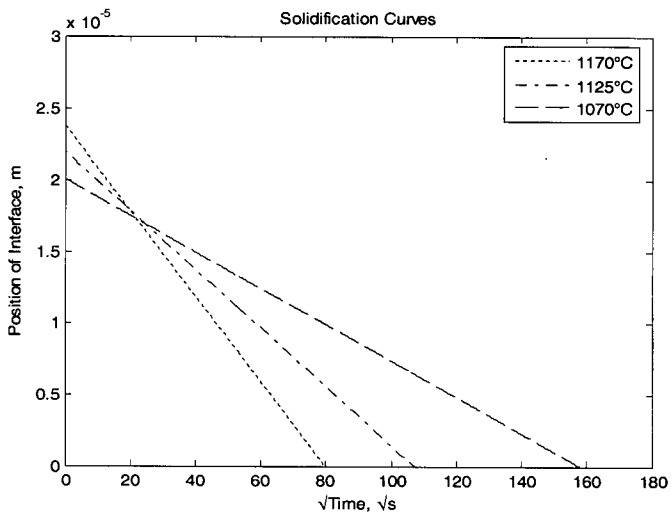


Figure 42 – Moving Boundary Model simulations of TLP bonds at 1070°C, 1125°C and 1170°C with Ni-0.078 at% B substrates and Ni-18.1 at% B filler material.

Table 12 – Predicted dissolution width using the moving boundary model vs. experimentally observed widths (microns).

Temperature	MBM Model			Experimental (+/- 2.5)
	Ni-DATA	Kaufman	ASM	
1070°C	43.0	46.8	40	47.5
1125°C	47.2	52.0	43.8	62.5
1170°C	52.2	57.6	47.6	67.5

Table 13 – Predicted solidification times using the moving boundary model vs. experimentally observed times (hours).

Temperature	MBM Model			Experimentally Extrapolated
	Ni-DATA	Kaufman	ASM	
1070°C	6.92	7.94	6.92	5.66
1125°C	3.18	6.52	3.18	2.23
1170°C	1.76	5.52	1.76	1.27

The model gives poor correlation with the predictions from the analytical solution for the dissolution widths. Like the analytical solution, the effect of the change in density between the liquid and solid phase is not taken into account in the present MBM model and may be a source of errors. Another source of error between the predicted values and the experimental data may arise from the binary component data used in the modeling when the experiments were performed on a complex superalloy and ternary component braze filler.

The predictions of bonding times are overestimated when compared to experimentally observed times. However, these results are better estimations compared to the Analytical solution proposed by Ramirez et al. The solidification times predicted by this MBM model for equilibrium data from the Ni-DATA and ASM Phase diagrams are very close despite predicting different dissolution widths. The trends observed in the predictions from this model suggest that the model is behaving in accordance with accepted models; however, the data on the nickel boron system requires further development. A large limitation of this model is that it will inherently be unable to predict the solidification in multi-component systems.

5.3.3 Phenomenological Model

The data available for higher order (above ternary) systems are scarce. Because of this, real systems cannot be represented by phase diagrams and only rough estimates of the behavior of a system can be modeled using binary component equilibrium data. Grushko and Weiss attempted to investigate the microstructure evolution of a braze joint in IN 718 using a complicated quasi-quaternary phase diagram on the Ni-Cr-Nb-Si system [90]. A possible solution to this problem is the use of computational thermodynamics through the CALculation of PHase Diagrams (CALPHAD) method which allows the calculation of chemical equilibrium in multi-component systems [77].

The CALPHAD method is based on the minimization of the free energy of a system and can be related to any alloy system and any number of components provided sufficient thermodynamic data are available. Extrapolation to higher order systems can also be calculated but may result in poor correlation to real systems. In the CALPHAD method there are many models that describe the Gibbs energy of a phase. For the commonly used sub-regular solution model, the molar Gibbs energy of a phase can be expressed as [91]:

$$g = g^{ref} + g_{mix}^{id} + g^{ex} \quad (31)$$

where g^{ref} is the reference energy, g_{mix}^{id} is the energy of ideal mixing and g^{ex} is the excess energy term representing interactions between different components in the system. Each of these terms can be calculated from the following equations:

$$g^{ref} = \sum_i x_i g_i^o \quad (32)$$

$$g_{mix}^{id} = RT \sum_i x_i \ln x_i \quad (33)$$

$$g^{ex} = x_j x_k \left(L_{jk} + L_{jk}^1 (x_j - x_k) + L_{jk}^2 (x_j - x_k)^2 + \dots \right) \quad (34)$$

where :

g_i^o = Reference energy of element i

x_i = Mole fraction of constituent i

L_{jk} = Interaction parameter between components j and k

The complexity of this thermodynamic description increases with the use of sub-lattices to differentiate substitutional and interstitial elements [92]. This calculation can be performed by using a thermodynamic calculator such as Thermo-Calc [93].

The goal of the coupled phenomenological model is to use experimentally measured thermodynamic and mobility databases to produce an accurate model with no adjustable parameters [94]. The diffusion of solute atoms can be modeled using a thermodynamic database by relating the diffusive flux to the Onsager force-flux equation. In this model, a thermodynamic description of the chemical system is coupled with a phenomenological description of the mobility of the solute atoms. With such a model, it is possible to model complex multi-component systems provided that accurate thermodynamic and kinetic data are available. The diffusive flux at each interface boundary is given by the Onsager force-flux relationship assuming a lattice-fixed frame reference[95]:

$$J_i^{l_k} = -\sum_{j=1}^C L_{ij}^{l_k} \nabla \mu_j^{l_k} \quad (35)$$

The flux equation is composed of a phenomenological parameter, $L_{ij}^{l_k}$, representing the mobility of the solute atoms and a thermodynamically derived chemical potential gradient, $\nabla \mu_j^{l_k}$, which represents the driving force for chemical equilibrium. At equilibrium, a system with constant temperature, pressure and composition, the chemical potential gradient is zero for all components and the Gibbs energy is at a minimum. Thus the driving force for diffusion is the chemical potential between two spatial points. The chemical potentials for a system of n components are related to the molar Gibbs energy by the Euler equation (equation 36). In this way the chemical potentials of a system can

be calculated for the phenomenological model. In this work this task is performed by using the commercial thermodynamic calculator: Thermo-Calc.

$$g = \sum_{i=1}^n \mu_i x_i \quad (36)$$

The chemical potential gradient at interface k for component j is calculated at the interface by the chemical potentials evaluated from the chemical potentials of the adjacent sub-systems:

$$\nabla \mu_j^{I,k} = \frac{\mu_j^{S_{k+1}} - \mu_j^{S_k}}{\Delta z} \quad (37)$$

where $\mu_j^{S_k}$ is the chemical potential of component j in sub-system S_k . The phenomenological parameter, L_{ij}^k , at each interface is evaluated by an average of the phenomenological parameters evaluated at the adjacent sub-systems, L_{ij} :

$$L_{ij} = C_i M_j = \frac{x_i}{\bar{V}_m} M_j \quad (38)$$

The mobility term, M_j , is calculated from an experimentally measured mobility database. The mobility term represents the ability of a solute atom to move and is dependant on composition, temperature and pressure. Andersson and Ågren determined in a simple disordered substitutional phase, such as the nickel-rich γ phase in a nickel-base superalloy, the off-diagonal terms of the diffusion mobility matrix are zero [95]. For the lattice-fixed frame of reference, the diagonal terms of the mobility matrix are calculated by [96]:

$$M_i = M_o \frac{1}{RT} \exp\left(\frac{\Delta G_i^*}{RT}\right) \quad (39)$$

where :

M_i = Mobility of species i in a given phase

M_o = Product of atomic jump distance squared and jump frequency

ΔG_i^* = Activation energy of diffusion of species i

M_o and ΔG_i^* are both dependant on composition, temperature and pressure, however, it is commonly accepted to assume that M_o has a value of $1 \text{ m}^2/\text{s}$ and to represent the combined dependence solely on ΔG_i^* which is expressed in terms of a Redlich-Kister polynomial [96]:

$$\Delta G_i^* = \sum_j x_j G_i^j + \sum_p \sum_{j>p} x_p x_j \sum_k G_i^{pj} (x_p - x_j)^k \quad (40)$$

where G_i^j and G_i^{pj} represent interaction parameters between the different atomic species and are linear functions of temperature and pressure.

The motion of the solid/liquid interface is tracked in the same way as in the MBM model. The phenomenological parameter in the inter-phase sub-system is calculated by evaluating the phenomenological parameters at the equilibrium concentrations on either side of the interface as defined by the local equilibrium assumption (L_{ij}^S, L_{ij}^L). The chemical potentials on either side of the solid liquid interface are calculated similarly.

5.3.4 Predictions from the Phenomenological Model

Simulations were performed using the above phenomenological model at 1070°C , 1125°C and 1170°C with an initial gap half-width of $20 \text{ }\mu\text{m}$. The simulation assumes the compositions of the substrate and filler are Ni-0.078 at% B and Ni-18.1 at% B

respectively. The Ni-DATA Superalloys Database was used for the thermodynamic description of the nickel-boron binary system. The kinetic description of this system was taken from the work of Campbell and Boettinger who determined that the diffusional activation energy for boron in a solid FCC nickel phase could be represented by the following relations in units of J/mol [56]:

Mobility of Boron

$${}^{FCC}G^{*Ni:B} = -94,500 - 110 * T$$

$${}^{FCC}G^{*Ni:Va} = -94,500 - 110 * T$$

Mobility of Nickel

$${}^{FCC}G^{*Ni:B} = -287,000 - 69.8 * T$$

$${}^{FCC}G^{*Ni:Va} = -287,000 - 69.8 * T$$

The superscript notation in each of the terms represents the species that contribute to the interaction energy. *Va* refers to the vacancies which are present in the sub-lattice model. However, it was noted by Campbell & Boettinger that these values required adjustment and provided poor predictions. To obtain agreement with experimental results the boron mobility was reduced by a factor of 3. In the same work it was assumed that the mobility of species in the liquid phase could be assumed to be $1 \times 10^{-9} \text{ m}^2/\text{s}$.

The motion of the interface calculated by the coupled phenomenological model and compared to data measured experimentally in this work is shown in Figure 43 and the predicted dissolution widths and isothermal solidification times calculated by the coupled phenomenological model are shown below in Table 14 and Table 15.

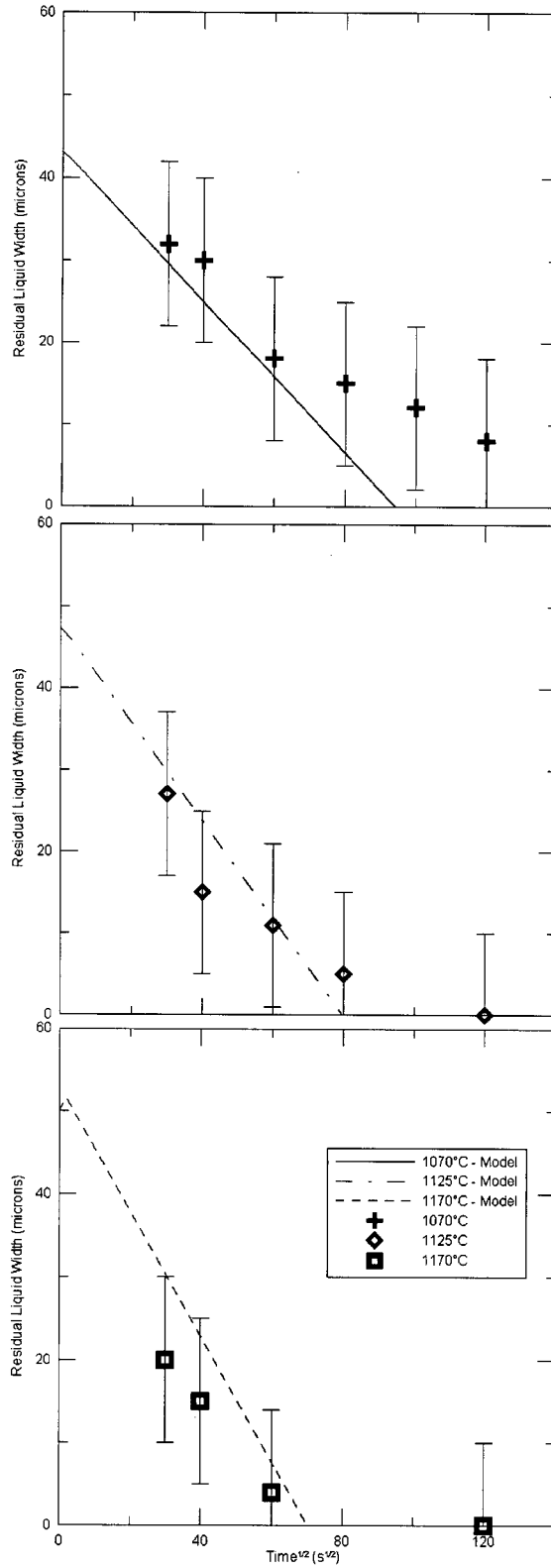


Figure 43 – Phenomenological model simulation of TLP bonding at 1070°C, 1125°C and 1170°C with Ni-0.078 at% B substrates and Ni-18.1 at% B filler material.

Table 14 – Predicted dissolution width using the coupled phenomenological model vs. experimentally observed widths (microns).

Temperature	Phenomenological Model	Experimental (+/- 2.5)
1070°C	43.0	47.5
1125°C	47.2	62.5
1170°C	52.2	67.5

Table 15 – Predicted solidification time using the coupled phenomenological model vs. experimentally observed times (hours).

Temperature	Phenomenological Model	Experimentally Extrapolated
1070°C	2.46	5.66
1125°C	1.76	2.23
1170°C	1.37	1.27

The predicted dissolution widths are underestimated in this model. The predicted maximum width is found to be equal to those predicted in the analytical models and the MBM model. As this model treats the dissolution of the base material similarly to the MBM model and shares the same equilibrium data values, it is not surprising that the values would be the same. The phenomenological model provides reasonable estimates of the solidification time at the highest temperature of 1170°C but is underestimated for lower temperatures. Of the two lower temperatures, the lowest temperature has the most error. The modification of the boron mobility was applied in the work of Campbell and Boettinger to account for the difference between experimentally observed data and the simulations performed at 1315°C. As this modification of the mobility term is not a temperature dependant, it is understandable that the predictions at the higher temperatures would be underestimated.

The phenomenological model used in this work is a binary model and does not take into account the interactions of the other elements in the thermodynamic description of the system or the mobility. Both of which have interaction parameters which depend on the concentrations of the other solute species. Furthermore, as noted by Campbell & Boettinger, the mobility description of boron in nickel is poorly defined in the literature

and requires refining. The current work contains a modified boron mobility which is questionable. In this case, the phenomenological model was not capable of accurately modeling the TLP bonding process due to lack of reliable data.

Another drawback of the current phenomenological model is that it is significantly slower than the regular MBM model due to the complicated calculations required. An expansion of the model to multiple components would further protract the calculation time. A revised numerical scheme should be considered and an implicit method should be utilized as this would allow the model to operate under a larger time step and allow a coarser discretization mesh which would significantly reduce the number of iterations (and computation time) that would be required for the model to reach completion.

Chapter 6

Conclusions

6.1 Summary

In this work, the Transient Liquid Phase (TLP) bonding technique was investigated for the joining of the nickel-base superalloy CM 247 LC. The following conclusions were made from this work:

- The liquid widths in all bonds were found to reduce linearly with the square root of time during isothermal solidification. The rate of solidification was observed to be greater on samples bonded at higher temperatures. However, it was found that the completion of isothermal solidification was not sufficient for good mechanical properties in the joints. Tensile tests showed brittle joints in samples created at all processing conditions including those that completed isothermal solidification. SEM analysis of the fracture surfaces showed evidence of boron containing precipitates. Post-bond heat treatment would likely improve the joint properties by dissolving the precipitates in the base metal and allow the diffusion of alloying additions not present in the joint to diffuse from the base material and homogenize the bond.

- In incompletely isothermal solidified joints, a binary eutectic consisting of nickel solid solution and nickel borides as well as a ternary eutectic consisting of a mixture of nickel solid solution, chromium borides and nickel borides was found in the residual liquid. This centerline phase was much harder than the base material with average micro-hardness values of 850 HV0.0025 compared to the base material with a nominal hardness of 450 HV0.0025. The existence of these phases is detrimental to the properties of the joints because of their brittle properties and their continuous morphology along the joint interface.
- Bordering either side of the centerline eutectic was a proeutectic solid solution nickel-rich phase. This was formed by the isothermal solidification process. The isothermally solidified microstructure was softer than the base material with an average hardness of 400 HV0.0025. EDS scans across this interface showed it to be deficient in many of the alloying elements necessary for the formation of the γ' phase necessary for a good joint. Homogenization did occur during bonding with evidence of cuboidal precipitates existing in the isothermal solidification region in samples processed at higher temperatures and longer duration. This is likely due to the diffusion of said alloying elements into this region which is promoted by the higher temperature and longer processing time.
- In all samples, the base material contained precipitation from the diffusion of boron from the filler material into the substrate. Blocky and acicular precipitates were observed in the regions adjacent to the joint/substrate interface. Blocky precipitates further away from the center of the joint were observed to be aligned in the direction of acicular precipitates. EDS analysis showed the precipitates were similar in composition despite the difference in morphology. The precipitates were slightly nickel depleted and tungsten rich compared to the surrounding material and contained detectable levels of boron indicating these precipitates may be nickel-borides. The precipitates in the base metal increased the hardness adjacent to joint interface exhibiting average hardness values of 600

HV0.0025 compared to the base metal with an average of 100 HV0.0025. The precipitation of these phases could also be a cause of poor joint properties.

- The apparent diffusion coefficient of boron in CM 247 LC was experimentally measured by observing the rate of isothermal solidification. The apparent activation energy is found to be 219 KJ/mol with a pre-exponential factor $D_0 = 0.0163 \text{ m}^2/\text{s}$. These values are similar to values in the literature for the diffusion of boron in other polycrystalline superalloys.
- Modeling of dissolution stage using analytical and numerical models were found to be inadequate for predicting the experimentally observed dissolution width of the TLP bonding of CM 247 LC with the commercial Ni-Cr-B-C filler alloy. The assumption of constant density between the solid and liquid phases is likely a source of error in this calculation.
- The data in the literature on the Ni-B system is lacking with scarce data available on both thermodynamics and kinetics. Isothermal solidification times were calculated using analytical and numerical models. The analytical model proposed by Gale et al. predicted better isothermal solidification times than the model by Ramirez et al. The numerical model developed under the MBM scheme predicted satisfactory isothermal solidification times but were overestimated in all cases. The phenomenological model produced satisfactory results for 1170°C but underestimated the isothermal solidification times for lower temperatures. Inaccurate predictions were produced with thermodynamic data from the Kaufman Binary Alloy Database while better predictions were possible with the Ni-DATA database and ASM phase diagram. The current mobility data available for boron is inadequate for a phenomenological model to be applied.

6.2 Recommendations for Future Work

- This study was performed with only one gap size and filler material composition. As the gap size will vary especially in repair and overhaul applications, data on the microstructures produced with joints of varying sizes is vital. Furthermore, it is unknown if the composition of the filler material used is optimal. Commercial braze fillers are available with a higher level of alloying and can possibly improve joint properties and/or reduce processing time.
- The refractory element rich precipitates that were observed in the base material require further analysis. Currently the understanding of the mechanism of their formation is lacking. TEM work should be performed to properly characterize and understand these precipitates.
- The tensile properties of the bonded joints were poor. An addition of a post-bond heat treatment would most likely improve the properties because of the dissolution of precipitates in the bond microstructure and the homogenization of strengthening alloying additions. Further work is needed to optimize post-bond heat treatment.
- The phenomenological model created in this work is based on the binary Ni-B system. The model can be further expanded to multi-component systems which represent the real superalloy systems. An expansion of this model to a multicomponent model could potentially improve its accuracy with respect to experimentally observed data since the phenomenological model allows for no fitting parameters. The quality of the predictions made by a phenomenological model is based entirely on the available data.
- Predictions of isothermal solidification time using the phenomenological model produced poor results compared to the other models (numerical and analytical) and experimentally observed data. Further, the boron mobility in the literature is modified by a factor which is not appropriate. This indicates that the data used in

the phenomenological model is not refined to the point where it can reliably predict isothermal solidification in the current alloying system. Further development of the kinetic and thermodynamic descriptions of boron and its interactions with alloying elements in the superalloys system is required. Interactions between boron and elements other than nickel and aluminum are not currently available in the literature.

References

1. Sims, C. T., (1984). "A history of superalloy metallurgy for superalloy metallurgists." *Superalloys 1984*, TMS, Champion, PA, pp. 399-419.
2. Commercial High Bypass Turbofan Engines: Rolls-Royce Trent 1000 Engine.
<http://www.aircraftenginedesign.com/> 2005.
3. Chaturvedi, M. C. and Richards, N. L., (2004). "Repair and overhaul of hot end gas turbine components." 41st Annual Conference of Metallurgists of CIM COM 2002, MetSOC, Montreal Quebec Canada, pp. 5-19.
4. Duvall, D. S., Owczarski, W. A., and Paulonis, D. F., "TLP bonding: a new method for joining heat resistant alloys," *Welding Journal*, Vol. 53, 1974, pp. 203-214.
5. Zhou, Y., Gale, W. F., and North, T. H., "Modeling of transient liquid phase bonding," *International Materials Review*, Vol. 40, No. 5, 1995, pp. 181-196.
6. Harris, K., Erikson, G. L., Sikkenga, S. L., Brentnall, W. D., Aurrecoechea, I. M., and Kubarych, K. G., (1992). "Development of the rhenium containing superalloys CMSX-4® & CM 186 LC® for single crystal blade and directionally solidified Vane applications in advanced turbine engines." *Superalloys 1992*, TMS, Champion, PA, pp. 297-306.
7. McLean, M., *Directionally solidified materials for high temperature service*, The Metals Society, London, 1983.
8. Harris, K., Erikson, G. L., and Schwer, R. E., "Directionally solidified and single crystal superalloys," *ASM Handbooks Volume 1, Properties and Selection: Irons, Steels, and High Performance Alloys* ASM International, 2004, pp. 995-1006.
9. Donachie, M. J. and Donachie, S. J., *Superalloys: a technical guide*, 2nd ed., ASM International, Materials Park, 2002, pp. 339-351.
10. Smith, W. F., "Nickel and cobalt Alloys," *Structures and Properties of Engineering Alloys* McGraw-Hill, 1993, pp. 487-536.
11. Sims, C. T., Hagel, W. C., and Stoloff, N. S., *Superalloys II*, John Wiley and Sons, New York, 1987.
12. Sims, C. T. and Hagel, W. C., *The Superalloys*, John Wiley and Sons, New York, 1972.
13. Murakumo, T., Kobayashi, T., Koizumi, Y., and Harada, H., "Creep behavior of Ni-base single-crystal superalloys with various volume fraction," *Acta Materialia*, Vol. 52, No. 12, 2003, pp. 3737-3744.
14. Harris, K., Erikson, G. L., and Schwer, R. E., (1984). "MAR-M 247 Derivations - CM 247 LC DS alloy CMSX single crystal alloys properties and performance." *Superalloys 1984*, TMS, Champion, PA, pp. 221-230.
15. Antony, K. C. and Goward, G. W., (1988). "Aircraft gas turbine blade and vane repair." *Superalloys 1988*, TMS, Champion, PA, pp. 745-754.

16. Su, C. Y., Chou, C. P., Wu, B. C., and Lih, W. C., "Plasma transferred arc repair welding of the nickel-base superalloy IN-738 LC," *Journal of Materials Engineering and Performance*, Vol. 6, No. 5, 1997, pp. 619-627.
17. Williams, A. D. and Humphries, J. L., (1998). "Latest gas turbine repair techniques using laser technology." Proceedings of the International Thermal Spray Conference, ASM International, Nice, pp. 1431-1435.
18. Reed, R. C., Stone, H. J., Dye, D., and Roberts, S. M., (2000). "Process modeling of electron beam welding of aero-engine components." TMS, Champion, PA, pp. 665-674.
19. Yeniscavich, W., "Joining," *Superalloys II*, edited by C. T. Sims, N. S. Stoloff, and W. C. Hagel John Wiley & Sons, New York, 1987, pp. 495-516.
20. Ojo, O. A., Richards, N. L., and Chaturvedi, M. C., "Microstructural study of weld fusion zone of TIG welded IN-738 LC nickel-based superalloy," *Scripta Materialia*, Vol. 51, No. 7, 2005, pp. 683-688.
21. Ojo, O. A., Richards, N. L., and Chaturvedi, M. C., "Contribution of constitutional liquation of gamma prime precipitate to weld HAZ cracking of cast Inconel 738 superalloy," *Scripta Materialia*, Vol. 50, No. 5, 2004, pp. 641-646.
22. Schwartz, M. M., "Fundamentals of brazing & soldering," *ASM Handbooks: Volume 6, Welding, Brazing and Soldering* ASM International, 1993, pp. 109-126.
23. Gandy, D. W., Frederick, G., Stover, J. T., and Viswanathan, R., "Overview of hot section component repair methods," *ASM International Materials Solutions Conference 2000 Gas Turbine Materials Technology Session*, 2000.
24. Metglas Brazing Foils. www.metglas.com 2005. Conway, SC, Honeywell Metglas Solutions.
25. Gale, W. F. and Butts, D. A., "Transient liquid phase bonding," *Science and Technology of Welding and Joining*, Vol. 9, No. 4, 2004, pp. 283-300.
26. Demo, W. A., Ferrigno, S., Budinger, D., and Huron, E., (2004). "Improving repair quality of turbine nozzles using SA650 braze alloy." *Superalloys 2000*, TMS, Champion, PA, pp. 713-720.
27. Manente, D., "Brazing of heat resistant alloys," *ASM Handbooks: Volume 6, Welding, Brazing and Soldering* ASM International, Metals Park, Ohio, 1993, pp. 924-930.
28. Miglietti, W., "Advantages of fluoride ion cleaning at sub-atmospheric pressure," *Engineering Failure Analysis*, Vol. 5, No. 2, 2003, pp. 149-169.
29. MacDonald, W. D. and Eagar, T. W., "Transient liquid phase bonding," *Annual Review of Materials Science*, 1992, pp. 23-46.
30. MacDonald, W. D. and Eagar, T. W., (1992). "Transient liquid phase bonding processes." *The Metal Science of Joining*, TMS, Chincinnati, OH, pp. 93-100.
31. Kim, D. U. and Nishimoto, K., "Creep rupture and fatigue properties of transient liquid phase bonded joints of Ni base single crystal superalloy," *Materials Science and Technology*, Vol. 19, No. April, 2003, pp. 456-460.
32. Pallos, K. J., "Gas turbine repair technology," General Electric Power Systems, GER-3957B, Atlanta, GA, 2004.

33. Cooke, L. A., "Airfoil repair: enabling technologies extended life and reduce costs," *Modern Power Systems*, No. 8, 2004.
34. Nakao, Y., Nishimoto, K., and Shinozaki, K., (1988). "Theoretical research on transient liquid insert metal diffusion bonding of nickel base alloys." *Superalloys 1988*, TMS, Champion, PA, pp. 775-783.
35. Corbin, S. F. and McIsaac, D. J., "Differential scanning calorimetry of the stages of transient liquid phase sintering," *Materials Science & Engineering A*, 2003, pp. 132-140.
36. Zhuang, W. D. and Eagar, T. W., "Liquid infiltrated powder interlayer bonding: process for large gap joining," *Science and Technology of Welding and Joining*, Vol. 5, No. 3, 2000, pp. 125-134.
37. Sulzer Metco Activated Diffusion Braze. <http://www.sulzermetco.com> . 2005.
38. Orel, S. V., Parous, L. C., and Gale, W. F., "Diffusion brazing of nickel aluminides," *Welding Research Supplement*, 1995, pp. 319-s-324-s.
39. Yang, T. Y., Wu, S. K., and Shiue, R. K., "Interfacial reaction of infrared brazed NiAl/Al/NiAl and Ni3Al/Al/Ni3Al joints," *Intermetallics*, Vol. 9, No. 4, 2001, pp. 341-347.
40. Abdo, Z. A. M. and Gale, W. F., "Microstructural development of transient liquid phase bonds between NiAl and nickel-bearing substrates," *Proceedings from Materials Solutions Conference '99 on Joining of Advanced and Specialty Materials*, 1999, pp. 64-71.
41. Gale, W. F. and Abdo, Z. A. M., "Bulk-alloy microstructural analogues for transient liquid-phase bonds in the NiAl/Cu/Ni system," *Metallurgical and Materials Transactions A*, Vol. 30A, No. 12, 1999, pp. 3111-3124.
42. Tseng, M. W. and Williams, D. B., "Microstructural evolution during transient liquid-phase bonding in a Ni-base superalloy/sapphire fibre composite," *Journal of Materials Science*, Vol. 34, 1999, pp. 5187-5197.
43. Jung, J.-P., Lee, B.-Y., and Kang, K.-S., (1992). "Liquid phase diffusion bonding using high diffusivity - and high melting point - element as insert material." *International Trends in Welding Science and Technology*, ASM International, Gatlinburg, Tennessee, pp. 1101-1105.
44. Nishimoto, K., Saida, K., Kim, D. U., Asai, S., Furukawa, Y., and Nakao, Y., "Bonding phenomena and joint properties of transient liquid phase bonding of Ni-base single crystal superalloys.," *Welding in the World*, Vol. 41, No. 2, 1998, pp. 121-131.
45. Li, W., Jin, T., Sun, X. F., Guo, Y., Guan, H. R., and Hu, Z. Q., "Study of Ni-Cr-Co-W-Mo-B interlayer alloy and its bonding behaviour for a Ni-base single crystal superalloy," *Scripta Materialia*, Vol. 48, 2003, pp. 1283-1288.
46. Liao, P. K. and Spear, K. E., "Binary phase diagrams," *ASM Handbooks: Volume 3, Alloy Phase Diagrams* ASM International, 1991.
47. Gale, W. F. and Wallach, E. R., "Microstructural development in transient liquid-phase bonding," *Metallurgical and Materials Transactions A*, Vol. 22A, No. 10, 1991, pp. 2451-2457.
48. Tung, S. K., Lim, L. C., Lai, M. O., and Wu, H., "Evolution of nickel borides in Ni-Si-B brazed joints of nickel during post braze heat treatment," *Materials Science and Technology*, Vol. 13, 2005, pp. 1051-1056.

49. Su, C. Y., Chou, C. P., Wu, B. C., and Lih, W. C., "Microstructural characterization of transient liquid phase zone of activated diffusion brazed nickel base superalloy," *Materials Science and Technology*, Vol. 15, No. 3, 1999, pp. 316-322.
50. Rabinkin, A., "Overview: brazing with (NiCoCr)-B-Si amorphous brazing filler metals: alloys, processing, joint structure, properties, applications," *Science and Technology of Welding and Joining*, 2003.
51. Rabinkin, A., "Brazing with (NiCoCr)-B-Si amorphous brazing filler metals: alloys, processing, joint structure, properties, applications.," *Science and Technology of Welding and Joining*, Vol. 9, No. 3, 2004, pp. 181-199.
52. Wu, X., Chandel, R. S., and Li, H., "Evaluation of transient liquid phase bonding between nickel-based superalloys," *Journal of Materials Science*, Vol. 36, No. 6, 2001, pp. 1539-1546.
53. Wu, X., Chandel, R. S., Hang, L., Seow, H. P., and Wu, S., "Induction brazing of Inconel 718 to Inconel X-750 using Ni-Cr-Si-B amorphous foil," *Journal of materials processing technology*, Vol. 104, No. 1, 2000, pp. 34-43.
54. Broomfield, R. W., (2003). "Development of brazing techniques for the joining of single crystal components." Proceedings of the Fifth International Charles Parsons Turbine Conference 3-7 July 2000, Churchill College, Cambridge, UK, pp. 741-754.
55. Ohsasa, K., Shinmura, T., and Narita, T., "Numerical modelling of the transient liquid phase bonding process of Ni using Ni-B-Cr ternary filler metal," *Journal of Phase Equilibria*, Vol. 20, No. 3, 1999, pp. 199-206.
56. Campbell, C. E. and Boettinger, W. J., "Transient liquid-phase bonding in the Ni-Al-B system," *Metallurgical and Materials Transactions A*, Vol. 31A, No. Nov., 2000, pp. 2835-2847.
57. Niemann, J. T. and Garrett, R. A., "Eutectic bonding of boron-aluminum structural components," *Welding Research*, 1974, pp. 175s-184s.
58. Ojo, O. A., Richards, N. L., and Chaturvedi, M. C., "Effect of gap size and process parameters on diffusion brazing of Inconel 738.," *Science and Technology of Welding and Joining*, Vol. 9, No. 3, 2004, pp. 209-220.
59. Idowu, O. A., Richards, N. L., and Chaturvedi, M. C., "Effect of bonding temperature on isothermal solidification rate during transient liquid phase bonding of Inconel 738 LC superalloy," *Materials Science & Engineering A*, Vol. 397, No. 1, 2005, pp. 98-112.
60. Nakahashi, M., Suenaga, S., Shirokane, M., and Takeda, H., "Transient liquid phase bonding for Ni-base superalloys, MAR-M 247 and IN-939," *Materials Transactions, JIM*, Vol. 33, No. 1, 1992, pp. 60-65.
61. Kokawa, H., Lee, C. H., and North, T. H., "Effect of grain boundaries on isothermal solidification during transient liquid phase brazing," *Metallurgical and Materials Transactions A*, Vol. 22A, No. 07, 1991, pp. 1627-1631.
62. Saida, K., Zhou, Y., and North, T. H., "The influence of base metal grain size on isothermal solidification during transient liquid-phase brazing of nickel," *Journal of Materials Science*, Vol. 28, 1993, pp. 6427-6432.

63. Ojo, O. A., Richards, N. L., and Chaturvedi, M. C., "Isothermal solidification during transient liquid phase bonding of Inconel 738 superalloy," *Science and Technology of Welding and Joining*, Vol. 9, No. 6, 2004, pp. 532-540.
64. DeAnonio, D. A., Duhl, D. N., Howson, T., and Rothman, M. F., "Cast superalloy heat treatment," *ASM Handbooks: Volume 4, Heat Treating* ASM International, 1993, pp. 793-814.
65. Zeisler-Mashl, K. L. and Pletka, B. J., (1992). "Segregation during solidification in the MAR-M 247 system." *Superalloys 1992*, TMS, Champion, PA, pp. 175-184.
66. Pope, M. I. and Judd, M. D., *Differential thermal analysis: a guide to the technique and its applications*, Heyden & Son Ltd., London, UK, 1977.
67. Fuchs, G. E., "Solution heat treatment response of a third generation single crystal Ni-base superalloy," *Materials Science & Engineering A*, Vol. 300, No. 1-2, 2004, pp. 52-60.
68. Williams, D. B. and Carter, C. B., "Quantitative x-ray microanalysis," *Transmission Electron Microscopy* Plenum Press, New York, 1996, pp. 597-620.
69. Roebuck, B., Cox, D. C., and Reed, R. C., (2004). "An innovative device for the mechanical testing of miniature specimens of the superalloys." *Superalloys 2004*, TMS, Champion, PA, pp. 523-528.
70. Karunaratne, M. and Reed, R. C., "Interdiffusion of the platinum-group metals in nickel at elevated temperatures," *Acta Materialia*, Vol. 51, No. 10, 2003, pp. 2905-2919.
71. Zhou, Y. and North, T. H., "Kinetic modelling of diffusion-controlled, two phase moving interface problems," *Modelling and Simulation in Materials Science and Engineering*, Vol. 1, No. 4, 1993, pp. 505-516.
72. Ramirez, J. E. and Liu, S., "Diffusion brazing in the nickel-boron system," *Welding Journal*, Vol. 71, 1992, pp. 365-s-375-s.
73. Matan, N., Winand, H. M. A., Carter, P., Karunaratne, M., Bogdanoff, P. D., and Reed, R. C., "A coupled thermodynamic / kinetic model for diffusional processes in superalloys," *Acta Materialia*, Vol. 46, No. 13, 1998, pp. 4587-4600.
74. Zhou, Y. and North, T. H., "Process modelling and optimized parameter selection during transient liquid phase bonding," *Zeitschrift Fur Metallkunde*, Vol. 85, No. 11, 1994, pp. 775-780.
75. Crank, J., "Infinite and semi-infinite media," *The mathematics of diffusion* Clarendon Press, Oxford, 1975, pp. 28-43.
76. *TCW Thermodynamic and Database Guide*, Thermo-Calc Software AB, Stockholm, Sweden, 2005.
77. Saunders, N., (1996). "Phase diagram calculations for Ni-based superalloys." *Superalloys 1996*, TMS, Champion, PA, pp. 101-110.
78. Wang, W., Zhang, S., and He, X., "Diffusion of boron in alloys," *Acta Metallurgica & Materialia*, Vol. 43, No. 4, 1995, pp. 1693-1699.
79. Nishimoto, K., Saida, K., Kim, D. U., and Nakao, Y., "Transient liquid phase bonding of Ni-base single crystal superalloy, CMSX-2," *ISIJ International*, Vol. 35, No. 10, 1995, pp. 1298-1306.
80. Sinclair, C. W., "Modelling transient liquid phase bonding in multicomponent systems," *Journal of Phase Equilibria*, Vol. 20, No. 4, 1999, pp. 361-369.

81. Nakagawa, H., Lee, C. E., and North, T. H., "Modelling of base metal dissolution behavior during transient liquid-phase brazing," *Metallurgical and Materials Transactions A*, Vol. 22A, No. 2, 1991, pp. 543-555.
82. Cain, S. R., Wilcox, J. R., and Venkatraman, R., "A diffusional model for transient liquid phase bonding," *Acta Metallurgica & Materialia*, Vol. 45, No. 2, 2003, pp. 701-707.
83. Shinmura, T., Ohsasa, K., and Narita, T., "Isothermal solidification behavior during the transient liquid phase bonding process of nickel using binary filler metals," *Materials Transactions, JIM*, Vol. 42, No. 2, 2001, pp. 292-297.
84. Akbay, T., Reed, R. C., and Atkinson, C., "Modelling re-austenitisation from ferrite/cementite mixtures in Fe-C steels," *Acta Metallurgica & Materialia*, Vol. 42, No. 4, 1994, pp. 1469-1480.
85. Illingworth, T. C., Golosney, I. O., Gergely, V., and Clyne, T. W., "Numerical modelling of transient liquid phase bonding and other diffusion controlled phase changes," *Journal of Materials Science*, Vol. 40, No. 9-10, 2005, pp. 2505-2511.
86. Gerald, C. F. and Wheatley, P. O., *Applied Numerical Analysis*, 4th ed. ed., Addison-Wesley Publishing Company, Reading, Massachusetts, 1989.
87. Natsume, Y., Ohsasa, K., and Tayu, Y., "Numerical modeling of the transient liquid-phase diffusion bonding process of Al using Cu filler metal," *ISIJ International*, Vol. 43, No. 12, 2003, pp. 1976-1982.
88. Natsume, Y., Ohsasa, K., and Narita, T., "Phase-field simulation of transient liquid phase bonding process of Ni using Ni-P binary filler metal," *Materials Transactions, JIM*, Vol. 44, No. 5, 2003, pp. 819-823.
89. Sinclair, C. W., Purdy, G. R., and Morral, J. E., "Transient liquid phase bonding in two-phase ternary systems," *Metallurgical and Materials Transactions A*, Vol. 31A, No. 04, 2000, pp. 1187-1192.
90. Grushko, B. and Weiss, B. Z., "Structure of vacuum brazed BNi-5 joint of Inconel 718," *Metallurgical and Materials Transactions A*, Vol. 15A, 1984, pp. 609-620.
91. Campbell, C. E. and Kattner, U. R., "A thermodynamic assessment of the Ni-Al-B system," *Journal of Phase Equilibria*, Vol. 20, No. 5, 1999, pp. 485-496.
92. Kattner, U. R., "Thermodynamic modeling of multicomponent phase equilibria," *Journal of Materials*, Vol. 49, No. 12, 1997, pp. 14-19.
93. Sundman, B., "Summary of the modules of Thermo-Calc," The Royal Institute of Technology, D53, Stockholm, Sweden, 1984.
94. Engström, A., Höglund, L., and Ågren, J., "Computer simulation of diffusion in multiphase systems," *Metallurgical and Materials Transactions A*, Vol. 25A, No. 06, 1994, pp. 1127-1134.
95. Andersson, J. and Ågren, J., "Models for numerical treatment of multicomponent diffusion in simple phases," *Journal of Applied Physics*, Vol. 72, No. 4, 1992, pp. 1350-1355.
96. Campbell, C. E., Boettinger, W. J., and Kattner, U. R., "Development of a diffusion mobility database for Ni-base superalloys," *Acta Materialia*, Vol. 50, 2002, pp. 775-792.

Appendices

Appendix A - Analytical Solution for the Interlayer Dissolution Stage

In this stage the dissolution of solid interlayer is modeled. There exist two simultaneous moving interfaces as shown in Figure 32. It is assumed that the process is controlled by Fick's 2nd law:

$$\frac{\partial C_i^L}{\partial t} = \tilde{D}^L \frac{\partial^2 C_i^L}{\partial y^2} \quad (1)$$

where \tilde{D}^L is the diffusion coefficient in of the solute atom in the liquid phase, C_i^L is the solute concentration and y is the distance. If we further assume:

- The diffusion coefficients are constant and not composition dependant
- Local equilibrium exists at the solid/liquid interfaces
- Semi-infinite domains

then Fick's 2nd law has a standard solution given by an error function expression:

$$C_i = A + B \cdot \text{erf} \left(\frac{y}{\sqrt{4\tilde{D}^L t}} \right) \quad (2)$$

where A and B are constants. We can now define the displacement, y , at a given time, t , for each phase, α and β :

$$y^\alpha = K^\alpha \sqrt{4\tilde{D}^L t} \quad (3)$$

$$y^\beta = K^\beta \sqrt{4\tilde{D}^L t} \quad (4)$$

where K^i is the non-dimensional growth rate constant for phase i . Taking the derivative of these expressions with respect to time we get the expressions for interface velocity:

$$\frac{dy^\alpha}{dt} = \frac{\partial}{\partial t} K^\alpha \sqrt{4\tilde{D}^L t} = \frac{K^\alpha \tilde{D}^L}{\sqrt{\tilde{D}^L t}} = K^\alpha \sqrt{\frac{\tilde{D}^L}{t}} \quad (5)$$

$$\frac{dy^\beta}{dt} = \frac{\partial}{\partial t} K^\beta \sqrt{4\tilde{D}^L t} = \frac{K^\beta \tilde{D}^L}{\sqrt{\tilde{D}^L t}} = K^\beta \sqrt{\frac{\tilde{D}^L}{t}} \quad (6)$$

Taking the derivative of the standard solution with respect to K we get the concentration gradient:

$$\frac{\partial C_i^{\alpha,L}}{\partial y} = \frac{B \exp(-K^\alpha)^2}{\sqrt{\pi \tilde{D}^L t}} \quad (7)$$

$$\frac{\partial C_i^{\beta,L}}{\partial y} = \frac{B \exp(-K^\beta)^2}{\sqrt{\pi \tilde{D}^L t}} \quad (8)$$

A mass balance at each of these interfaces provides the velocity of each of the interfaces:

$$\frac{dy}{dt} = \frac{\tilde{D}^L}{C_i^{\alpha o} - C_i^{\alpha,LS}} \left. \frac{\partial C^L}{\partial y} \right|_{y=y^\alpha} \quad (9)$$

$$\frac{dy}{dt} = \frac{-\tilde{D}^L}{C_i^{\beta o} - C_i^{\beta,LS}} \left. \frac{\partial C^L}{\partial y} \right|_{y=y^\beta} \quad (10)$$

Substituting the above derivatives into the mass balances and considering only the diffusion of solute atoms in two semi-infinite planes located between $y = 0$ & $y = y^\alpha$ &

$y = y^\beta$ & $y = \infty$ with the following boundary conditions we get two explicit expressions of the dimensionless growth constants:

- K is dependant on t
- $C = C^o$ at $y = 0$
- $C = C^{\alpha,LS}$ at $y = y^\alpha$
- $C = C^{\beta,LS}$ at $y = y^\beta$
- $C = C^\infty$ at $y = \infty$

$$\frac{C_i^\infty - C_i^{\beta,LS}}{C_i^{\alpha,LS} - C_i^o} K^\beta \exp(K^{\beta^2} - K^{\alpha^2}) - K^\alpha = 0 \quad (11)$$

$$\frac{C_i^o - C_i^{\alpha,LS}}{C_i^{\alpha,LS} - C_i^\infty} K^\alpha \sqrt{\pi} [\operatorname{erf}(K^\beta) - \operatorname{erf}(K^\alpha)] - \exp(-K^{\alpha^2}) = 0 \quad (12)$$

We can solve for the dimensionless growth constants by simultaneously solving these two equations. The time for dissolution of the braze interlayer of initial thickness $2h$ at a given temperature can be calculated from the following equation:

$$t_d = \frac{(2h)^2}{16K^{\beta^2} \tilde{D}^L} \quad (13)$$

The width of the liquid interlayer at the completion of dissolution is:

$$W_L = 2h + 2K^\alpha \sqrt{D^L t_d} \quad (14)41$$

Appendix B - Analytical Solution for the Widening and Homogenization Stage

After the establishment of a fully liquid interlayer, further dissolution of the parent metal takes place as solute diffuses from the liquid into the solid substrate. This process proceeds until the liquid is fully homogenized and has a concentration equal to the liquidus. Similar to the previous stage, the concentrations in the solid (S) and liquid (L) regions will vary according to Fick's 2nd Law:

$$\frac{\partial C_i^S}{\partial t} = \tilde{D}^S \frac{\partial^2 C_i^S}{\partial z^2} \quad (1)$$

$$\frac{\partial C_i^L}{\partial t} = \tilde{D}^L \frac{\partial^2 C_i^L}{\partial z^2} \quad (2)$$

Again, we assume:

- The diffusion coefficients are constant and not composition dependant
- Local equilibrium exists at the solid/liquid interface
- Semi-infinite domain

The standard solution for Fick's 2nd law is again:

$$C_i = A + B \cdot \operatorname{erf} \left(\frac{z}{\sqrt{4\tilde{D}t}} \right) \quad (3)$$

We can now define $\xi = K\sqrt{4\tilde{D}t}$
 $z = \lambda\sqrt{4\tilde{D}t}$

Where:

- K = Dimensionless growth constant
- λ = Boltzmann's change of variable
- $z = \xi$ at the solid/liquid interface

Considering only the diffusion of solute atoms in a semi-infinite single phase located between $z = \xi$ & $z = \infty$ with the following boundary conditions:

- ξ is dependant on t
- $C = C^\xi$ at $z = \xi$
- $C = C^\infty$ at $z = \infty$

$$C_i = C_i^\infty + (C_i^\xi - C_i^\infty) \left[\frac{\text{erfc}(\lambda)}{\text{erfc}(K)} \right] \quad (4)$$

Taking the derivative of the standard solution with respect to λ we get the following equations:

$$\frac{\partial C_i^S}{\partial z} = - \frac{(C_i^{SL} - C_i^{\infty,S}) \exp\left(-\lambda^2 \frac{\tilde{D}^L}{\tilde{D}^S}\right)}{\sqrt{\pi \tilde{D}^S t} \text{erfc}\left(K \sqrt{\frac{\tilde{D}^L}{\tilde{D}^S}}\right)} \sqrt{\frac{\tilde{D}^L}{\tilde{D}^S}} \quad (5)$$

$$\frac{\partial C_i^L}{\partial z} = - \frac{(C_i^{LS} - C_i^{\infty,L}) \exp(-\lambda^2)}{\sqrt{\pi \tilde{D}_i^L t} \text{erfc}(K)} \quad (6)$$

A mass balance can be examined by equating the fluxes across the solid/liquid interface:

$$\tilde{D}^L \frac{\partial C_i^L}{\partial z} \Big|_{z=\xi} - \tilde{D}^S \frac{\partial C_i^S}{\partial z} \Big|_{z=\xi} = (C_i^{SL} - C_i^{LS}) \frac{\partial z}{\partial t} \Big|_{z=\xi} \quad (7)$$

Substituting equations (5) & (6) into equation (7) we get:

$$\frac{\partial z}{\partial t} \Big|_{z=\xi} = \frac{1}{\sqrt{\pi t}} \left[\sqrt{\tilde{D}^L} \left(\frac{C_i^{LS} - C_i^{\infty,L}}{C_i^{LS} - C_i^{SL}} \right) \frac{\exp(-\lambda^2)}{\operatorname{erfc}(K)} - \sqrt{\tilde{D}^S} \left(\frac{C_i^{SL} - C_i^{\infty,S}}{C_i^{LS} - C_i^{SL}} \right) \frac{\exp\left(-\lambda^2 \frac{\tilde{D}^L}{\tilde{D}^S}\right)}{\operatorname{erfc}\left(K \sqrt{\frac{\tilde{D}^L}{\tilde{D}^S}}\right)} \right] \quad (8)$$

Differentiating z with respect to t :

$$\frac{\partial z}{\partial t} \Big|_{z=\xi} = \frac{\partial}{\partial t} K \sqrt{4\tilde{D}^L t} = \frac{K\tilde{D}^L}{\sqrt{\tilde{D}^L t}} = K \sqrt{\frac{\tilde{D}^L}{t}} \quad (9)$$

Substituting equation (9) into (8) and evaluating the resulting equation at $K = \lambda$:

$$K = \frac{1}{\sqrt{\pi}} \left[\left(\frac{C_i^{LS} - C_i^{\infty,L}}{C_i^{LS} - C_i^{SL}} \right) \frac{\exp(-K^2)}{\operatorname{erfc}(K)} - \sqrt{\frac{\tilde{D}^S}{\tilde{D}^L}} \left(\frac{C_i^{SL} - C_i^{\infty,S}}{C_i^{LS} - C_i^{SL}} \right) \frac{\exp\left(-K^2 \frac{\tilde{D}^L}{\tilde{D}^S}\right)}{\operatorname{erfc}\left(K \sqrt{\frac{\tilde{D}^L}{\tilde{D}^S}}\right)} \right] \quad (10)$$

Solving the equation numerically, we can thus determine the dimensionless growth constant. Assuming that the boron diffusivity in the liquid is the controlling mechanism, the time of dissolution can then be calculated with the following equation:

$$t_h = \frac{Z^2}{16K^2 \tilde{D}^L} \quad (11)$$

Where the interface displacement, (Z) is:

$$Z = \left(\frac{W_m - 2h}{2} \right) \quad (12)$$

The theoretical maximum width of the liquid, W_m region is a function of the concentration ($C^{\infty,L}$) of melting point depressant in the interlayer of thickness, h , and the equilibrium liquidus composition (C^{LS}) at the processing temperature [72]:

$$W_m = 2h \frac{\rho_o}{\rho_L} \frac{C^{\infty,s}}{C^{LS}} \quad (13)$$

Appendix C - Analytical Solution of the Isothermal Solidification Stage

During the isothermal solidification stage solute from the liquid phase continues to be redistributed to the substrate. In the liquid phase, the concentration of solute can be considered to be uniform due to the completion of homogenization in the previous stage and therefore solute diffusion in the liquid is ignored. The isothermal solidification process can again be described by Fick's 2nd law:

$$\frac{\partial C_i^s}{\partial t} = \tilde{D}^s \frac{\partial^2 C_i^s}{\partial z^2} \quad (1)$$

Again, we assume:

- Constant diffusion coefficients
- Local equilibrium at the solid/liquid interface
- Semi-infinite domain

Thus allowing the standard solution to Fick's 2nd law can be written as an error function expression:

$$C_i = A + B \cdot \operatorname{erf} \left(\frac{z}{\sqrt{4\tilde{D}t}} \right) \quad (2)$$

We can now define $\xi = K\sqrt{4\tilde{D}t}$
 $z = \lambda\sqrt{4\tilde{D}t}$

Where:

- K = Dimensionless growth constant
- λ = Boltzmann's change of variable
- $z = \xi$ at the solid/liquid interface

Considering only the diffusion of solute atoms in a semi-infinite single phase located between $z = \xi$ & $z = \infty$ with the following boundary conditions:

- ξ is dependant on t
- $C = C^\xi$ at $z = \xi$
- $C = C^\infty$ at $z = \infty$

$$C_i = C_i^\infty + (C_i^\xi - C_i^\infty) \left[\frac{\text{erfc}(\lambda)}{\text{erfc}(K)} \right] \quad (3)$$

Taking the derivative of the standard solution with respect to λ we get the following equation:

$$\frac{\partial C_i^S}{\partial z} = - \frac{(C_i^S - C_i^\infty) \exp(-\lambda^2)}{\sqrt{\pi\tilde{D}^S t} \text{erfc}(K)} \quad (4)$$

A mass balance can be examined by equating the fluxes across the solid/liquid interface:

$$\tilde{D}^S \frac{\partial C_i^S}{\partial z} \Big|_{z=\xi} = (C_i^{LS} - C_i^{SL}) \frac{\partial z}{\partial t} \Big|_{z=\xi} \quad (5)$$

Substituting equation (4) into (5), we get:

$$\frac{\partial z}{\partial t} \Big|_{z=\xi} = \frac{1}{\sqrt{\pi t}} \left[\sqrt{D^S} \left(\frac{C_i^{SL} - C_i^{\infty,S}}{C_i^{LS} - C_i^{SL}} \right) \frac{\exp(-\lambda^2)}{\operatorname{erfc}(K)} \right] \quad (6)$$

Differentiating z with respect to t :

$$\frac{\partial z}{\partial t} \Big|_{z=\xi} = \frac{\partial}{\partial t} K \sqrt{4\tilde{D}^S t} = \frac{K\tilde{D}^S}{\sqrt{\tilde{D}^S t}} = K \sqrt{\frac{\tilde{D}^S}{t}} \quad (7)$$

Substituting equation (7) into (6) and evaluating the resulting equation at $K = \lambda$

$$K = \frac{1}{\sqrt{\pi}} \left[\left(\frac{C_i^{SL} - C_i^{\infty,S}}{C_i^{LS} - C_i^{SL}} \right) \frac{\exp(-K^2)}{\operatorname{erfc}(K)} \right] \quad (8)$$

Solving the equation numerically, we can thus determine the dimensionless growth constant. The time of solidification can then be calculated with the following equation:

$$t_s = \frac{W_m^2}{16K^2 \tilde{D}^S} \quad (9)$$